Delft University of Technology

Wind Propulsion for Merchant Vessels

Assesing the Performance of a VentiFoil for Wind Assisted Propulsion

Thesis Report

Author
Anton Kisjes

Examination Committee
prof. dr. ir. T.J.C. van Terwisga
ir. A.A. van der Bles
dr. ir. J. Sterenborg
ir. R. Eggers
dr. ir. A. Vrijdag
ir. S. Schenke

Supervisors
prof. dr. ir. T.J.C. van Terwisga
dr. ir. Joost Sterenborg
ir. A.A. van der Bles
ir. F. Nieuwenhuis
ir. N. van der Kolk

A thesis in the partial fulfilment of the requirements for the degree of
Master of Science in Marine Technology

October 15, 2017

Acknowledgements

In the partial fulfillment of the master Marine Technology at the TU Delft, this master thesis is established in cooperation with two other parties which are CONOSHIP and MARIN. At first, I would like to greatly thank Guus van der Bles and Frank Nieuwenhuis of CONOSHIP for offering me interesting master thesis subject with regard to wind propulsion for existing ships.

Special thanks goes to Tom van Terwisga and Joost Sterenborg who made a considerable amount of time for me in guidance and support during my thesis. I am grateful to members of the committee who provided me with feedback on the report and giving their opinion during supervisory meetings about the direction of the thesis.

Also I specially thank MARIN, for offering me a nice workstation and the possibility to conduct CFD computations with ReFRESCO on the marclus3 cluster where I used a considerable amount of computational resources. Therefore I would like to thank employees of MARIN at the R&D Department Guilherme Vaz, Maarten Kerkvliet, Bart Schuiling, Douwe Rijpkema, Serge Toxopeus and Joris Brouwer for their fruitful conversations regarding using ReFRESCO and helping me with the CFD modeling of a turbosail and other topics.

Abstract

The awareness of the impact of air pollution on global climate change is more and more growing in society. The urgency to make ships more eco-friendly captures the interest of shipowners and naval architects. Hull designs of a ship, with regard to minimum fuel consumption have been optimized in the last decades and it has been proven difficult to improve current hull forms. Another strategy is to reduce fuel consumption by using external wind power combined with engine power, so called ‘wind-assisted propulsion’ or ‘motor-sailing’. The potential of an extraordinary high lifting device of a mechanical sail using aspiration power, known as a ’Turbosail’ introduced by Jacques Cousteau [1], has been selected as wind propulsion for an existing cargo ship. This foil can generate about 3 times higher lift compared to conventional foils, which do not use active suction of the boundary layer. Similar to the concept of a velocity prediction program for sailing yachts, a fuel prediction program (FPP) is set up to visualize the fuel savings for all wind directions relative to the vessel. For a wind force 7 Beaufort, the fuel savings for optimal wind angle can reach up to 40%, which are enormous.

The working mechanism of the Turbosail is further explored and examined with CFD using ReFRESCO [38], to see if the performance of the Turbosail is as high as reported by Cousteau. Steady and unsteady RANS simulations are conducted for infinite span Turbosail using the $k-\omega$ SST turbulence model of Menter [32]. As a verification study, an expansion of two other turbulence models are included, which are the $k-\omega$ SST-LCTM model of Langtry et al [30] and the EARSM model for a more anisotropic flow accounting for Reynolds stresses. The difference between all turbulence models appeared to be small, and a fair agreement is found with the lift and drag coefficients found by experiments of Cousteau.

A steady RANS simulation has been conducted at model scale for a finite Turbosail to calculate the lift, drag and aspiration power. The distribution of air suction along the span of the foil is visualized, which gives insight for the real experiments. During this study, a Turbosail at model scale 1:2 is built with a span height of 5.5 metres and a chord length of 1 metre. The comparison with CFD is therefore very useful for validation. As a final step, the lift and drag coefficients found from the numerical result are implemented in the FPP. The fuel savings from the FPP are analysed by placing four full scale Turbosails on an existing cargo ship. In this model, there has been accounted for aspiration power needed for the boundary layer suction. Hydrodynamic forces due to leeway of the hull and rudder, propeller efficiency and specific fuel oil consumption of the engine.

Contents

List of Figures

List of Tables

List of Abbreviations

Abbreviation	**Description**
BHP	Brake Horse Power
CFD	Computational Fluid Dynamics
DDES	Detached Delayed Eddy Simulations
DNS	Direct Numerical Simulations
DWT	DeadWeight Tonnage
EEDI	Energy Efficiency Design Index
FPP	Fuel Prediction Program
IMO	International Maritime Organization
LES	Large Eddy Simulations
PPP	Power Prediction Program
PTO	Power Take Off
RANS	Reynols Average Navier Stokes
RPM	Rotations Per Minute
SFOC	Specifiec Fuel Oil Consumption
SRANS	Steady Reynols Average Navier Stokes
SRS	Scale Resolved Simulations
TNT	Turbulent Non-Turbulent
TST	Transient Scanning Technique
URANS	Unsteady Reynols Average Navier Stokes
VPP	Velocity Prection Program
WASP	Wind ASisted Propulsion
WCU	Winc conversion Unit

List of Symbols

Symbol	Description	Units
α	Angle of attack	[°]
$\alpha\_\{AW\}$	Apparent wind angle	[°]
β	leeway angle	[°]
δ	rudder angle	[°]
η_H	hull efficiency	[-]
η_O	Open water efficiency	[-]
η_P	propeller efficiency	[-]
η_R	relative rotative efficiency	[-]
ϕ	heel angle	[°]
ρ	density of seawater	[kg/mˆ3]
ρ_air	Density of air	[kg/mˆ3]
A_R	Aspect ratio	[-]
$C_{N,H}$	coefficient for yaw moment of the hull	[-]
C_{turbo}	Interaction coefficient between multiple turbosails	[-]
$C_{x,H}$	coefficient for induced drift resistance of the hull	[-]
$C_{y,H}$	coefficient for hydrodynamic side force of the hull	[-]
C_B	Block coefficient of ship	[-]
C_D	Drag coefficient	[-]
C_L	Lift coefficient	[-]
C_M	midship coefficient	[-]
C_q	Suction coefficient of turbosail	[-]
D	diamater of propeller	[m]
F_D	drag force	[kN]
F_L	Lift force	[kN]
h	Span height of turbosail	[m]
J	advance ratio	[-]
K_Q	torque coefficient of propeller	[-]
K_T	thrust coefficient of ship or propeller	[-]
L_{pp}	Length of ship between perpendiculars	[m]
L_C	Chord length of turbosail	[m]
M_{st}	Stabilizing moment of the ship	[kNm]
M_z	yaw moment	[kNm]
n_{turbo}	number of turbosail on the ship	[-]
n_e	engine rotation rate	[rpm]
n_p	shaft rotation rate	[rpm]
P_a	Aspiration Power	[kW]
P_B	Brake power of engine	[kW]
P_D	Delivered power of propeller	[kW]
P_E	Effective power	[kW]
p_{stat}	static pressure	[Pa]
p_t	total pressure	[Pa]
Q	Air mass flux through suction region	[mˆ3/s]
R_{rudder}	Rudder resistance	[kN]
R_0	Bare hull resistance	[kN]
R_1	Net resistance for ship with WASP	[kN]

Symbol	**Description**	**Units**
R_i	Induced resistance due to leeway	[kN]
S	Surface of turbosail	[mˆ2]
t	thrust deduction factor	[-]
T	draught of the ship	[m]
T_{wcu}	Forward towing force of total WCUs	[kN]
TB	Thrust benefit	[-]
U_{AW}	Apparent wind velocity	[m/s]
U_∞	Freestream velocity	[m/s]
v_{eff}	Effective rudder inflow speed	[m/s]
v_a	advance velocity before propeller plane	[m/s]
v_s	ship velocity	[m/s]
v_t	tangential velocity component	[m/s]
v_x	axial velocity component	[m/s]
w	wake fraction	[-]
X_{vv}	coefficient for induced drift resistance of the hull	[-]
U_ϕ	Numerical uncertainty	[%]
y^+	Dimensionless wall spacing	[-]

Chapter 1

Introduction

1.1 Background

At the present, governments and society see the urgency to reduce carbon dioxide emissions and other greenhouse gases to prevent further global warming. In the latest climate conference in Paris (2015), nations agreed to drastically reduce their greenhouse gases in the next decades. Although shipping is an efficient way to transport goods, it is still a polluting industry. B. Notenboom [35] with the documentary 'Seablind', states that the shipping industry is a big pollutant with regard to sulphur and black carbon. The sixteen largest container ships emit as much sulphur as all cars on earth. Another relative unknown greenhouse gas is black carbon, 13% of all black carbon is emitted by ships. In the Artics, black carbon accelerates the melting of ice and this effect is not investigated thoroughly. Black carbon remains three weeks in the atmosphere while carbon dioxide stays in the air for 70 years. Therefore, measurements to reduce the emission of ships could have a rapid effect on a cleaner atmosphere. The demand for non-polluting and more efficient ships is therefore growing by industry and society.

From economical point of view the current market condition can be described as poor, reported by e.g. Financieel Dagblad [34] and Schuttevaer [33]. Rates for bulk cargo are historically low in 2016. The low cargo rates can be ascribed to the large shipping capacity. At the economical peak of 2007, shipping companies ordered a great amount of new built ships from which some of them still needs to be built. Because it is hard to survive in current markets, shipping companies are looking for new ways to improve their energy efficiency of current ships and to make the shipping industry more sustainable to comply with new regulations. During the mid-eighties, wind propulsion for ships has been examined by for example Cousteau et al [1] with the Turbosail. This technology, however, did not lead to a breakthrough of wind propulsion for ships. Nevertheless, because the potential of wind propulsion is high and ships need to be more environmental friendly, the future of wind-assisted propulsion may not be far away. In last decades, a great development in systems and control will raise the transition of ships assisted with wind-propulsion.

Wind propulsion delivers additional forward thrust to the ship and should reduce the brake power of the engine, resulting in fuel savings of the vessel. Wind propulsion will therefore be a combination of sailing and using engine power, so called motor-sailing or wind assisted propulsion (WASP). WASP has some great advantages. One main advantage is that it has the potential to realize large fuel savings. In some ports, discount on port costs are given as an incentive to stimulate environmental friendly ships. Moreover, wind-assistance reduces energy efficiency index (EEDI) which means that a ship complies with the latest environmental regulations, see IMO criterion [36].

1.2 State of Art

Wind assisted propulsion has captured also the interest of ship design company Conoship. Conoship is specialized in short sea shipping for different sorts of cargo with vessels in the range of up to 15000 dwt. The service speed is generally relative low of most vessels, between 10–13 knots which makes these vessels perhaps more attractive for motor-sailing than fast sailing vessels, due to a more favourable incoming wind angle in head to beam winds compared to faster sailing vessels.

The Turbosail of Cousteau [1] reported very high lift characteristics of about 2,5-3 times larger compared to conventional wing profiles. The lift force is for most cases (which is true for head and beam winds) the main contributor in forward thrust, while the drag forces reduces the forward thrust. When the surface area of the sails can be minimized, this is an advantage for the captain who has more visibility over the vessel. The Turbosail is an oval mechanical sail, which uses aspiration of a fan to subtract airflow from the air stream. This makes it possible to increase the angle of attack so that the lift is increased.

Because of the outstanding performance of the Turbosail compared to conventional wing sails and other types of wind propulsion examined by van Tuijl [5], Conoship has selected this type of wind propulsion to be retrofitted on vessels which are already in service. As the title suggest, Conoship has assigned the name VentiFoil for the so called 'Turbosail' of Cousteau. The concept idea is that the two Turbosail units are integrated in a 40 ft container, a so called wind conversion unit (WCU), which can be launched and lowered automatically. In port, the WCU can be removed easily to access the cargo. This makes wind propulsion attractive for shipowners because it is practical in use and it has high potential to save fuel.

The forces that act on the Turbosail(s), exert a propulsive driving force and side force on the ship. These side forces need to balance with hydrodynamic forces of ship, causing a heel angle, leeway angle and rudder angle. Therefore it is essential to calculate the hydrodynamic reaction forces to indicate optimal locations to place Turbosails and to quantify the benefit obtained by wind assist. For ships it is very common to predict the resistance of a ship by empirically derived formulas, such as from Holtrop & Mennen [37]. However, for ships sailing under a constant relatively small leeway ($\theta < 5°$) and heel angle ($\phi < 10°$), the performance prediction doesn't include empirically methods for cargo ships. These investigation are still going at the TU Delft, by van der Kolk [9]. Consequently, empirical relations found by manoeuvrability studies are consulted to predict the hydrodynamic forces.

1.3 Aim of Current Study

How can the performance of a ship using wind-assistance be presented in terms of brake power or fuel consumption? To answer this question, it is convenient to take a look at a velocity prediction program (VPP) used for sailing yachts. A VPP shows in polar diagram the resulting ship speed for a range of different wind speeds and wind directions due to the forward thrust of the sails. An example of a VPP can be found by de Jong et al [24]. Aspired by this VPP, the performance of merchant vessel equipped with wind propulsion can be expressed as function of wind speed and all wind directions 360 degrees round, presented in a polar diagram. The performance of the ship can be quantified as the power reduction as a ratio of the total brake power for a constant ship speed, a so called Power Prediction Program (PPP). This PPP can also directly be related and expressed in terms of fuel consumption using the characteristics of the engine. Then, the PPP becomes a Fuel Prediction Program (FPP), which is a concept that is introduced in this thesis. The aim of this study is to built up a FPP by correct modelling of hydrodynamic forces of the hull and the aerodynamic forces of the Turbosails and superstructure with as less simplification as possible. The FPP can eventually be the base input for a weather prediction program, to find the best economical route and thus the largest fuel savings.

In the definition stage the FPP model is built up which is described in chapter 3, based on knowledge from available literature, reviewed in chapter 2. Based on the outcome of this first FPP model, the most uncertain factors are more thoroughly investigated. As a result, it is concluded that the Turbosail is desired to be better understood, such that there becomes more clarity on how a Turbosail performs.

In the next stage, the refinement study, theory about the aspirated foil or Turbosail is examined by a numerical study using CFD package ReFRESCO [38]. In this study the objective is to quantify and verify if the lift and drag forces of the Turbosail are reliable and trustworthy coefficients to assume. This numerical study investigates different turbulence models as a verification study to qualify which modelling techniques are sufficient to be applied to calculate lift and drag forces of the Turbosail.

Consequently, this outcome can be used to investigate other profile variants which can be used in an optimization process. Also a better prediction can be made of the fan power, which can improve the accuracy of the FPP.

1.4 Research Questions

In this thesis, the following research questions will be treated concerning the power prediction program and the Turbosail.

1. How large are the fuel savings for a general cargo ship of 4500 DWT by installing four Turbosails on deck for multiple wind speeds and 360 degrees round true wind angles?

Regarding the lift and drag coefficients of the Turbosail, two sub questions can be defined:

2. What are the lift and drag forces of a Turbosail with infinite aspect ratio, for a range of angles of attack at three dimensionless suction speeds of $C_q = [0; 0.032; 0.047]$ at an apparent wind speed of $U_{AW} = 10m/s$ (corresponding to a Reynolds number of $6 \cdot 10^5$) by performing a verification study investigating different turbulence models?
3. How large are the lift and drag coefficients for a single finite Turbosail at model scale 1:2 with an aspect ratio of $A_R = 5.5$ at a suction speed of $Cq = 0.047$ and an apparent wind speed of $U_{AW} = 10m/s$?

1.5 Approach

To be able to answer the research questions presented in section 1.4, the following methodology is adapted.

1. At first, all relevant components that need to be present in a FPP are analysed in a literature review. These components include hydrodynamic side force and induced resistance preditions, rudder forces, propeller efficiency, stability and Turbosail forces.
2. With some simplifications, a FPP is built up. A variation of the vessel speed, propeller rotation rate and wind speed is made to investigate the effect of each parameter. From this analysis, a selection is made of the most uncertain factors in the FPP which was concluded to be the Turbosail.
3. From the FPP, it is desired to have a better understanding and more trustworthy prediction of the Turbosail characteristics. A numerical analysis with CFD is set up to predict performance of the lift and drag coefficients of a Turbosail with infinite span using several turbulence models. These lift and drag coefficients for infinite span are compared to the reported lift and drag coefficients of Cousteau [1] for infinite span.
4. A Turbosail with a finite aspect ratio of $A_R = 5.5$ is modeled with CFD, to find the lift and drag coefficients at the optimal angle of attack, α.
5. For the aspiration of the Turbosail, a fan is selected. The power input of fan necessary to realize a particular suction speed is estimated from the CFD computations and inserted in the FPP model. The original FPP is updated with the new lift and drag coefficient including the required power for aspiration of the Turbosail.
6. The final conclusion can be drawn whether the Turbosail is beneficial as a wind propulsion device for ships.

Chapter 2

Literature Review

This chapter summarizes previous research on ships using wind-assisted propulsion reported by graduates at Conoship and several other relevant subjects such as, the main concept of a Turbosail, the hydrodynamic forces under leeway consulted from manoeuvrability studies, and how sails may effect propulsive efficiency of a vessel.

2.1 Research on WASP by Conoship

Wind-assisted propulsion for cargo ships has already captured the attention of Conoship International. A few graduates, van Tuijl [5] and Dijkman [4] have investigated the potential of wind-assisted propulsion. The work of van Tuijl and Dijkman will be reviewed in section 2.1.2 and 2.1.3. Furthermore, in section 2.1.1 the idea of wind conversion units WCUs are described in the feasibility study [15]. A physical model is built up to investigate the feasibility of the wind-assisted propulsion. The description of the model and the assumptions made, are discussed and form the initial base for the Fuel Prediction Program, discussed in chapter 3.

2.1.1 Feasibility Study

The feasibility study analyses the potential of WASP by placing wind conversion units (WCU) on a 4500 DWT general cargo ship for two concepts, also depicted in figure 2.1:

- Concept 1: 4 WCUs where each WCU contains one retractable Turbosail with a span of 20m
- Concept 2: 2 WCUs containing each one Turbosail with a span of 28.5m.

The concept of the WCU is described in the following and a summary of the basic assumptions is given how the feasibility study calculates the fuel savings based on the physical model. In this thesis, the 4500 DWT general cargo ship is also used as base vessel, with its characteristics presented in Appendix A. A common route of the vessel is chosen to be between Rotterdam - Turku (Finland) and the fuel savings are calculated using simplified assumptions. Eventually, the quality of these assumptions determine how accurate the estimate of fuel savings is of a motor-sailing ship.

The concept of a wind conversion unit is that one or more Turbosails are integrated in a 40 or 45 foot container. The main advantage is that a container can be connected on many vessels and has the ability to be easily and quickly coupled or decoupled in harbour to access the cargo. An simple sketch of this idea is shown in figure 2.1. The Turbosail is retractable for unfavourable wind directions such as winds coming from ahead, so that there is no penalty of additional air resistance.

From construction point of view, the WCU's will be placed parallel to each other and connected with interconnected frames to reduce deck point loadings by a factor 5 to withstand the moment of the Turbosail, illustrated in figure 2.2.

Basic assumptions. The basic assumptions used in feasibility study [15] are reviewed in the following, to assess a performance prediction of the presented WCU concepts in figure 2.1. The physical model contains the aspects as: Turbosail forces, stability criteria, hydrodynamic forces, propulsive efficiency (Kt-Kq curves, open propeller diagrams) and specific fuel consumption for different engine loadings.

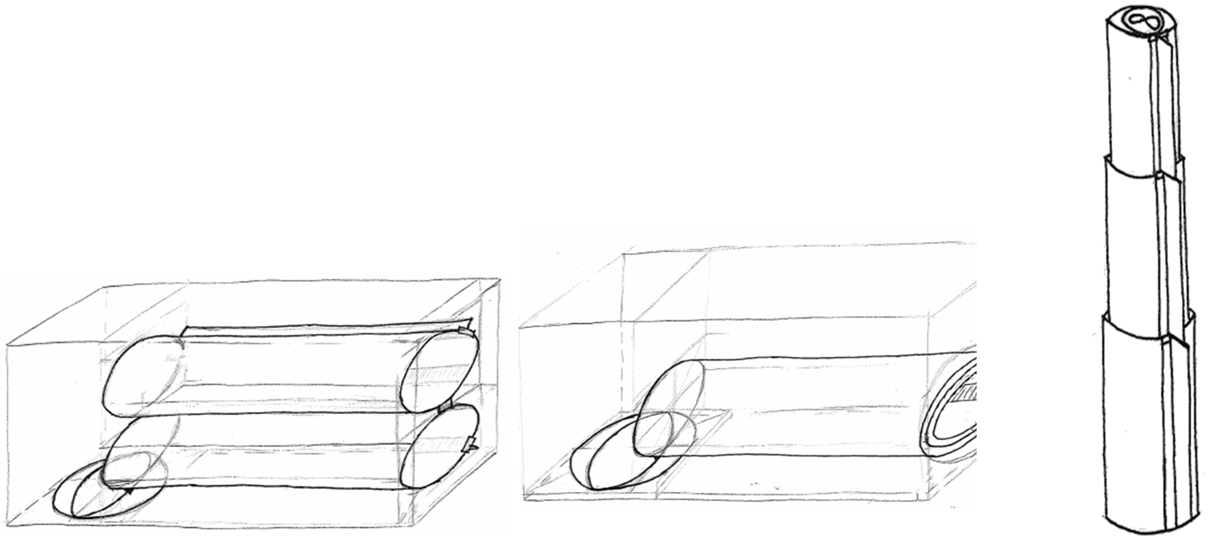

(a) Concept 1.

(b) Concept 2.

Figure 2.1: Two WCU concepts from the feasibility study [15]: concept 1, a two part foldable Turbosail in a 40ft container of 20m. Concept 2, a three part foldable Turbosail reaching a total span of 28.5m.

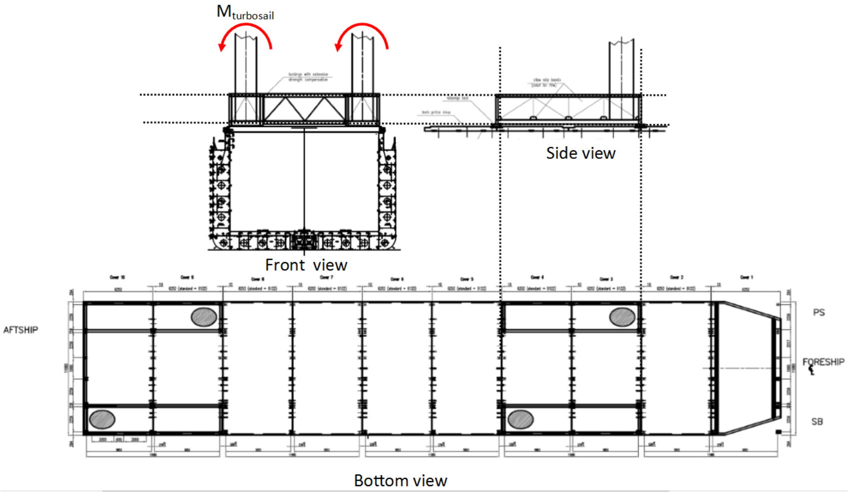

Figure 2.2: Connection of WCU's on ship.

- Turbosail forces. Turbosail forces are based on the maximum reported lift and corresponding drag coefficients of Cousteau [1]. To quantify if these coefficients are realistic values, additional literature about Turbosail is reviewed in section ??. As already mentioned in the introduction of chapter 1, a numerical analysis of a Turbosail is conducted using CFD (Computational Fluid Dynamics) to verify the experimental data reported by Cousteau and to compare with new experiments.

- Stability criteria. The stabilizing moment is calculated for several loading conditions at design draught with PIAS, a program that Conoship uses to calculate the stability. From the perspective of the captain, the decision is made that maximum heeling angle should not exceed $\phi > 10^\circ$. For a certain loading condition, the stabilizing moment has a maximum allowable value of $M_{st,10^\circ} = 310tonm = 3000kNm$. However, specific details of GM are not provided in this report. From the IMO (International Maritime Organisation) wind criteria , stated in [15], The ship should withstand a stable wind force 10 assuming a drag coefficient of the hull of $C_{D,hull} = 1$. This corresponds to a wind pressure of $504N/m^2$. However, for a wind gust, the wind pressure increases by a factor 1.5. For the Turbosail forces in this situation, it is assumed that due to a failure the Turbosail cannot be retracted, but the aspiration can be turned off. Therefore, C_L and C_D coefficients for a Turbosails without aspiration should be considered. These lift and drag coefficients are analysed in the numerical study in chapter 6.

- Balance sailing forces. The feasibilty study does not include balance of the Turbosails with the ship.

An induced drift resistance of 1% of total resistance is used, which is an too optimistic assumption.

- Propulsive efficiency. In the feasibility study, the methodology of Klein Woud & Stapersma [39] is used for calculating the propulsive efficiency and the desirable working point of the propeller. The propulsive efficiency η_D, relates the effective towing power P_E to the delivered power to the propeller P_D and is a function of the relative rotative efficiency η_R, hull efficiency η_H, and the propeller open water efficiency η_O, expressed in equation 2.1.

$$P_D = \frac{P_E}{\eta_D} = \frac{P_E}{\eta_O \cdot \eta_R \cdot \eta_H} \tag{2.1}$$

The feasibility study assumes the that relative rotative efficiency remains constant, and that the thrust deduction coefficient t, and wake factor w, remain constant as well, so that the hull efficiency is unchanged. Only the open water efficiency may change considerably, this depends on the type of propeller which is installed. For a fixed propeller and the criteria that the ship sails at constant speed when motor-sailing, the only way to reduce thrust is to decrease the RPM of the propeller. This results in a shift of the advance ratio J, where the advance ratio is defined as,

$$J = \frac{v_s(1-w)}{n_p \cdot D} = \frac{v_A}{n_p \cdot D} \tag{2.2}$$

v_A is the advance velocity in front of the propeller plane. In order to see the effect of propeller open water efficiency, an open water diagram is used where the K_T-curves of the ship and propeller find their equilibrium at J. The thrust coefficient of the ship without wind assist, $K_{T,ship,0}$, is defined as,

$$K_{T,ship,0} = \frac{1}{\rho_s D^2} \cdot \frac{\left(\frac{R_0}{v_s^2}\right)}{(1-t)\cdot(1-w)^2} \cdot J^2 = c_{7,0} \cdot J^2 \tag{2.3}$$

For the situation with wind assistance, thus when Turbosails are delivering forward thrust T_{WCU}, the delivered thrust by the propeller can be reduced, see equation 2.4.

$$K_{T,ship,1} = \frac{1}{\rho_s D^2} \cdot \frac{\left(\frac{R_0 + R_i - T_{WCU}}{v_s^2}\right)}{(1-t)\cdot(1-w)^2} \cdot J^2 = c_{7,1} \cdot J^2 \tag{2.4}$$

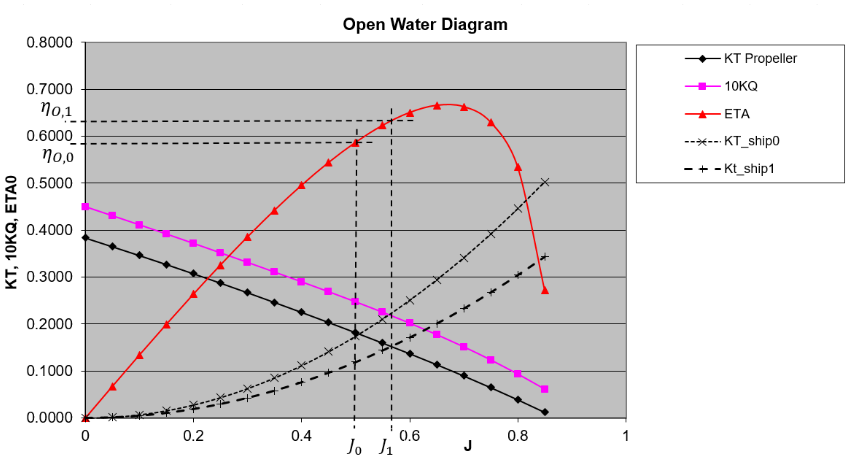

Figure 2.3: Evaluation of intersection of $K_{T,ship}$ and $K_{T,propeller}$ to determine the propeller open water efficiency η_O

Note that due to side forces of the Turbosails, there is a induced drift resistance component for the bare hull and appendages, denoted with R_i. In this feasibilty study, the induced resistance was assumed to be $R_i = 0.01 \cdot R_0$, which is small and not a realistic value. A fixed propeller was selected in the calculation for propeller power, the open water diagram for conventional and wind-assisted condition is presented in figure 2.3 using equation 2.3 and 2.4. In figure 2.3, the Turbosail forces are set at $T_{WCU} = 40kN$. It can be seen that the open water efficiency increases with $\Delta\eta_O = +0.04$.

- Engine loading. The effect of reduced power demand of the engine on specific fuel oil consumption (SFOC) is not modelled in the feasibility study. The optimal SFOC at operating speed of 11 knots is also used for wind-assisted configuration. The choice of propeller, fixed or Controllable Pitch propeller (CP-propeller), determines how the engine will be loaded.

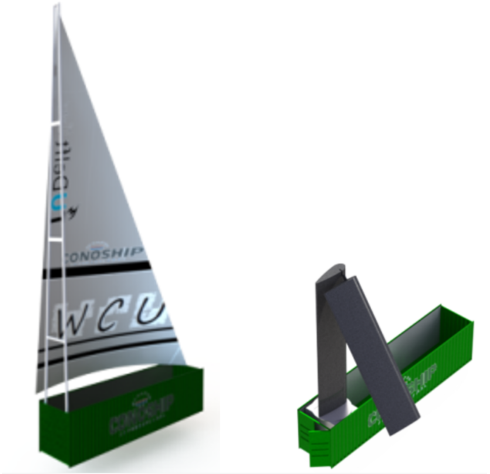

Figure 2.4: Two WCU concepts: Left, soft sail with retractable rolling system. Right, foldable wing sail.

The above described assumptions are for most cases rough estimates and require improvement by better modeling these different aspects. At last, the feasibility study estimates for the route Rotterdam - Turku (Finland), the average fuel savings by using average annual weather conditions. This gives an indication of the reduced fuel costs.

2.1.2 Van Tuijl: ‘Evaluation of Auxiliary Wind Propulsion Systems for Merchant Ships’

The thesis of Van Tuijl [5] was part of the ADEPT project, where other parties in the maritime industry are involved in the development of wind-assisted ships. This thesis evaluates the profitability of different sailing rigs for a 8300 ton general cargo carrier of 121m, comparing the following rig types: wing sail, multi-wing sail, Turbosail, Flettner rotor, cat rig and a square rig.

The profitability is tested by an optimization model which calculates stability, drift angle and rudder angle including the components as bare hull, rudder, propeller, wind forces of superstructure and sails. Eventually, the maximum sail area is calculated by optimization. It must be noted that any insight about the induced resistance of the hull or rudder resistance has not been reported. Also the propulsive power has not been presented for different solutions.

At last, an assessment of the costs and the return on investment is accomplished by analysing capital costs of every rig solution and the fuel savings from wind-assist for different routes. This study gives a overview of many aspects which should be accounted for by analysing a ship installed with wind propulsion.

2.1.3 Dijkman: ‘Feasibility Study at two Wind Conversion Units’

As a continuation on the feasibility study (section 2.1.1), Dijkman investigates two WCU concepts with a rigid wing sail and a soft sail using a retractable rolling system, see figure 2.4. Special focus is set on legislation concerning wind propulsion, where rules are presented to comply with sufficient stability. Fuel savings and return on investment are calculated based on a consistent line between Rotterdam - Turku. Many important aspects are disregarded in this study, such as engine loading (SFOC), balance of the hull and sails, induced resistance and propeller efficiency.

2.2 Turbosail

This section describes the working mechanism of a Turbosail and why the Turbosail of Cousteau [1] has been selected as the best solution for wind assisted propulsion. Previous graduates van Tuijl [5] and Dijkman [4] have investigated different wind propulsion systems. Van Tuijl has investigated the cost effectiveness of a Fletner rotor, different wing profiles, Turbosails and soft sails. Dijkman used a rigid wing sail and a soft sail, because of its trust worthy and elaborated technique.

2.2.1 Introduction

In 1980 – 1985, Jacques Cousteau et al [1] investigated a new type of wind propulsion aspired by the Magnus effect of the Fletner rotor. The Fletner rotor is a rotating cylinder which creates a high and low pressure side by the air friction. Cousteau used this concept and came up with the idea to delay the separation of air-stream along the profile by applying boundary layer suction at the trailing edge of the wing profile, called the 'Turbosail'. The Turbosail has a vertical tube of forward elliptic cross section with a flap and boundary layer suction, depicted in figure 2.5. The flap is added to ensure separation while the boundary layer suction delays separation point at the suction side, generating high lift forces while the drag remains low.

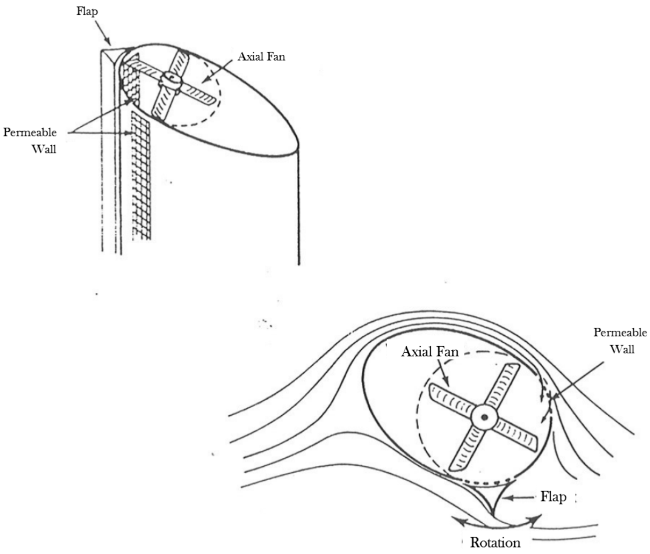

Figure 2.5: Working principle of a Turbosail

2.2.2 Turbosail Forces

The lift and drag forces generated by the Turbosail can be calculated by the general formula for a wing according to eq. 2.5 and eq. 2.6.

$$F_L = \frac{1}{2}\rho_{air} C_L U_{AW}^2 S \tag{2.5}$$

$$F_D = \frac{1}{2}\rho_{air} C_D U_{AW}^2 S \tag{2.6}$$

Where ρ_{air} is the density of air, U_{AW} is the apparent wind velocity and S is the surface area of the wing, defined as the chord length L_C versus the span height h. A limited amount of experimental data for Turbosails is available from literature. Only Cousteau et al [1] reported experimental results for Turbosails. Cousteau provides wind tunnel test results for an aspect ratio of 4 and for an infinite span (both ends constraint at the wall). Also the pressure coefficient C_p is given along the Turbosail profile at for the case of maximum lift, but not specifying the angle of attack α. The lift and drag coefficients, C_L and C_D for an aspect ratio of 4 (effective aspect ratio is 8) are given in figure 2.7 and in figure 2.6 for infinite span. The position of the flap and the location for air suction have been varied independently and the results of the best performing position are presented. As can be seen from these figures is that the lift and drag coefficients depend on the angle of incidence, α and the amount of boundary layer suction, denoted by mass flux Q in $[m^3/s]$. The dimensionless suction coefficient C_q is defined in equation 2.7.

$$C_q = \frac{Q}{SU_{AW}} \tag{2.7}$$

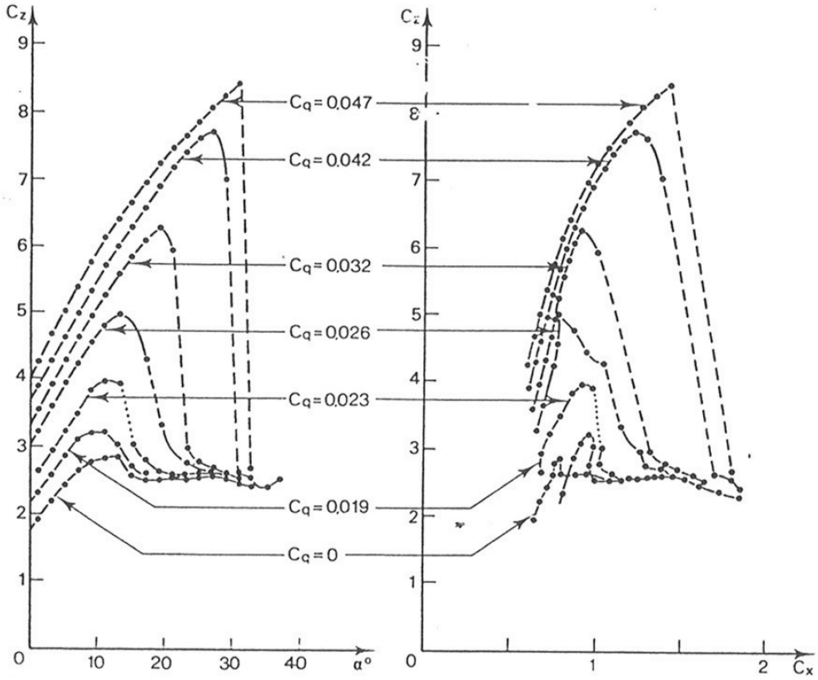

Figure 2.6: Lift and drag coefficients according to Cousteau [1] for infinite aspect ratio and different suction coefficients C_q

In figure 2.7, the lift and drag coefficients are presented for an aspect ratio of $AR = 4$ which is equal to an effective aspect ratio of $AR_e = 8$. This effective aspect ratio is increased by the connection of the Turbosail on the ground, so there are no losses due to vortex shedding. Vortex shedding is only relevant for the top end of the Turbosail. It can be seen that a suction coefficient of $C_q = 0.05$, gives a maximum lift of $C_L = 6.7$ with a drag coefficient of $C_D = 1.85$. When less suction is applied, at $C_q = 0.027$ the lift coefficient becomes $C_L = 5.0$ and $C_D = 1.2$.

2.2.3 Turbosail Best Solution

There are several reasons why a Turbosail is an attractive wind propulsion system compared to other solutions such as soft sails, kite, fletner rotor, etc. One main reason is that the Turbosail produces high lift force and has high lift/drag ratios compared to a Flettner rotor. Since the Turbosail is integrated in a 40ft container, the maximum area, S, of the sail is restricted by the dimension of the container. To obtain the largest forward thrust from wind propulsion, the lift coefficient needs to be maximized, as well as C_L/C_D- ratio, because the drag force reduces the forward thrust for most cases.

The surface area S of the Turbosail, is in common wing theory defined as the product of chord length and span (height). However, in the Turbosail pattent [16], the surface area S is reported as: *'the surface area of the device as projected on a plane perpendicular to the direction V in which the fluid moves'*. This would suggest that the chord length reduces for larger incoming angles of attack α. Then, the remarkable large lift coefficients can be subscribed as a consequence of definition of S, which gives much higher lift coefficients. This topic is further discussed in the problem description of section 4.1. Since the area S is restricted by the dimensions of the container, the chord length and span height need to be maximized within the container's boundaries. This makes the Turbosail and the Fletner rotor the most favourable for wind propulsion, because of their large lift and drag coefficients and thus delivering the largest forward thrust per unit surface area.

The Fletner rotor, however, has a disadvantage regarding from structural point of view. The rotation

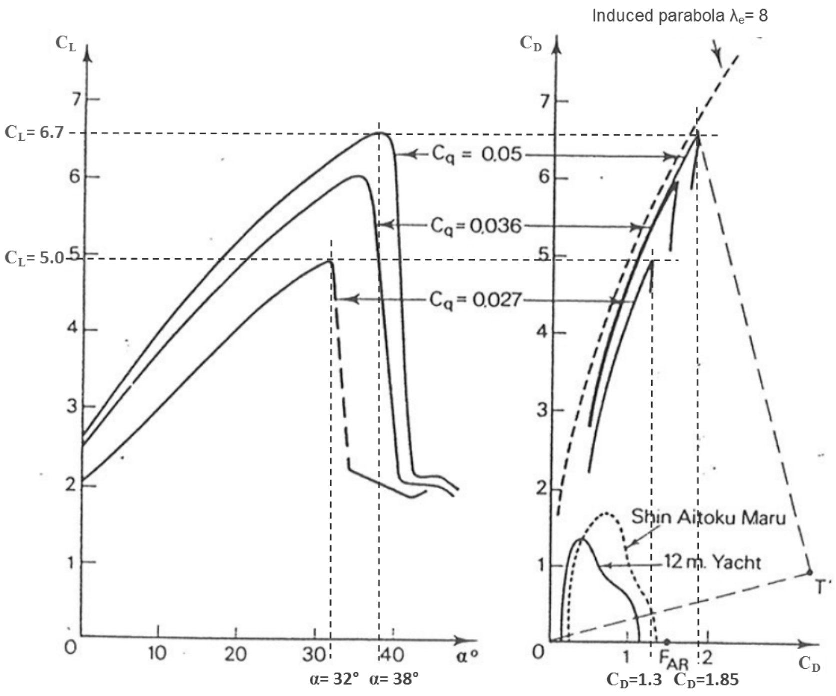

Figure 2.7: Lift and drag coefficients according to Cousteau [1] for an aspect ratio of 4 and different suction coefficients C_q.

of the cylinder, causes gyro forces under roll and sway motions. These forces can exceed the structural capacity and may cause fatigue problems since the loading is periodic. Moreover, the C_L/C_D ratio is smaller for a Fletner rotor than for a Turbosail. Based on these characteristics, the Fletner rotor is rejected as wind propulsion device.

In previous research projects on WASP for Conoship, Dijkman [4] investigated two different wing sails. This was a two – part foldable wing sail which has a total span of 20 meters. The connection of both parts, requires a hydraulic system which is expensive and may be sensitive for failures and maintenance. The maximum lift coefficients of a wing sail is around 2-2.5 while a Turbosail can reach lift coefficient around $C_L = 6 - 7$. Van Tuijl [5] compared different wind propulsion devices on their performance in figure 2.8, expressed in the thrust coefficient and lateral force coefficient for all apparent wind angles.

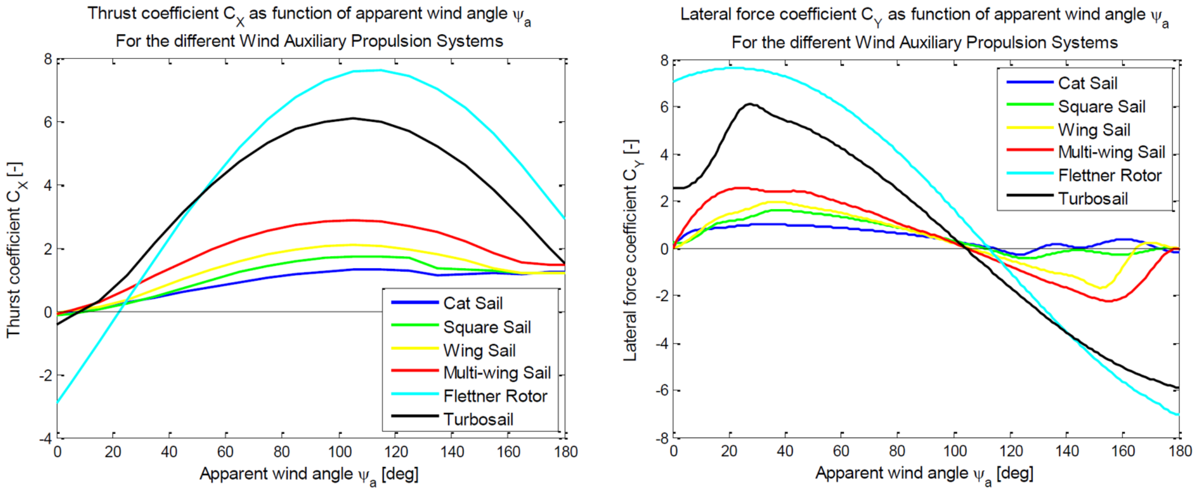

Figure 2.8: Lift and drag forces for different wind propulsion systems by van Tuijl [5].

It can be observed that the Turbosail produces the most propulsive power for small apparent wind angles compared to the other wind propulsion systems. However, this comparison is not totally fair, since little power is needed for the aspiration of the Turbosail. Based on its high lift coefficients, the absence of gyro forces (Fletner rotor) and the ability to easily reduce power by controlling the air suction, the Turbosail seems to be the best sail for wind propulsion. However, it has not been explored if the Turbosail is best solution from cost perspective, this aspect is disregarded in this thesis.

2.2.4 Hcini: ‘A Turbosail Profile Analysis Code Based on the Panel Method’

A recent research about the performance of a Turbosail is published by Hcini et al [17], who investigated the effect of flap and suction position, suction intensity and relative thickness of the Turbosail on the lift and drag forces. A numerical flow simulation of 2D Turbosail profile was conducted using a the Hess-Smith panel method, which is based a potential flow theory.
It appears that the Turbosail produces higher lift and drag coefficients when the relative thickness, yielding a thicker foil, increases. The position of the flap size is varied between 0° and 35°, which shows that the flap effectively increases the lift force. The amount of air suction has effect on the drag coefficient; more air suction leads to lower drag forces. This study gives some guidance for the optimal flap position and the suction speed.

2.3 WASP Model

2.3.1 Viola et al: ‘A numerical Method for the Design of Ships with Wind-assisted Propulsion’

Viola et al [7] gives an overview on how to assess the performance of a KVLCC2M tanker equiped with various wing sail configurations. The hydrodynamic forces for sailing under leeway are based on empirical formulations. These empirical formulation deviate from manoeuvring theory by Kijima et al [10], but the origin of the empirical formula are not cited. The validity of these expressions is therefore not justified. A summary is given of the equation of motion with most relevant forces. Further, it explains how these equations can be solved iteratively in order to obtain equilibrium in F_x, F_y and M_z. This WASP model calculates what rudder angle needs to be given to balance the hull forces and external wind forces.

The equation of motion for a vessel with wind-assist is built of the following components: the hull (subscript h), rudder (subcript r), forces due to wind resistance of the superstructure (subscript s), the Turbosail (subscript t) and propeller (subscript p), see equation 2.8-2.10. Forces due to current and waves are not included in this model.

$$X_h + X_r + X_t + X_s + X_t = -X_p \tag{2.8}$$

$$Y_h + Y_r + Y_s + Y_t = 0 \tag{2.9}$$

$$N_h + N_r + N_s + N_t = 0 \tag{2.10}$$

The external wind forces for the superstructure and wing sails are calculated with a numerical model using RANS. The influence of the wing aspect ratio is investigated, under the assumption that the height of the wing sail is restricted and the total wing area is constant. It is concluded that it is more efficient to place more high aspect ratio wings than a less wings with low aspect ratio but equal surface area. Stability criteria are not considered in this model, which means there is no limitation for the sail area.

When the performance of a ship with WASP is analysed, one compares the benefit from wind propulsion with the condition when no sails are present. The benefit from wind propulsion depends on the driving force of the sails and the additional resistance or loss in efficiency due to leeway and heel. This so called thrust benefit (TB) is also used by van der Kolk [9] and Fujiwara [2], which describes that the benefit of thrust from the sails (with subscript S) X_S should be higher than the additional resistance and/or loss in efficiency of the propulsion system, denoted by X_{tot}. If this expression exceeds 1, this means that the Turbosail adds resistance to the ship so there is no benefit.

$$TB \equiv 1 - \frac{X_S}{X_{tot}} \tag{2.11}$$

2.3.2 Fuijiwara et al: 'Steady Sailing Performance of a Hybrid-sail Assisted Carrier',

Fuijwara et al [2] performed a similar study as Viola et al [7], where the steady sailing performance of a bulk carrier of $L_{pp} = 177m$, $C_B = 0.8$ with rectangular and triangular sails is examined. The reduction of brake horse power (BHP) is calculated for a constant ship speed of 13.5 knots, where it was concluded that the average BHP gain is in the order of 15% for rectangular sails. The methodology is described in the following.
From manoeuvring theory, hydrodynamic derivatives are used to calculate hydrodynamic forces and moments. A tanker with comparable hull dimensions consist of hydrodynamic derivatives derived from model tests and was used to estimate the hydrodynamic loads of the bulk carrier. To counter act the large yaw moment of the bare hull, the rudder is used, where rudder forces and moments are calculated by Kijima et al [10]. Wind forces are based wind force coefficients, derived from wind tunnel experiments on model scale, which is illustrated in figure 2.9. The equation of motion is solved for $\sum X, Y, N, K = 0$ where K stands for the moment around the x-axis, to meet stability criteria.

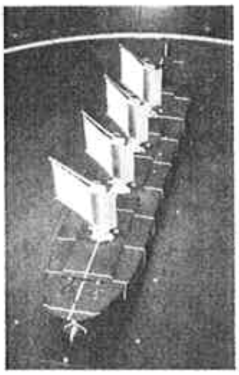

Figure 2.9: Wind tunnel tests of bulk carrier with rectangular sails by Fuijiwara et al [2]

In the force and moment equations, the modelled components include hull, propeller, rudder and external forces due to wind (soft sails and superstructure). These equations are solved to find the resulting leeway β, heel ϕ and rudder angle δ. For a true wind speed of 15 m/s, the leeway, heel, rudder angle and RPM of the propeller are calculated for all wind directions TWA. For an incoming wind direction of 50 degrees relative to head wind, the resulting leeway, heel and rudder angles become $\beta = 2.3°, \phi = 4.2°, \delta = 10°$. The delivered power of the propeller is calculated by K_T/K_Q - diagram of the propeller, which also incorporates the open water efficiency using expressions for K_T and K_Q. It should be mentioned that this open water diagram for the propeller does not account for a oblique flow, although a correction is made for the wake factor, which is dependent of the drift angle. Finally, constant shaft and gearbox efficiencies are used to determine BHP which can be related to the SFOC based on engine characteristics. According to Fuijiwara et al, the lateral force and yaw moment acting on the hull are fairly insensitive to changes of heel angle over the complete drift angle range. In this thesis, it is assumed that the heel angle may not exceed 10° and therefore the effect of heel is also of less importance, in contrast to other aspects as for example drift resistance of hull and rudder forces.

2.3.3 Eggers: 'Operational Performance of Wind Assisted Ships'

Wind assistance and the operational performance was examined by Eggers [3] for a coastal freighter, called the 'Wind Hybrid Coaster' as a subproject of MARITIM. This ship has a relatively short length, $L_{pp} = 85m$, comparable to the reference vessel treated in this thesis. The low service speed of 8.5 knots increases the potential gains from wind propulsion, because of a more favourable apparent wind angle. This study captures most relevant aspects of the operability of a wind-assisted vessel such as: induced resistance, rudder forces and stall, propulsive efficiency, Fletner rotor characteristics, envelope for engine loading (fuel consumption) and voyage optimization (weather routing). To assess the hydrodynamic performance, CFD computations and model test were conducted at small drift angles for a full appended ship to quantify the hydrodynamic lift and drag forces. Results of these model tests are presented by Settels [8], see section 2.4.1.
For low wind speeds, it seems to be more efficient to have the wind propulsion placed more at the aft, so that the largest portion of hydrodynamic side force is produced by the rudder. The rudder has a

more favourable lift/drag ratio in comparison to the hull. However, for larger wind speeds, the side forces increase and thus the rudder becomes less effective in generating side forces. Eventually stall of the rudder occurs. Moreover, too large rudder angles should be avoided because it makes the vessel less manoeuvrable.
The importance of engine loading has also been pointed out, where it is stated that the low demanded engine loads, lead to a large specific fuel consumption since engines are designed to operate nominal RPM or at 85% MCR or brake power. This can be observed in the engine envelope from figure 2.10, where for a specific route, the loading of the engine is plotted for every timestep (simulation point) in the engine envelope. It can be seen that for wind-assist, the SFOC is lower for most simulation points in contrast to the SFOC of a conventional configuration without wind propulsion. It can be questioned if it is more fuel efficient to increase ship speed, to operate at a more efficient engine loading.

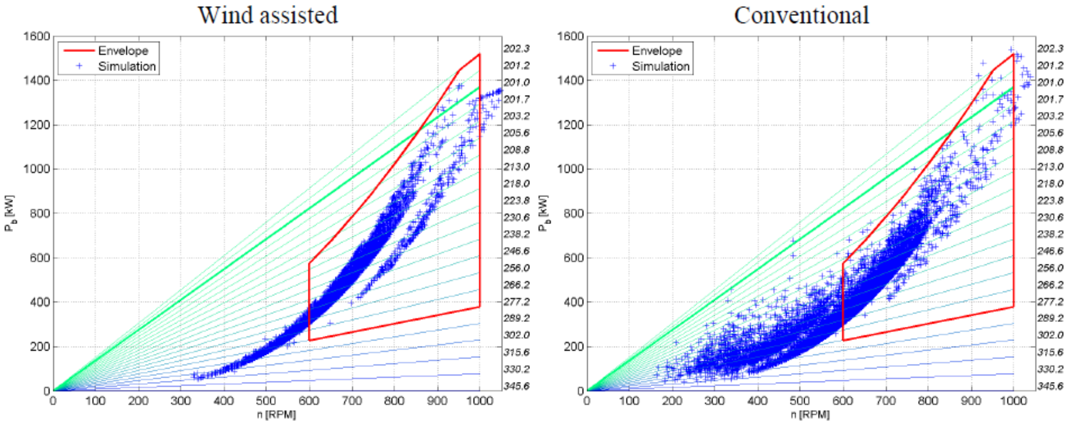

Figure 2.10: Engine diagrams for a conventional and wind-assisted operating vessel, from Eggers [3]

The conclusion from Eggers is that the fuel savings vary (dependent of the route) between 5-10%, which is remarkably lower than the fuel savings calculated by Fuijiwara [2] (averagely 15% savings). Eggers did also account for more realistic modeling criteria such as engine loading, propulsive efficiency, hydrodynamic lift and drag, rudder stall and voyage planning.

2.4 Hydrodynamic Forces for Small Drift Angles

2.4.1 Settels: 'Hydrodynamic Forces of Wind Assisted Propulsion'

Settels [8] has examined the hydrodynamic response of the wind-assisted ship called Wind Hybrid Coaster Vessel, by a numerical model performing CFD computations with RANS. This study investigates the influence of small leeway angles (up to $\beta = 9\,\text{deg}$) on the hydrodynamic lift, drag and the centre of lateral resistance (CLR) at ship speed of $\text{Fn} = 0.14$ and $\text{Fn} = 0.21$. Model test data was available from the Wind Hybrid Coaster Project by MARITIM, which is used to validate CFD computations. Moreover, Settels also incorporates the modelling of appendages such as bilge keels, bow thruster tunnel, rudder and propeller. The influence of the bilge keel and bow thruster tunnel on lateral forces are however less discussed, but the effect of rudder and propeller forces are more elaborated.

The numerical model is built up of a so called RANS-BEM coupling, which is used to make a transition between modeling of the propeller and the ship. BEM (Boundary Element Method) is used to better model the flow at the propeller plane. Further, in order to reduce computational time, the surface is treated as a so called double body configuration where symmetry boundary condition are applied at the free surface, which means there is no wave making drag. The reasoning behind this was to investigate the effect of leeway on the lift induced forces.

The results from CFD are distinguished in three configurations: bare hull results, appended results without propeller (hull + appendages) and appended results with propeller. Comparison between CFD and experiments show that lateral forces can be validated under the presence of large uncertainty errors. For the longitudinal forces and the yaw moment, the numerical model could not be validated.

Under leeway, the propeller also exerts a net lateral forces at the propeller. Settels states that the contribution of the propeller lateral forces with respect to rudder and hull forces is very limited, 5-10% with respect to the delivered thrust. In contrast to the lateral forces produces by rudder and the hull, the lateral force produced by the propeller is negligible which is an important conclusion from this study.

Although the vessel data is not presented because of confidentiality reasons, force coefficients gathered from experiments and CFD can be used for comparison with empirical formulations and other reference vessels. Non-dimensional lift-drag coefficients are presented for the bare hull (and including appendages). Also the rudder force coefficients are treated separately. Additionally, Non dimensional forces are presented for different thrust ratio's and rudder angles, which shows the contribution of rudder forces, related to the total forces of the entire ship. All calculated and measured coefficients are based on a ship model with scale 1 : 16.74, so there has not been accounted for scale effects of full scale.

The Wind Hybrid Coaster has a similar hull shape to the reference vessel in Appendix A. Consequently, the lift and drag force coefficients in this study can be used as a reference vessel to better predict the hydrodynamic lift and drag for the bare hull, including the effect of appendages.

2.4.2 Kramer et al: 'Experimental Study of the Effect of drift angle on a Ship-like Foil'

Kramer investigates a few number of important form parameters of a ship-like foil on the lift and drag forces by performing model tests in the MARINTEK towing tank. This ship-like foil is shown in figure 2.11 and is used to consider simple hull variations, such as as varying the draught or aspect ratio, T/Lpp (for three aspect ratios) and the bottom edge shape (sharp edges and rounded edges). These variations are tested for ship speeds of Fn = 0.1 and Fn = 0.2 to determine how surface effects (wave patterns) play a role in generation the lift and drag. Kramer compares how a physical model, in this case a low aspect ratio ship-like foil, relates to a mathematical models. Most relevant models for small aspect ratio are elliptic wing theory and slender body theory.
The experimental results are presented for all form parameters at two different speeds, where regression lines give a good agreement with the experiments. Remarkable is that the lift forces at small drift angles for sharp edges are a factor two as high compared to a foil with rounded edges, this large difference points out the importance of the midship coefficient. Main conclusion from this study is that the aspect ratios and bottom edge shape are both very important parameters for the lift and induced drag. Only slender body theory approaches the lift forces for small drift angles and larger aspect ratio.

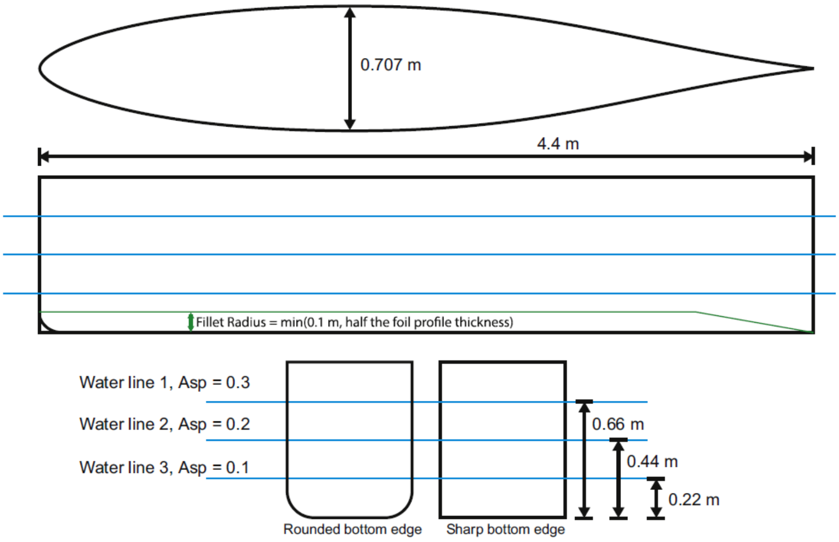

Figure 2.11: Model of a Ship-like foil presented by Kramer [11]

2.5 Manoeuvrability Models

From theory about manoeuvrability, steady state drift forces for a large range of drift angles are examined. These steady side forces under a constant drift angle are generally presented as hydrodynamic derivatives in non-dimensional form. Kijima et al [10] has analysed 13 ship models from captive model tests, where these ship models consist of general cargo, oil tanker, car carrier and RORO ships. Their block coefficients vary from $C_B = 0.556 - 0.831$ and T/L_{pp} varies from 0.040 - 0.073. Kijima comes up with empirical formulas based on these model tests to predict the hydrodynamic derivatives of the bare hull, rudder and propeller to assess the manoeuvring capabilities of ships. The hydrodynamic derivatives are non-dimensionalized by Kijima as follows,

$$C_X, C_Y = \frac{F_{x,H}, F_{y,H}}{\frac{1}{2}\rho T L_{pp} v_s^2}, \qquad C_N = \frac{M_z}{\frac{1}{2}\rho T L_{pp}^2 v_s^2} \tag{2.12}$$

where $F_{x,H}$ and $F_{y,H}$ present forces of the ship hull in longitudinal and lateral direction respectively, M_z is the moment around the vertical axis or yaw moment. Note that Kijima uses other notations for forces and coefficients. Unfortunately, Kijima does not come up with derivatives to calculate the induced drift resistance. Important to mention is that the hydrodynamic derivatives are based on model ships and to determine the full scale forces for a specific ship, these derivatives exclude scale effects and correlation errors. Generally, most manoeuvring models subdivide the lateral force in a linear and nonlinear part. Here, the linear part is due to circular lift, where the body of the hull acts as a foil; the non-linear part is increase of lift due to crossdrag flow, which increases when the vertical velocity component (eq. 2.18) becomes substantially larger. Most manoeuvring models described by Kijima [10] and others, use for the non-dimensional lateral force and moment coefficients of the hull in the general form,

$$C_{Y,H} = C_{Y,lin} + C_{Y,nonlin} \tag{2.13}$$

or expressed as function of drift angle β,

$$C_{Y,H} = C_{Y,\beta}\beta + C_{Y,\beta\beta}\beta|\beta| \tag{2.14}$$

The moment around the vertical axis is stated in equation 2.15,

$$C_{N,H} = C_{N,\beta}\beta + C_{N,\beta\beta}\beta|\beta| \tag{2.15}$$

where subscript, H, refers to the bare hull.

Other authors who describe hydrodynamic derivatives for bare hull and rudder forces are Kornev [14] and work from Ankundinov [12] presented by Panel H-10 [13]. Panel H-10 comes up with empirical formulation to calculate the induced drift resistance for steady drift angles. However, the forces are made non-dimensional in a different way, see equation 2.17. This equation was also used by van Tuijl [5], but a mistake is made in the implementation of the formula. The hydrodynamic derivative for induced drift resistance is given in eq. 2.16.

$$X'_{vv} = 12 \cdot \left[0.070 \left(\frac{B}{L_{pp}}\right)^2 \left(\frac{T}{L_{pp}}\right) \left(1 + 0.8 \cdot \left(\frac{B}{L_{pp}}\right)^2\right)^2\right] \tag{2.16}$$

The induced drift resistance is then calculated by,

$$X_H = X'_{vv} \cdot v_{s,y}|v_{s,y}| \cdot \frac{1}{2}\rho L_{pp}^2 \tag{2.17}$$

where $v_{s,y}$ is the velocity component in y-direction due to drift angle, β, becomes,

$$v_{s,y} = v_s \cdot sin(\beta) \tag{2.18}$$

Kornev [14] defines empirical formulation to determine the steady drift forces and moments based on various series of experimental measurements presented by various authors. However, the formula to determine the induced drift resistance and yaw moment, are not clearly presented. In section 2.6 the manoeuvring models described in this section are compared with experimental data of the Wind Hybrid Coaster by Settels [8] and experiments of a ship-like foil by Kramer [11]. From this comparison, conclusions can be drawn regarding the accuracy of the presented empirical expressions.

2.6 Comparison of Hydrodynamic Derivatives

In section 2.5, literature for manoeuvring models are presented, and in section 2.4.1 and 2.4.2 studies regarding small drift angles of ships are described. By implementing empirical formulations from literature, a rapid assessment on the hydrodynamic side force, moment and induced resistance can be performed for a ship using simple hull characteristics. These empirical formulas can be implemented in the equation of motion, see eq. $3.1 - 3.3$, which finally give the resulting drift angle, β, and rudder angle, δ. This section compares empirical formulations to quantify what methods are the most accurate and reliable. This comparison is presented in a polar diagram in figure 3.2 of section 3.2 where the net resistance is presented for all incoming wind angles. This polar plot is a pre-stage of the final power prediction program, which is expanded to a Fuel Prediction Program in section 3.4.

For the reference vessel, the hydrodynamic derivatives C_X, C_Y, C_N are calculated for induced drift resistance, side force and yaw moment respectively and presented in figure 2.12 - 2.14. To indicate if the calculated values are realistic, a comparison is made between hydrodynamic derivatives of other reference vessels based on model test results.

2.6.1 Induced Drift Resistance

The induced drift resistance R_i is made non-dimensional to compare with reference ships. The hydrodynamic derivative for induced drift resistance or the drift resistance coefficient, C_X, is defined equation 2.19.

$$C_X = \frac{R_i}{\frac{1}{2}\rho v_s^2 L_{pp} T} \tag{2.19}$$

The drift resistance coefficient, C_X, is calculated by SNAME [13] and ISO standard [19] and is presented in figure 2.12. Although the formula by ISO standards, is not clearly justified by references, this formula gives the largest induced resistance and matches the best with reference ships. In figure 2.12, the resistance coefficient C_X is compared between reference vessels and empirical formulas. It can be seen that SNAME gives rather low values for C_X, compared to resistance coefficient of reference ships. However, for small drift angles $\beta < 3°$, coefficient C_X is for all reference ships below $C_X < 0.3 \cdot 10^-3$ which is less than 2.5 % of the bare hull resistance, R_0.

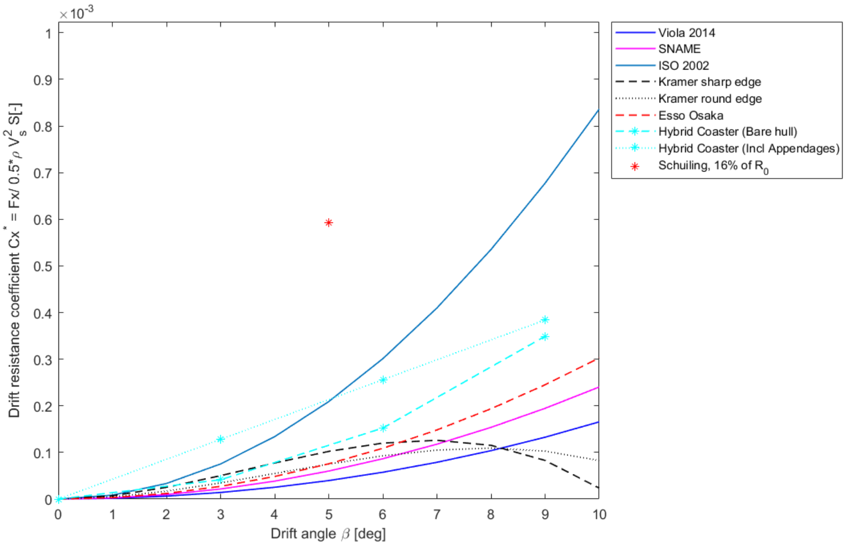

Figure 2.12: Comparison for induced drift resistance coefficient of the bare hull, $C_{X,h}$

2.6.2 Side Forces under Drift

In figure 2.13, the lateral force coefficient of the bare hull of reference ship, C_Y, is calculated by eq. 2.20, using empirical expressions from several authors: Kijima [10], Kornev [14], Kramer [11] and SNAME [13].

$$C_Y = \frac{F_{y,H}}{\frac{1}{2}\rho V_s^2 L_{pp} T} \tag{2.20}$$

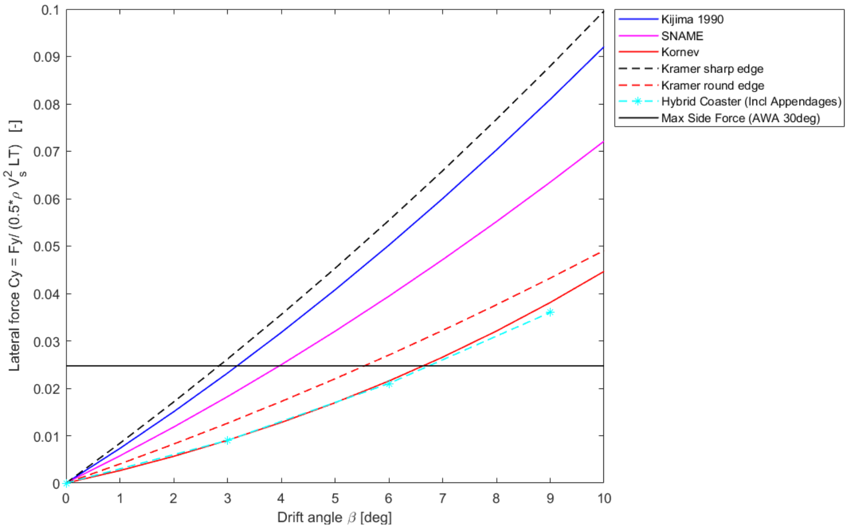

Figure 2.13: Comparison for lateral force coefficient of the bare hull, $C_{Y,h}$

.

From figure 2.13, it can clearly be seen that there is a large difference between the applied method. To decide what method would be the most accurate to apply, a comparison is made with other reference vessels.
From the ship-like foil of Kramer in section 2.4.2, it is concluded that the side force produced by the hull is mainly dependent of T/L_{pp} and midship coefficient, C_M. The Wind Hybrid Coaster from Settels [8] is included in figure 2.13 which has a similar block coefficient, but lower draft to length ratio (or aspect ratio), T/L_{pp}, and lower midship coefficient compared to the reference ship of Conoship. In figure 2.13, the lateral coefficient, C_Y, shows a different pattern for all presented methods (Kornev, SNAME and Kijima). Kornev's method gives slightly higher side force coefficients than the side force coefficients of the wind hybrid coaster. Without proper CFD calculations or model tests, it can not be concluded which method is the most reliable. It is expected that reference ship has C_Y values close to the wind hybrid coaster, but this may be slightly higher due to a larger aspect ratio T/L_{pp} and larger midship coefficient C_M. Methods by SNAME and Kijima give respectively about 1.5 and 2 times higher side forces compared to Kornev and seem to be far overestimated. This large deviation may be caused by the fact that SNAME and Kijima approximate their empirical formulas on larger drift angles and therefore capture not the behaviour of side forces for small drift angles, but this is a hypothesis.

2.6.3 Yawing Moment

In figure 2.14, the yawing moment of the hull, M_z is calculated by Kijima [10] in equation 2.12 and is made non-dimensional by $\frac{1}{2}\rho v_s^2 L_{pp}^2 T$ to obtain the yawing moment coefficient $C_{N,H}$ in equation 2.21.

$$C_{N,H} = \frac{M_z}{\frac{1}{2}\rho V_s^2 L_{pp} T} \tag{2.21}$$

Methods of Kornev and SNAME are excluded because Kornev does not give a clear description of the calculated yaw moment and SNAME gives unrealistic high values for the yaw moment, which indicates that a mistake is made in the formula. The reference vessel of the Wind Hybrid Coaster is also included in figure 2.14 to make a comparison and conclude if the applied method of Kijima gives similar results. It can be seen that the deviation between the method of Kijima and the Wind Hybrid coaster are significant.

However, this is the only empirical formula found that gives an empirical relation for the yawing moment coefficient $C_{N,H}$.

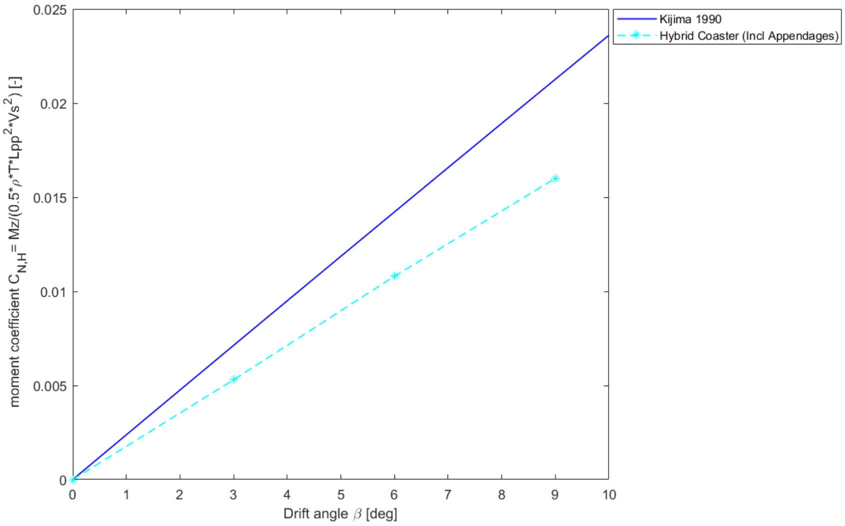

Figure 2.14: Comparison for vertical moment coefficient of the bare hull, $C_{N,H}$

2.7 Rudder Forces

For a vessel using wind-propulsion, the rudder is essential to balance the forces in y-direction due to the large uprighting moment of the ship. It is already observed from section 2.6.3 that the yaw moment is large, where position of x_{CLR} is always in front of the vessel. The center of lateral resistance is defined in equation 2.22.

$$x_{CLR} = \frac{M_z}{F_{y,H}} \tag{2.22}$$

Consequently, a certain rudder angle is required, which will cause additional rudder resistance, R_{rudder}. Many authors come up with expression to calculate rudder forces, for example Kornev [14] and Kijima [10]. A comparison of the rudder forces is made between the method of Kijima and Kornev. Considering the empirical formulas for rudder forces by Kijima, the expression for effective rudder inflow speed v_{eff} could not be calculated with full confidence, since the coefficient C, for starboard or portside is not given in the publication. Consequently, a different expression for v_{eff} is selected from ISO [19] to calculate the rudder forces from empirical formulas from Kijima. Rudder forces by Kornev and Kijima have the general form given in equation 2.23 and 2.24. Both authors, do not account for stall of the rudder blade in the empirical formulas.

$$R_{rudder} = C_{x,rudder} \cdot \frac{1}{2}\rho v_{eff}^2 A_R \tag{2.23}$$

$$F_{y,rudder} = C_{y,rudder} \cdot \frac{1}{2}\rho v_{eff}^2 A_R \tag{2.24}$$

where v_{eff} is the effective rudder inflow speed, A_R is the aspect ratio of the rudder blade.

In figure 2.15, the forces of the rudder in x,y- direction are calculated for rudder angle, δ according to the method of Kornev and Kijima. A change of angle of attack due to drift is not included, but this effect is negligible for very small drift angles, $\beta < 3.5°$. It can be seen that for small rudder angle, $\delta < 6°$, the ratio of $F_{y,rudder}/F_{x,rudder}$ is small, and increases significantly for larger rudder angles. The method of Kijima gives remarkably higher side forces $F_{y,rudder}$ compared to the method of Kornev for the same rudder angle δ. This difference in side force generation, gives a significant lower rudder resistance when the method of Kijima is used. As a conservative and safe assumption, the method of Kornev is adopted in the FPP, which is discussed in chapter 3.

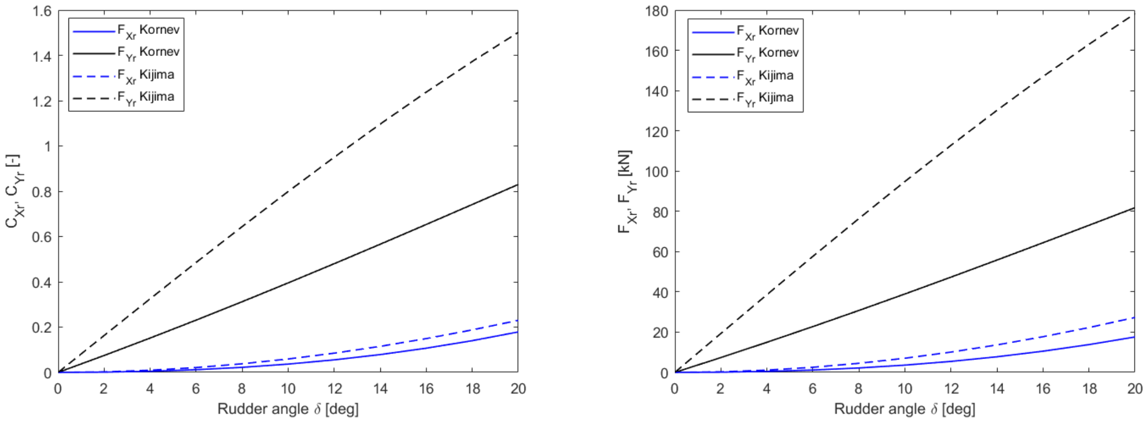

(a) (b)

Figure 2.15: Rudder coefficients (a) and rudder forces (b) according to Kornev [14] and Kijima [10].

2.8 Propeller Efficiency Under Drift Angle

2.8.1 Schuiling: 'Effect of Drift angle on Propulsion Performance'

Schuiling [6] has performed a numerical study on the KRISO Container Ship (KCS) with CFD to see how a leeway or drift angle affects the resistance and propulsive performance. Schuiling also makes a distinction between leeway from portside and starboard, which results in a different propeller efficiency. The total resistance has been computed for a drift angle of 5 degrees without rudder. As a result, the total resistance increases by 16.5 % where the largest contribution to this increase can be subscribed to pressure resistance (14.6%) and the other part is viscous resistance or skin friction. The skin friction however, might be lower due to numerical ventilation which presents the fraction of air volume near the hull surface. The main conclusion is that the induced resistance due to drift should be in the order of 15 %.

Furthermore, the effect of the wake field on the propeller efficiency when sailing under leeway has been analysed. The leeway angle changes the axial and tangential velocity at the propeller plane. The propeller efficiency increases when the thrust-torque ratio increases (at the same torque,Q, more thrust T is produced), this can clearly be seen in figure 2.17. The thrust increases in magnitude when the angle of attack increases. This angle of attack increases when axial velocity (V_x) decreases, and/or if the tangential velocity, V_T, increases.

The nominal wake is computed for two incoming drift angles under presence of a propeller blade, under 5 degrees leeway at starboard port side. In this nominal wake, the tangential and axial velocity components are analysed and give useful insight in the propeller efficiency for both drift angles.

At starboard drift, the nominal wake at the propeller plane has been presented by Schuiling, which is presented in figure 2.16. As can be seen from figure 2.16, the axial velocity increases at starboard side, while a decrease in axial velocity is observed at portside. Consequently, the thrust-torque ratio increases at port side plane of the propeller while at starboard, the thrust-torque ratio decreases. As a result, the wake factor decreases from 0.753 at zero drift to 0.728 at 5 degrees starboard drift, which leads to an overall increase in hull efficiency, due to a more favourable advance velocity v_A. The propeller efficiency, η_P is defined by the ratio of thrust power P_T that the propeller delivers to the water and the delivered power to the propeller P_D, according to equation 2.25.

$$\eta_P = \frac{P_T}{P_D} = \eta_O \cdot \eta_R \tag{2.25}$$

The tangential velocity in the wake is also changed considerably, which also has its influence on the propeller efficiency.

As a result, Schuiling reports that for a right-handed propeller under starboard drift, the propeller efficiency increases by 2.1% under the same rotation rate for the propeller compared to zero drift. However, the total resistance increases by 16.5%, and therefore the required thrust is much higher. The total delivered thrust has to increase by 24% compared to the case with zero drift. When the drift angle is from port side, the propeller efficiency decreases as a result of unfavourable tangential and axial velocities in

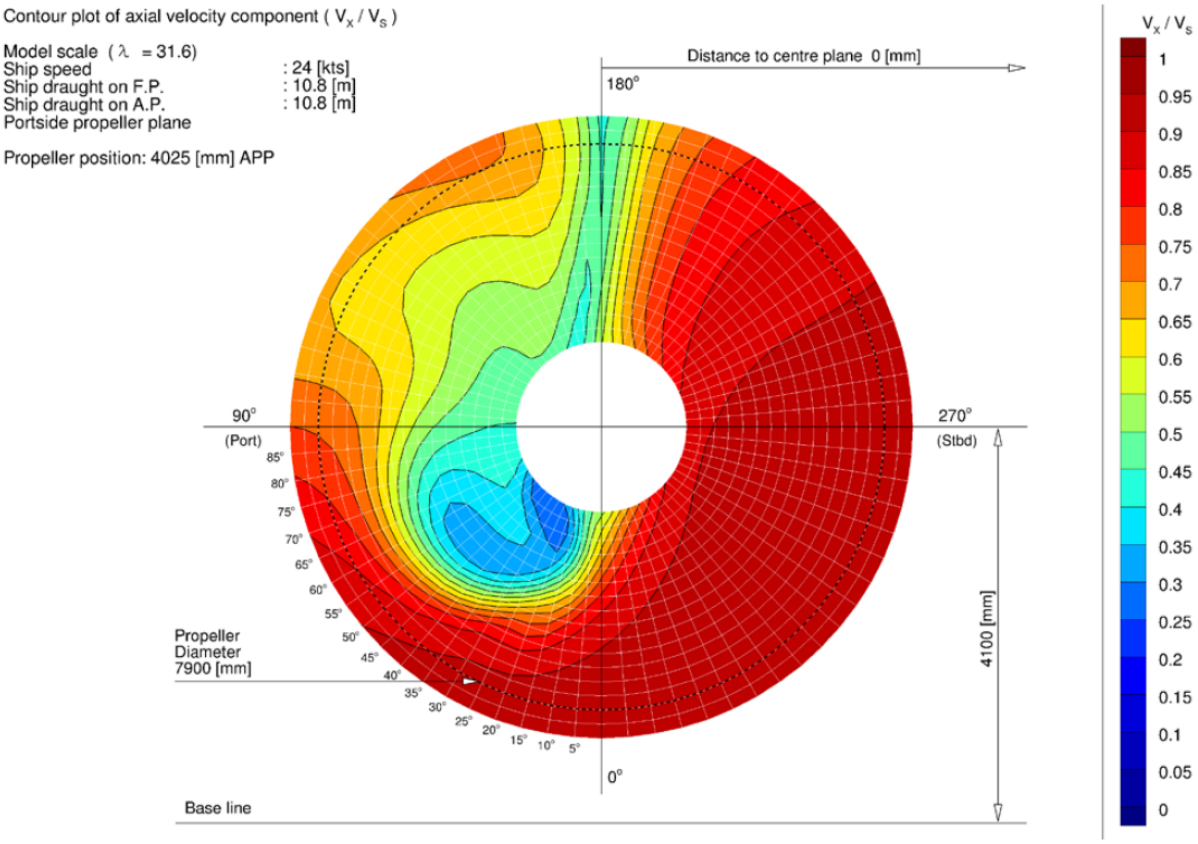

Figure 2.16: Wake field at the propeller plane under a drift angle of $\beta = 5°$ presented by Schuiling [6]

the wake. The propeller efficiency decreases with -2.4%, and to reach self-propulsion point, the delivered power needs to be increased by approximately 30.4%.

This research shows that the effect of propeller efficiency is an important aspect to keep in mind when a ship is sailing under a drift angle and which always applies for wind assisted propulsion. Also, this CFD analysis shows that the induced resistance due to drift is very large for this particular container vessel. The calculated drift resistance of 16% of the total resistance seems to be rather high, compared to other investigation about hydrodynamic lift and drag for the Wind hybrid Coaster by Settels [8], the ship-like foil from Kramer [11] and other manoeuvring prediction models.

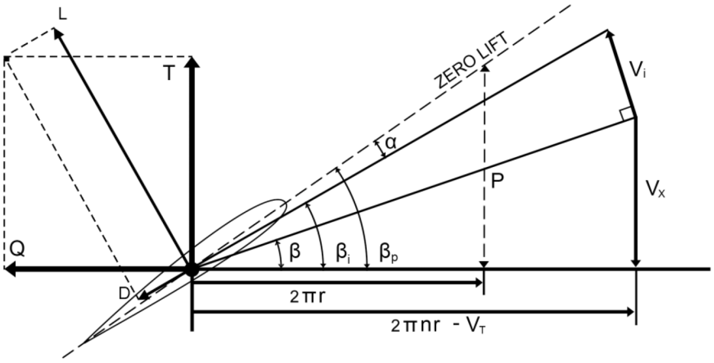

Figure 2.17: Thrust and Torque of a propeller blade by Schuiling [6]

Chapter 3

Fuel Prediction Program

This chapter presents a Power Prediction Program (PPP) and Fuel Prediction Program (FPP), which is based on solving the equation of motion with Turbosail forces, hydrodynamic forces, propulsion efficiencies and the specific fuel oil consumption (SFOC). The FPP shows the reduced fuel consumption for 360 degrees of true wind angle (TWA). The equation of motion behind the model are explained and a comparison is made between different wind velocities. The propeller efficiency is analysed in a open water diagram by matching the demanded thrust of the ship and delivered thrust by the propeller.

3.1 Equation of Motion

The equation of motion for a motor-sailing vessel is already presented by Viola et al [7] in equation 2.8 − 2.10. The free body diagram is drawn in figure 3.1 for forces in x,y- direction for a ship installed with 4 WCU's. From the free body diagram, the equation of motion can be derived, see eq. 3.1 − 3.3.

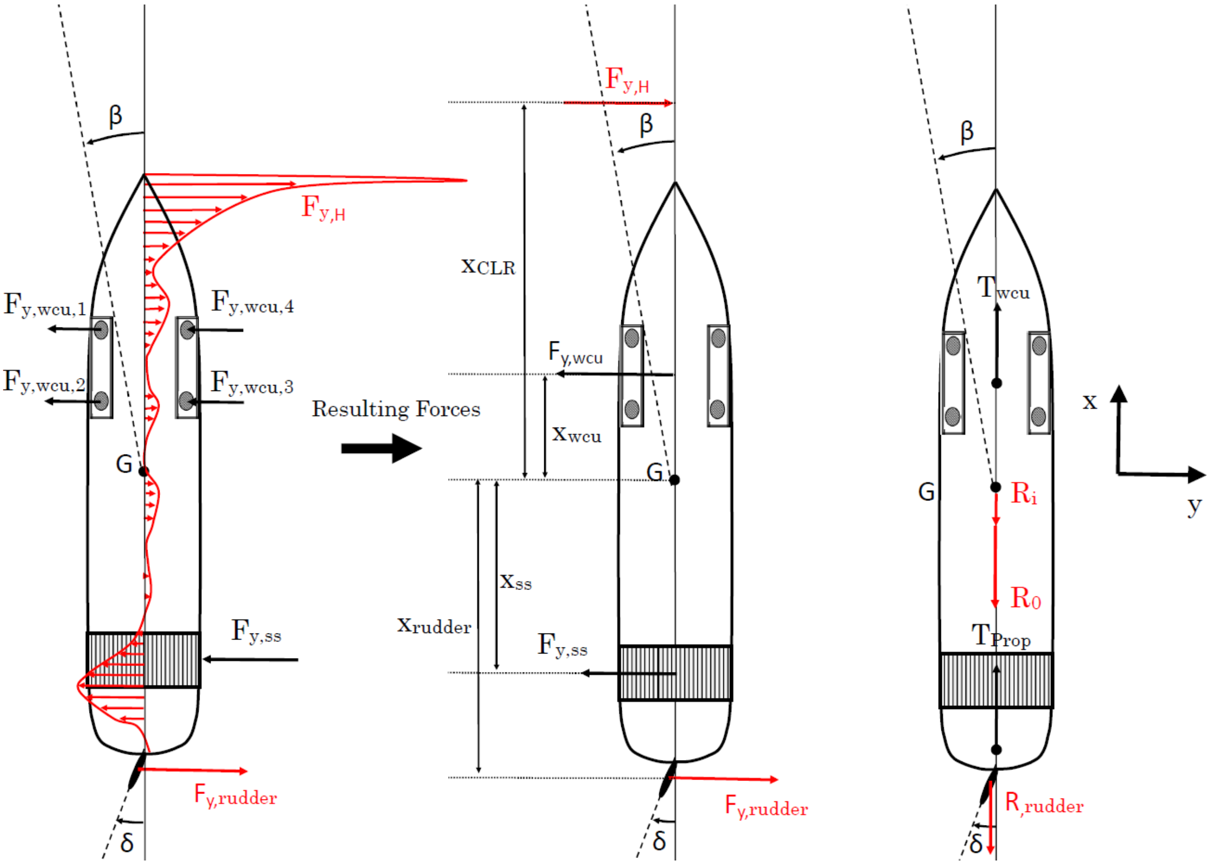

Figure 3.1: Free body diagram for x,y-forces

$$\sum F_x = 0; \qquad T_{prop} + T_{wcu} - R_0 - R_{rudder} - R_i - R_{ss} = 0 \tag{3.1}$$

$$\sum F_y = 0; \qquad -F_{y,wcu} - F_{ss} + F_{y,rudder} + F_{y,H} = 0 \tag{3.2}$$

$$\sum M_z = 0; \qquad F_{y,wcu} \cdot x_{wcu} - F_{y,ss} \cdot x_{ss} + F_{y,rudder} \cdot x_{rudder} - F_{y,H} \cdot x_{CLR} = 0 \tag{3.3}$$

From eq. 3.2 and 3.3, the side force of the rudder, $F_{y,rudder}$, and hydrodynamic side force of the hull $F_{y,H}$, can be solved so that the drift angle β and rudder angle δ can be calculated. Substitution of equation 3.2 in to 3.3 gives an equation in the form $ax^2 + bx + c = 0$, which can easily be solved.

From section 2.6, it has been described what methods give the best approximation for the hydrodynamic derivatives, C_X,C_Y,C_N. The induced resistance, R_i, is calculated using expression ISO 2002 standards [19], where the R_i is calculated by the general form in equation 3.4.

$$R_i = C_{X,\beta\beta} \cdot \beta^2 \cdot \frac{1}{2}\rho v_s^2 T \tag{3.4}$$

The hydrodynamic side force for the bare hull $F_{y,H}$, is calculated using the empirical formula presented by Kornev [14], which has the general form,

$$F_{y,H} = (C_{Y,\beta} \cdot \beta + C_{Y,\beta\beta} \cdot \beta^2)\frac{1}{2}\rho v_s^2 L_{pp} T \tag{3.5}$$

The yaw moment M_z of the hull, is approximated Kijima [10], which has the general form,

$$M_z = (C_{N,\beta}\beta + C_{N,\beta\beta} \cdot \beta^2)\frac{1}{2}\rho v_s^2 L_{pp}^2 T \tag{3.6}$$

Turbosail forces in x,y-direction of the ship can easily be derived from lift and drag forces from equation 2.5 and 2.6, the apparent wind speed, U_{AW}, and apparent wind angle, α_{AW}. The lift and drag coefficients are based on figure 2.7 which depict the lift-drag coefficients as function of α for a finite aspect ratio Turbosail of $A_R = 4$. From this figure, the maximum lift is $C_L = 6.8$ and the corresponding drag is $C_D = 1.95$. The aspect ratio of $A_R = 4$ is slightly lower compared to the aspect ratio of the Turbosail considered in this research study of $A_R = 5.5$. In fact, the lift and drag should improve for the higher aspect ratio of $A_R = 5.5$ where the lift becomes higher and the drag is reduced. The driving force coefficient for each Turbosail is calculated by equation 3.7. In the research question 1 of section 1.4, it chosen to calculate the Turbosail forces for 2 WCU of each consisting 2 Turbosails with a span of 11m.

$$C_{X,turbo} = C_L \cdot sin(\alpha_{AW}) - C_D \cdot cos(\alpha_{AW}) \tag{3.7}$$

The total driving force of all Turbosails, denoted with $F_{x,wcu}$ can be calculated by equation 3.8.

$$F_{x,wcu} = C_{X,turbo} \cdot \frac{1}{2}\rho_{air} U_{AW}^2 S_{turbo} \cdot n_{turbo} \cdot C_{turbo} \tag{3.8}$$

where n_{turbo} are the number of Turbosails in service at maximum power, C_{turbo} is the factor to compensate for power reduction of the Turbosails due negative (or positive) interaction of the Turbosails. This factor is unknown and should be investigated if an accurate assessment of the FPP is desired.

Similarly, the side force coefficient of the Turbosail is calculcated with equation 3.9.

$$C_{Y,turbo} = C_L \cdot cos(\alpha_{WA}) + C_D \cdot sin(\alpha_{AW}) \tag{3.9}$$

Then, the total side forces of all Turbosails can be expressed as,

$$F_{y,wcu} = C_{Y,turbo} \cdot \frac{1}{2}\rho_{air} U_{AW}^2 S_{turbo} \cdot n_{turbo} \cdot C_{turbo} \tag{3.10}$$

Rudder forces are expressed in section 2.7, according to eq. 2.23 and 2.24.

$$F_{x,rudder} = C_{x,rudder} \cdot \frac{1}{2}\rho v_{eff}^2 A_R \tag{2.23}$$

$$F_{y,rudder} = C_{y,rudder} \cdot \frac{1}{2}\rho v_{eff}^2 A_R \tag{2.24}$$

The air resistance and side force of the superstructure, respectively R_{ss} and $F_{y,ss}$ have not been calculated yet, but this component would be wise to include since the rudder resistance is increasing quadratic for the amount generated side forces.

3.1.1 Stability Criteria

When Turbosails are in service, the maximum side forces are restricted by the maximum stability moment of $M_{st} = 3000kNm$, which is found from the feasibility study [15] of section 2.1.1. The moment due to each Turbosail is calculated by multiplying side forces with arm between the centre of gravity and the centre of effort of the Turbosail. The centre of gravity is assumed to be located at $KG = 0.5 \cdot T$. For a WCU with a length of 11m, the length from waterline to the center of effort becomes, $s_{wcu} = 15.5m$. The wind moment due to the hull without WCU's is calculated by equation 3.11.

$$M_{ss} = \frac{1}{2}\rho_{air} C_{D,hull} U_{AW}^2 A_{lat} \sin(\alpha_{AW}) s_{ss} \tag{3.11}$$

Where A_{lat} is the lateral projected area of the superstructure, U_{AW} is the apparent wind speed, α_{AW} is the apparent wind angle and s_{ss} is the vertical distance between the centre of effort and KG. The maximum side force of a total number of WCU's, n_{wcu}, can be calculated using eq. 3.13 and 3.11. From stability point of view, the maximum side forces may not exceed 10 degrees of heel angle, see equation 3.12.

$$M_{ss} + F_{y,wcu} s_{wcu} n_{wcu} < M_{st,10^\circ} \tag{3.12}$$

For an apparent wind speed of 20 m/s and an apparent wind angle of 30 degrees, the total moment due to wind forces is calculated to be 2300kNm for 2 WCUs containing each 2 Turbosails of each 11m high. The maximum side forces in this situation are $F_y = 155kN$.

The total external wind moment of the ship is a summation of the moment induced by the side forces of the superstructure, M_{ss}, and secondly the moment caused by side forces of the WCU's, M_{wcu}. Also the moment term arises from the hydrodynamic forces of the hull and rudder, M_H, M_R respectively. The moment equation is written in equation 3.13.

$$M_{st} = M_{ss} + M_{wcu} + M_R + M_H \tag{3.13}$$

Where M_{st} is the stabilizing moment of the ship according to equation

$$M_{st} = \rho g \nabla GM sin(\phi) \tag{3.14}$$

3.2 Results

3.2.1 Sensitivity for Hydrodynamic Side Forces

The sensitivity of the hydrodynamic side forces of the hull on the performance of the FPP model is studied by considering two empirical relations for the hydrodynamic side force, $F_{y,H}$. In this way, it can be observed what is the importance of determining the hydrodynamic side forces with more accuracy. As a first case, identified by case 1, the original expression for the side force by Kornev [14] in equation 3.5 is selected, such that the case 1 reads,

$$F_{y1,H} = F_{y,H} \tag{3.15}$$

As a second condition, identified by case 2, it is assumed that the ship produces 35% less hydrodynamic side forces. The hydrodynamic side force for case 2 is defined as

$$F_{y2,H} = 0.65 \cdot F_{y1,H} \tag{3.16}$$

For wind-assistance, this assumption negatively influences the thrust benefit from the Turbosails. Hence, the rudder needs to produce larger side forces, $F_{y,rudder}$, to balance the yaw moment. Consequently, there will be a higher leeway angle, and the centre of effort x_{CLR} will be located more forward in front of the ship. All other quantities such as yaw moment, rudder forces, induced resistance, etc are computed for case 1 and 2 identically. To quantify how large the benefit of wind-assistance by Turbosails is, the comparison between hydrodynamic side forces of the hull $F_{y1,H}$ and $F_{y2,H}$ can be expressed in terms of new net resistance of the ship, R_1. The net resistance can be found in equation 3.17 by rewriting equation 3.1 and is equal to the effective thrust of the propeller, T_{prop}, after thrust deduction factor t.

$$R_1 = R_0 + R_i + R_{rudder} + R_{ss} - T_{wcu} = T_{prop}(1-t) \tag{3.17}$$

In non-dimensional form, the net resistance can be divided by the bare hull resistance at zero drift, R_0 and becomes R_1/R_0. The thrust benefit of equation 2.11 can easily be rewritten in equation 3.18

$$TB = 1 - \left(\frac{R_1}{R_0}\right) \tag{3.18}$$

The equation of motion in eq. 3.1 − 3.3 for $\sum F_x, \sum F_y, \sum M_z = 0$ are solved, which gives the resulting drift and rudder angle. For every true wind angle, the equation of motion is calculated for a wind speed of $U_{AW} = 14m/s$, with steps of 30 degrees, presented in table 3.1 and 3.2, which gives an overview of all force components and wind variables.

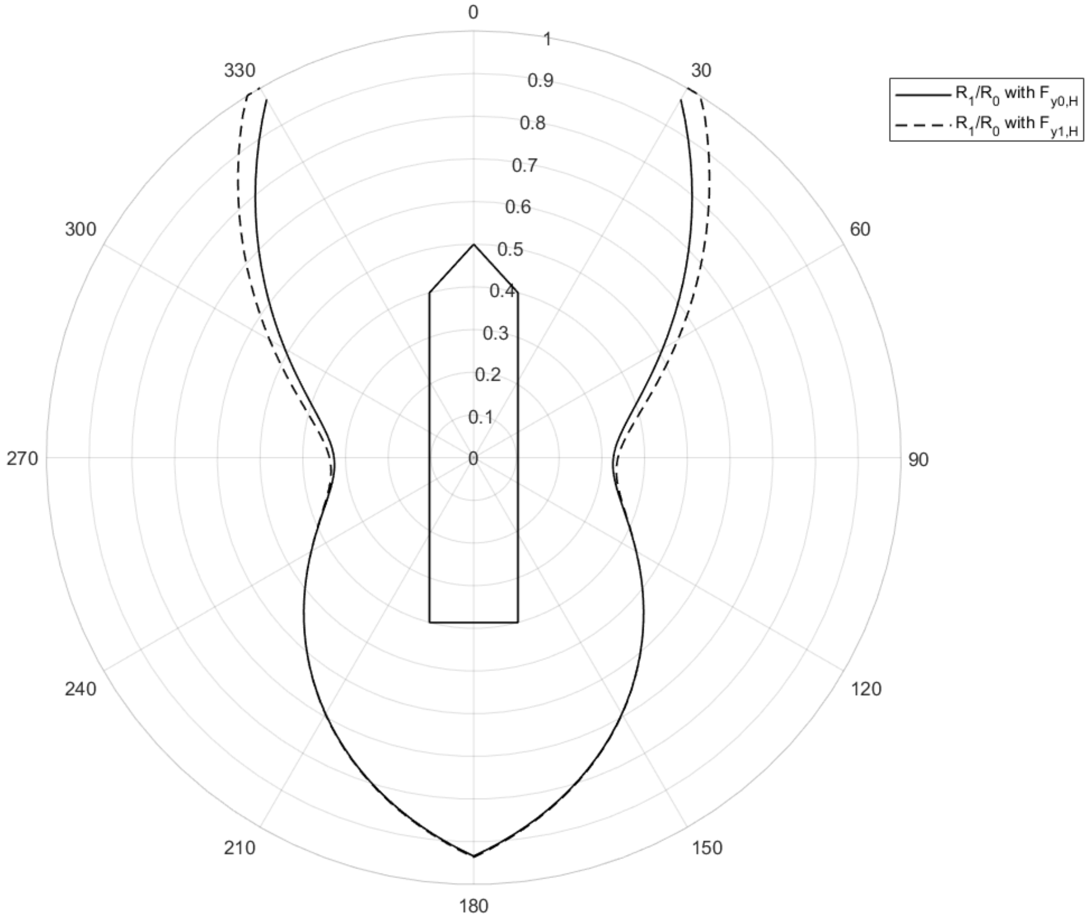

Figure 3.2: Polar plot of net resistance for a true wind speed of V_{wind} = 14 m/s comparing differences between hydrodynamic side forces of Kornev for case 1 and 2.

Table 3.1: Results net resistance at $V_{wind} = 14m/s$, comparing the sensitivity of the hydrodynamic side force of the hull for case 1 and 2.

TWA [°]	α_{AW} [°]	U_{AW} [m/s]	Case 1 β [°]	Case 2 β [°]	Case 1 x_{clr} [m]	Case 2 x_{clr} [m]	Case 1 $F_{y,H}$ [kN]	Case 2 $F_{y,H}$ [kN]	Case 1 $F_{y,rudder}$ [kN]	Case 2 $F_{y,rudder}$ [kN]
30	21	19.1	3.2	3.7	68.8	102.9	76.4	58.5	59.7	77.6
60	44	17.5	2.4	2.8	72.3	108.8	55.1	41.8	46.2	59.5
90	68	15.1	1.3	1.5	78.2	118.8	26.9	20.1	25.0	31.8
120	96	12.2	0.2	0.3	84.4	129.6	4.4	3.2	4.5	5.6
150	133	9.5	0.4	0.4	83.4	127.7	7.7	5.7	7.9	9.9
180	180	8.3	0.6	0.7	81.9	125.2	12.6	9.4	12.5	15.8

The differences between the calculation method for $F_{y,H}$ in case 1 and 2 for the non-dimensional net resistance R_1/R_0 are depicted in the polar diagram of figure 3.2 for all 360 degrees round true wind angles. The higher thrust benefit, or the lowest ratio for R_1/R_0 is realised for beam winds at around $TWA = 90°$ or at portside at $TWA = 270°$ where the net resistance is reduced by 66-67%, depending on the used expression for $F_{y,H}$ in case 1 and 2. For a $TWA < 30°$, the net resistance R_1 becomes larger

Table 3.2: Results net resistance at $V_{wind} = 14m/s$, comparing the sensitivity of the hydrodynamic side force of the hull for case 1 and 2.

TWA [°]	Case 1,2 T_{turbo} [kN]	Case 1 R_i [kN]	Case 2 R_i [kN]	Case 1 R_{rudder} [kN]	Case 2 R_{rudder} [kN]	Case 1 δ [°]	Case 2 δ [°]	Case 1 R_1/R_0 [-]	Case 2 R_1/R_0 [-]
30	14.4	2.7	3.6	8.7	14.8	15	19	0.97	1.00
60	54.6	1.6	2.1	5.1	8.6	12	15	0.51	0.55
90	67.8	0.4	0.6	1.4	2.3	6.6	8.2	0.33	0.34
120	55.0	0.0	0.0	0.0	0.1	1.2	1.5	0.44	0.44
150	30.2	0.0	0.1	0.1	0.2	2.1	2.7	0.69	0.69
180	6.9	0.1	0.1	0.3	0.5	3.4	4.2	0.93	0.94

than the bare hull resistance, R_0 which means that the thrust benefit TB from Turbosail described in equation 2.11 add resistance instead of reducing the resistance.

A comparison between the differences of case 1 and 2 is also depicted in table 3.1 and 3.2, which shows clearly that the more conservative method of case 2 leads to less favourable net resistance for cross to beam winds (TWA = $[30° - 90°]$). It can be seen that the drift angles deviate slightly, with a maximum of $\Delta\beta = 0.5°$ at TWA = 30°. The side forces generated by the hull are approximately 30% (of the total side force) larger for case 1 compared to case 2 for true wind angles from 30 - 90 degrees. Consequently, the required side force of the rudder $F_{y,rudder}$, to balance the Turbosail forces, are much higher by applying the expression for hydrodynamic side forces $F_{y2,H}$ of case 2. This results in a much higher rudder resistance R_{rudder}. For small rudder angles δ, the rudder is effective in generating side forces, however, for larger rudder angles the rudder resistance grows quadratic, see figure 2.15. The rudder forces are simply calculated by selected by empirical formula proposed by Kornev in equation 2.23 and 2.24. From these results, it can be seen that rudder forces are very important in the performance of a ship using wind propulsion. Therefore, it is recommended to calculate the rudder forces using more reliable and accurate methods.
In contrast to the rudder resistance, the induced resistance due to leeway R_i, is approximately 2-3 times lower. At TWA = 30°, the maximum induced resistance is $R_i = 3.7$ kN since the leeway angle is restricted to $\beta < 3.7°$. Consequently, determining the induced resistance with higher accuracy is of second concern, in contrast to the rudder forces.

3.2.2 Polar plot for Net Resistance

Using the original expression for hydrodynamic side forces of the hull of case 1 in equation 3.15, the net resistance R_1 is calculated by equation 3.17 and is presented in a polar diagram for all 360 degrees round true wind angles, see figure 3.3. The net resistance is calculated for different true wind velocities, $U_{TW} = [0,\ 6,\ 10,\ 14]$ m/s. It can clearly be seen that at $U_{TW} = 0$ m/s, the net resistance is constant for all TWA, and is slightly increased compared to the bare hull resistance, due to the wind resistance from Turbosails. Modeling of wind resistance due to superstructure would still be wise to model, since rudder forces increase quadratic with the generated side forces. For true wind speeds of 6, 10 and 14 m/s, the net resistance decreases, starting at a TWA of 30 degrees and reaches a minimum at a TWA of 90 degrees. At $U_{TW} = 10$ m/s, the net resistance becomes $R_1 = 64$ kN, a decrease of 35%. For a higher wind speed of $U_{TW} = 14$ m/s, the net resistance improves even further to $R_i = 33$ kN, an extraordinary reduction of 66%.

However, in the calculation for net resistance, the most ideal lift-drag coefficients are considered, which can be lower since it is not possible to always have the best angle of attack, α. Also α may be effected by the roll motion of the ship, which needs to be accounted for. Furthermore, negative (or positive) interaction effects of multiple Turbosails are not incorporated and should be accounted for to make an accurate power prediction program.
This first polar plot for net resistance needs to be expanded to the delivered power P_D of the propeller. To reduce P_D, the CP-propeller of the ship is given a different pitch ratio, which may lead to another propeller efficiency, this is discussed in section 3.3. The delivered power is related to brake power, P_B resulting in a Power Prediction Program. At last, the PPP is coupled to the SFOC of the engine in section 3.4 to find the fuel consumption.

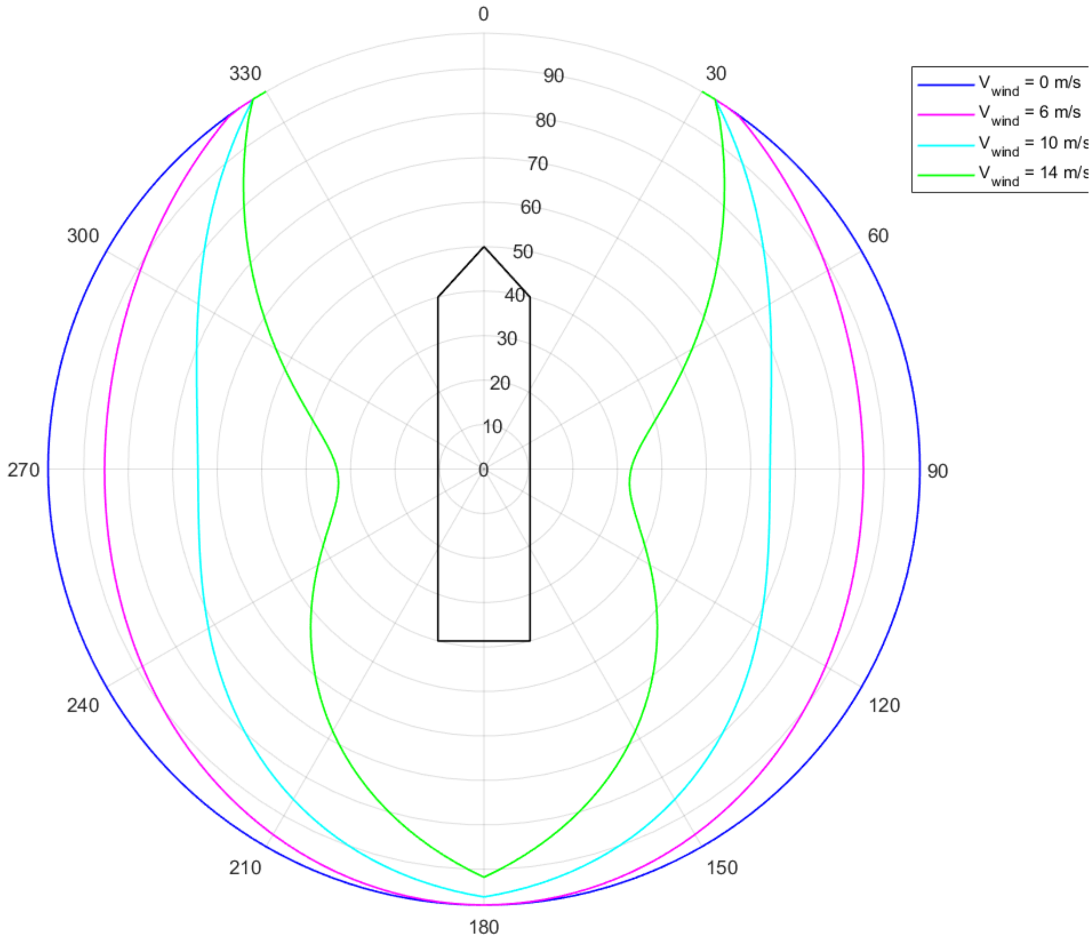

Figure 3.3: PPP plot of the net resistance in [kN] for several wind speeds.

3.3 Matching of the Propeller

This section investigates how the propeller will operate when the ship turns over to wind-assisted propulsion. In the feasibility study of section 2.1.1, theory about matching of the propeller is explained. The reader should be familiar with advance ratio J in equation 2.2 and delivered power P_D in equation 2.1. It should be noted that the effective power P_E changes due to wind-assistance, where the bare hull resistance R_0, without WASP is replaced by the net resistance R_1, with WASP. Then, the effective power, P_E can be expressed in equation 3.19

$$P_E = R_1 \cdot v_s \tag{3.19}$$

The engine of the reference vessel is a four stroke turbocharged diesel engine, delivering a maximum brake power of 2000kW. For power supply on board, a constant power of 100kW needs to be available and is generated with a power take off (PTO) coupled to the engine. To deliver this power for the PTO, a contant RPM of the engine is required, which is found at the nominal rotation speed of the engine at $n_e = 750$ RPM.

To reduce the delivered power to the propeller (to decrease the ship's speed) at a constant shaft RPM, the ship is equipped with a controllable pitch propeller (CP-propeller). The amount of delivered thrust by the propeller is then determined by the pitch setting or pitch ratio of the propeller.
When the ship generates additional thrust with Turbosails, the delivered power to the propeller needs to be decreased, when constant ship speed is attained. This can be realized by two configurations on the ship.

- Configuration 1: the engine and shaft RPM are set to nominal RPM, to ensure generation of power for the PTO. Then, the delivered power of the propeller is only controlled by the pitch ratio. The rotation rate for engine and shaft become respectively $n_e = 750$ RPM, $n_p = 161$ RPM. At a ship velocity of $v_s = 11kts$, the advance ratio becomes $J = 0.421$.
- Configuration 2: there is a possibility to reduce the engine and shaft RPM to 90% of the nominal

RPM. The rotation rate for engine and shaft become respectively $n_e = 680$ RPM, $n_p = 145$rpm. At a ship velocity of $v_s = 11kts$, the advance ratio increases to $J = 0.469$. This reduces the delivered power to the propeller slightly, and further reduction of power can be realized by pitch control. The power for the PTO needs to be obtained by a separate generator set. However, the gen-set operates at a higher specific fuel consumption.

The required thrust from the propeller to overcome the ship's resistance, is found by finding equilibrium point between propeller thrust and the required thrust due to resistance. The operating point of the propeller at advance ratio J, is found by equalizing thrust coefficient K_T of ship and propeller according to equation 3.20.

$$K_{T,ship} = K_{T,prop} \tag{3.20}$$

From Klein Woud & Stapersma [18], the equation for $K_{T,ship}$ can be expressed as function of advance ratio J, see equation 2.2 and 2.3. The propeller mounted on the ship, is a controllable pitch propeller, comparable with the Wageningen B-series of type B4-40, with four blades and blade ratio $A_E/A_0 = 0.40$. However, the implementation of open water diagram of the CP-propeller is not considered, since the formulas of the Wageningen B-series were better assessable. However, the open water diagram of a CP-propeller for different pitch ratios, can have a lower open water efficiency and therefore it would be wise to replace the open water diagram of the Wageningen B-series with the open water diagram of the CP-propeller in an improved power prediction program.
In figure 3.4 and 3.5, the open water diagrams of the propeller of the Wageningen B-series are presented including the thrust coefficient of the ship with and without wind-assist, $K_{T,ship,1}$, $K_{T,ship,0}$ respectively for two configurations ($n_e = 750$ RPM and $n_e = 680$ RPM). For the case with wind propulsion, an example is shown with a resistance reduction of 30%, resulting in a lower thrust coefficient, $K_{T,ship,1}$. From the open water diagrams, it can be seen at what thrust coefficient, the ship and propeller match (for a certain pitch ratio) for a given advance ratio J. Then, the corresponding propeller efficiency, η_P, can be read out for the right pitch ratio P/D. The delivered power P_D is then calculated by propeller efficiency η_P and hull efficiency η_H, see equation 3.21.

$$P_D = \frac{P_E}{\eta_P \cdot \eta_H} \tag{3.21}$$

3.3.1 Comparison Ship with and without WASP

In the following, a comparison will be made for the propeller efficiency for a ship sailing with and without WASP at two operating advance ratios. This gives 4 cases, which are defined as:

- Case 1: Without wind-assist, at nominal engine speed, $n_e = 750$ RPM.
- Case 2: With wind-assist, at nominal engine speed, $n_e = 750$ RPM.
- Case 3: Without wind-assist, at reduced engine speed, $n_e = 680$ RPM.
- Case 4: With wind-assist, at reduced engine speed, $n_e = 680$ RPM.

In figure 3.4 and 3.5 the matching point for each case K_T between ship and propeller is denoted with the case number 1-4. The effect of reducing the shaft RPM by 10% is regarded by comparing case 1 and 3. As can be seen from figure 3.4 and 3.5, the propeller efficiency increases significantly from $\eta_{P,1} = 0.52$ at $J = 0.421$ to $\eta_{P,3} = 0.56$ at $J = 0.469$, which will result in a 4% lower brake power demand of the engine. However, the specific fuel consumption increases and the power supply of the PTO needs to be accounted by a generator set, which uses a larger specific fuel consumption. This is reviewed in the engine characteristics of section 3.4.

The difference between a ship with and without wind-assist, can be regarded by comparing case 1 and 2 in figure 3.4. The pitch P/D reduces from approximately 0.65 to 0.57, while the propeller efficiency decreases by 2% from $\eta_{P,1} = 0.54$ to $\eta_{P,2} = 0.52$. Thus, for a ship using wind propulsion at nominal engine speed, there is a penalty in propeller efficiency of 2%.

However, when the engine speed is reduced for a ship with wind assist (comparing case 2 and 4), the pitch ratio increases from $P/D = 0.57$ to $P/D = 0.7$ and the propeller efficiency improves to $\eta_{P,4} = 0.555$. This is a major increase in propeller efficiency of 3.5%, compared to case 2, just by reducing the engine speed by 10%. The differences between case 1-4 are summarized in table 3.3.

Table 3.3: Propeller efficiencies for case 1-4.

Case	**1**	**2**	**3**	**4**
J [-]	0.421	0.469	0.421	0.469
n_e [rpm]	750	680	750	680
η_P [-]	0.54	0.52	0.555	0.555

From the comparison of a ship with and without WASP in case 1-4, it can be seen that the propeller efficiency for a motor-sailing vessel is not effected negatively or positively by more than 3.5%.
Surprisingly, considering the open water diagram, there is a great potential to improve the propeller efficiency when the ship is using wind propulsion. This would be only possible if the gearbox transmission allows a lower shaft speed. Then, the advance ratio increases and when values for $K_{T,ship}(J)$ are low enough, this can lead to an operational profile with very high propeller efficiency of $\eta_P \approx 0.70$ or higher. This would for example be the case when the advance ratio can become $J = 0.8$ and ship and propeller match at $K_T = 0.1$ at a pitch ratio of $P/D = 1.0$.

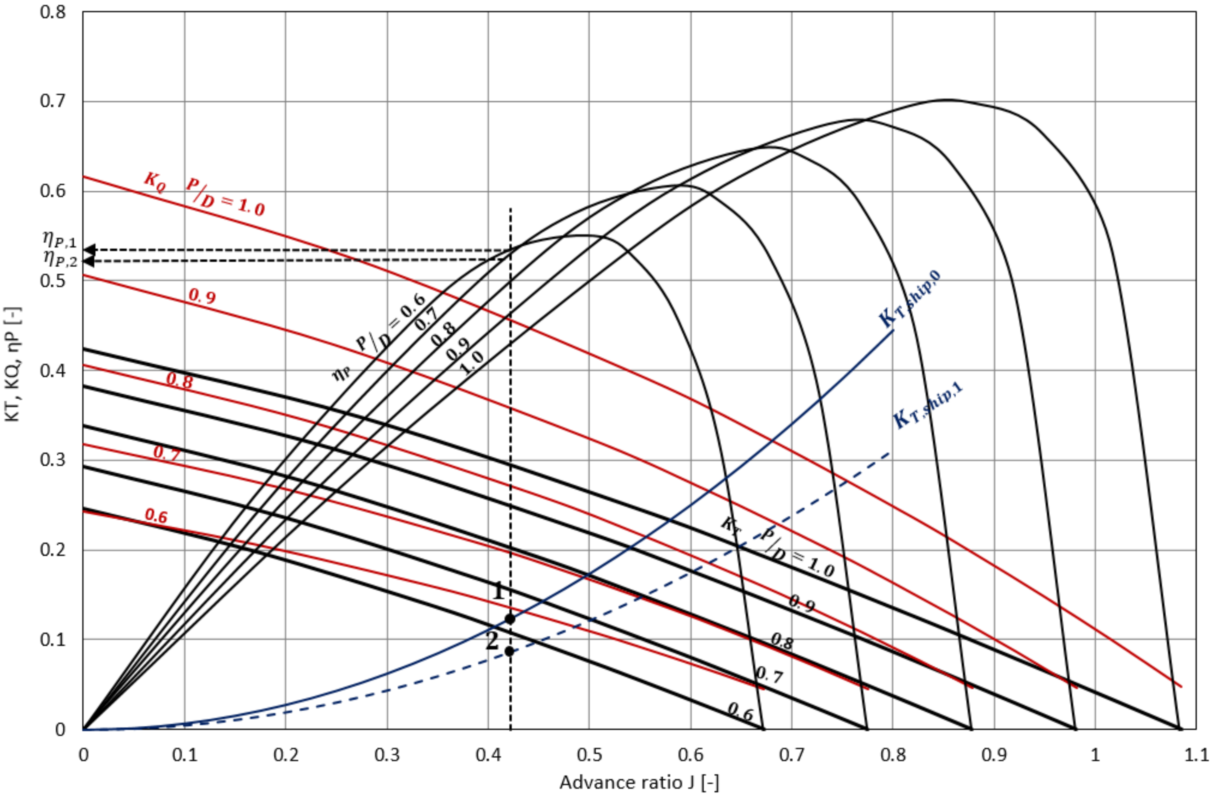

Figure 3.4: Open water diagram, operation point at $n_e = 750$ RPM ($J = 0.421$)

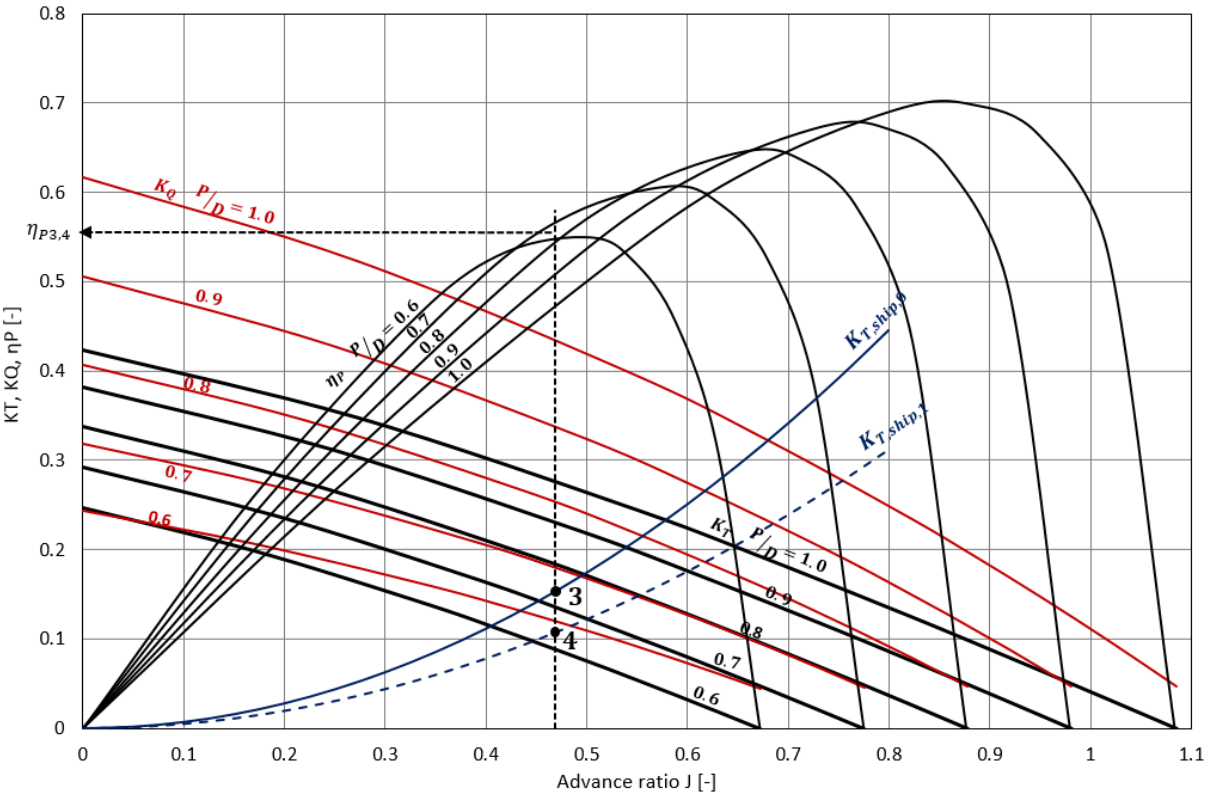

Figure 3.5: Open water diagram, operation point at $n_e = 680$ RPM ($J = 0.469$)

3.4 Engine Loading

As already mentioned in section 3.3, the ship is installed with a 2000kW four stroke diesel engine, with 6 cylinders of type 6M25C. In figure 3.6, the specific fuel oil consumption (SFOC) is presented as function of the brake power per cylinder for a constant nominal engine speed and for a fixed propeller by reducing the engine speed. The SFOC can be approximated by drawing a polynomial line through the points, according to equation 3.22.

$$SFOC = a_1 \cdot P_{B,cyl}^4 + a_2 \cdot P_{B,cyl}^3 + a_3 \cdot P_{B,cyl}^2 + a_4 \cdot P_{B,cyl} + P_{B,cyl} \tag{3.22}$$

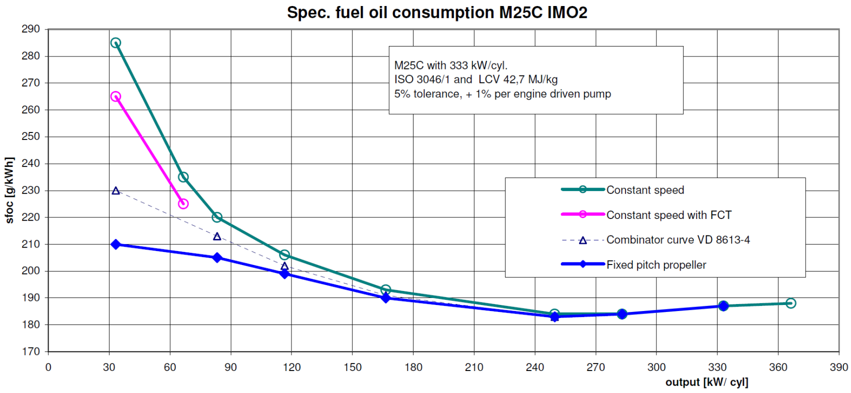

Figure 3.6: Specific Fuel Oil Consumption of the engine of type 6M25C.

Reducing the power of the engine effects the SFOC of the engine considerably. Moreover, there is a limit for the power reduction with a minimum power of 30% MCR. For wind speeds of 10 m/s and higher, and advantageous true wind angles around TWA ≈ 90°, the required power lowers even more than 30% MCR. Consequently, the ship speed needs to be increased. For a higher ship speed, the advance ratio J also raises, while $K_{T,ship}$ remains constant. As a result the propeller efficiency becomes higher.

In section 3.3 it is explained how the propeller efficiency can be derived. Furthermore, the assumption is made that gearbox efficiency η_{GB} and shaft efficiency η_S are constant. It should be investigated if the gearbox and shaft efficiency remain constant for other engine loads. The gearbox and shaft efficiency are assumed to be $\eta_{GB} = 0.99$ and $\eta_S = 0.99$ which is based on guidelines from Kleinwoud & Stapersma [39]. The brake power is then calculated in equation 3.23 by the delivered power P_D from equation 3.21. The brake power can also be depicted in a polar plot and can be regarded as a Power Prediction Program or PPP.

$$P_B = \frac{P_D}{\eta_{GB} \cdot \eta_S} \tag{3.23}$$

However, the electrical power for the aspiration of the Turbosail fan is not included in the brake power of the engine. This topic will be addressed in chapter 8 for the modified FPP after a better understanding of the Turbosail by a numerical study. The polar plot for net resistance presented in figure 3.3, can now be transferred to a Fuel Prediction Program (FPP), where the fuel consumption per hour can be calculated for all 360 degrees TWA, by equation 3.24.

$$FC = P_B \cdot SFOC \tag{3.24}$$

In figure B.1 and B.2 of appendix B, the fuel consumption FC and net resistance R_1 are presented in non-dimensional form in a polar diagram for a ship speed of $v_s = 11.5$ kts for wind speeds of up to 10 m/s and for two engine speeds. The fuel consumption is made nondimensionsal by dividing the fuel consumption by the maximum fuel consumption in the conventional mode without wind-assist FC_1/FC_0. The net resistance is nondimensionalized by dividing by the total resistance without wind-assist, R_1/R_0. These same results are also depicted in table B.1 - B.2 for a TWA of 90 degrees including the propulsive efficiency η_D and SFOC.
Considering table B.1 where the engine speed is set at 750 RPM, the net resistance for a TWA of 90 degrees and a wind speed of 10 m/s becomes $R_1 = 0.67 \cdot R_0$, but leads relatively to a higher fuel consumption of $FC_1 = 0.73 \cdot FC_0$, where subscript 0 refers to the conventional mode and subscript 1 refers to the wind-assisted mode at TWA = 90°.
When the engine speed is reduced to 680 RPM, the fuel consumption is slightly lower which is due to a better propeller efficiency, see table B.2.

For higher wind speeds, the ship speed needs to be increased to prevent the ship delivering less than 30% MCR. In figure B.3 and B.4 another two FPPs are presented for a ship speed of $v_s = 12.5$ kts including the wind speed of 14 m/s. At $U_{TW} = 14$ m/s, a larger relative difference in fuel consumption is observed between engine speeds of 680 RPM and 750 RPM. This is caused by the large difference in propeller efficiency, $\eta_P = 0.596$ and $\eta_P = 0.557$ respectively.

When the ship is in service under the presence of additional thrust of Turbosails, the potential in fuel savings depends in a large extent on the ship speed, shaft rotation speed and the engine SFOC under low power. To improve the potential of wind assist, a CP propeller and a larger range of the shaft rotation speed will improve the propeller efficiency significantly up to $\eta_P = 0.7$. This can be realized for a high pitch ratio P/D, with a large advance ratio and low required thrust of the propeller. However, the engine configuration should be adapted to be more fuel efficient in lower power range. Therefore, other engine configuration such as diesel-electric would improve the fuel savings by wind-assistance.

3.5 Conclusion PPP

In this orientating stage of defining the important aspects of ships using wind propulsion as an auxiliary propulsion system, concluding remarks are drawn for the most uncertain and important aspects regarding the feasibility of wind propulsion for commercial ships.

Hydrodynamic Forces. Side forces of the Turbosail need to be balanced by the hydrodynamic side forces produced by the hull and appendices such as the rudder, skeg and bilge keel. The hydrodynamic lift and induced drag of the bare hull determine the magnitude of generated side forces, which are mainly dependent of ship hull parameters such as draft to length ratio, midship coefficient and the block coefficient. Two empirical formulations to estimate the hydrodynamic side force by Kornev are considered in a sensitivity study. It is observed, that when the hull of the ship generates less hydrodynamic side forces, for $F_{y2,H}$ is case 2, the rudder needs to produce the other side forces to balance the Turbosail

forces in sideway direction. Larger rudder forces accompanies with a larger rudder resistance. Empirical formulas proposed manoeuvring theory such as Kijima [10] and SNAME [13], seem to over predict the hydrodynamic side forces at small drift angles. Furthermore, the centre of lateral resistance of the bare hull, X_{CLR} is located in all times in front of the ship, which causes a large yawing moment. In order to balance the Turbosail forces it would be most ideal to position the wind conversion units as far in front of the ship, so that the required rudder forces are minimized. Eventually, it can be concluded that still a high uncertainty remains about the hydrodynamic side force and induced resistance due to leeway and should be further investigated in next studies.
To predict the benefit from Turbosails in relation to fuel savings, the importance of accurately predict the hydrodynamic lift and induced drag of the bare hull and appendages such as rudder, bilge keel (and skeg) are essential. It would be recommended to do extensive model testing or CFD computations. All empirical models do not account for scale effects, because the hydrodynamic derivatives are obtained by model test results. It is therefore desired to picture the influence of scale effects.

Rudder Forces. Depending on the selected method for estimating the side forces, the required rudder angle can become rather large, so that the rudder resistance even abrogates the advantage gained by Turbosails. The maximum rudder angle in relation to stall needs to be studied, so that a certain margin should be reserved in case a ship needs to manoeuvre quickly in dangerous situations. In the context of maximum rudder angle, it should also be recommended to include external forces due to current and waves.

Matching and Propeller Efficiency. When wind propulsion takes over a part of the total resistance, the delivered power to the propeller needs to be decreased. In case of a controllable pitch propeller, the pitch ratio P/D need to be reduced. The engine however, is not capable to reduce its engine speed by more than 10 %, so that the advance ratio J, cannot be increased to operate at a higher propeller efficiency. In current engine configuration, where the range of engine speed is restricted at 750 RPM, the propeller efficiency declines of approximately 2% when the net resistance is reduced by 35%.
When the engine speed can be reduced by using for example a diesel-electric engine configuration, the propeller efficiency improves considerably from $\eta_P = 0.52$ to $\eta_P = 0.70$. This will raise the benefit from wind-assisted propulsion even more. If the engine speed is reduced with 10% to 680 RPM, the propeller efficiency increases by 3.5% to $\eta_P = 0.555$. The power demand of a separate generator set is disregarded in this analysis and should be included to quantify what engine speed should be chosen to realize the largest fuel savings.

Engine Loading. When the engine loading decreases while the engine speed is constant, the SFOC becomes less optimal. In case of large additional thrust from Turbosails, the delivered thrust of the propeller is small, but leads to a less ideal SFOC. It is therefore recommended to increase the ship speed, so that the engine has a better operational profile. Furthermore, when the ship is sailing under low engine power, maintenance costs of the engine may increase due to pollution of the turbine nozzle ring, this aspect should be further investigated, but is out of the scope of this research.

Turbosail Forces. The Turbosail forces are an uncertain field and are investigated the refinement study with CFD in chapter 4-7. Also, the total external wind forces due to the superstructure and the interaction between Turbosail need to be calculated but are out of the scope of this research. Interaction effects between multiple Turbosails and the superstructure may effect the delivered forward thrust by the Turbosails and should be investigated in next studies.

Stability. In the feasibilty study [15], the stability is calculated for one loading condition at maximum draught. However, The stability for different loading conditions has not been examined yet and from safety perspective, this will be an important aspect to be known.

From the concluding remarks, it may be noticed that assessing the performance of wind propulsion, there are a large number of aspects to account for, which some of them, still need to be explored. From this definition study, it is concluded that the largest uncertainty are the hydrodynamic drift forces of the hull and rudder, and Turbosail forces including the effect of the superstructure. In the next phase of this thesis report, the focus lays on better predict the Turbosail forces. The main objectives are pointed out in chapter 4.

Chapter 4

Turbosail

4.1 Problem Description

The Turbosail profile investigated by Cousteau [1] was already introduced around 1980-1985. Although the outstanding lift and lift-drag ratios presented, this device has never leaded to a great breakthrough in wind-assisted propulsion. Perhaps, now in the time that the public awareness is growing to develop a more eco-friendly and sustainable economy, the re-introduction of the Turbosail could now be the right moment! In section 3.5, it is concluded that the Turbosail is one of the major uncertain factors in the FPP. As a continuation of this master thesis, the main objective is selected to numerically predict the lift and drag coefficients of the aspirated foil, by conducting CFD computations and interpreted the new lift and drag coefficient in a final polar plot of the FPP of the vessel of interest.

Regarding the report of Cousteau describing the Turbosail performance, there is confusion about the definition on how the lift and drag coefficients are defined. In the Turbosail patent report [16], the definition of surface area is subscribed as *'the surface area of the device as projected on a plane perpendicular to the direction V in which the fluid moves'*. This sentence implies that the surface area changes with the angle of attack, where the chord length shortens for higher angles of attack. By definition, the lift and drag coefficients are higher in equation 2.5 and 2.6. However, according to Bertrand Charrier (one of the authors of the Turbosail publication [1]), the normal convention is used of defining the surface of an airfoil, where the largest chord length is constantly used as a measure of defining the surface.

The aim is to obtain clarity about the lift and drag coefficients at three suction speeds, $C_q = [0; 0.032; 0.047]$ at free stream Reynolds number of $\mathrm{Re} = 6 \cdot 10^5$ (corresponding to an apparent wind speed of $U = 10m/s$ at model scale) for an infinite span (the Turbosail profile fixed between two frictionless walls), as was already stated in research question 2 in section 1.4.

Additionally, a finite Turbosail at model scale is modelled with a finite aspect ratio of $A_R = 5.5$ at an optimal angle of attack to be implemented in the Power Prediction Program, stated in research question 3. The choice of this aspect ratio, is based on the dimensions of the wind conversion unit. Moreover, a Turbosail at model scale 1:2 is conducted during the time span of the research project, so that a good comparison can be made between CFD results and measured forces from the physical Turbosail model. At last, it can be concluded whether the reported lift-drag coefficients of Cousteau for finite and infinite span are realistic values or not.

In order to scale correctly between model and full scale, Reynolds scale factors are calculated and explained. The expected forces are calculated and explained in section 8.1.

4.1.1 Desirable Working Points

From figure 2.6, two interesting operating suction coefficients appear. At first, the highest suction coefficient with $C_q = 0.047$ where the maximum reported lift force is obtained and second a suction speed at $C_q = 0.032$ which gives a better lift/drag ratio while using less aspiration power. From figure 2.6, it remains not entirely clear from Cousteau [1] what is the actual Reynolds number and the selected profile. However, the impression is that the Reynolds number is $Re = 130.000$ and that the selected profile is referred to the half-elliptic cross section of the Moulin au Vent (MAV).

The current Turbosail model of scale 1:2, does not consist of experimental test results yet. A comparison with CFD results is therefore not possible. Although this profile has a slightly different geometry compared to the half-eliptic profile of the Moulin au Vent which is considered in the numerical study, it is relevant to select ambient wind condition which can easily be measured. A wind velocity of 10 m/s corresponds to wind force of 5 Beaufort and generates significant forces that can be measured within acceptable accuracy. This wind velocity corresponds to a Reynolds number of $6 \cdot 10^5$, thus at full scale the Reynolds number is a factor 2 higher.
From fluid mechanics, the region of Reynolds number between $10^4 - 10^6$ is generally characterized as a transition zone between a laminar to turbulent flow stream in the boundary layer. This can affect the direction of streamlines, affecting the lift and drag forces. Therefore, to capture the influence of this phenomena, transition equations have also been solved, which is further explained in section 4.4.2.

The lift and drag coefficients reported by Cousteau might have been defined by dividing the lift force by a smaller surface, with a different definition of the chord length than is usual in defining lifting profiles. By this definition, one gets the impression that the aspirated foil has superior lift and drag coefficients. To resolve this uncertainty on the generated forces, the aim is to verify if these coefficients are valid by performing a numerical study by CFD using ReFRESCO. In this numerical study, the influence of three turbulence models are investigated to evaluate their differences which find their origin as modelling errors. The selected turbulence models are described in section 4.4.

4.2 Theoretical Background Fluid Dynamcis

In fluid dynamics, a numerical prediction of the flow around an object is conducted by a domain filled with a finite number of cells or control volumes (CVs). A domain filled with cells is also called a grid, which is treated in section 5.2 for the Turbosail profile. For each CV, the well-known Navier Stokes equations are solved, which are generally stated as the combined equation for momentum conservation and continuity equation for mass conservation. Many books on fluid dynamics treat these equations, such as by Larsson & Raven [20] or Feriziger [21]. In section 4.2.1, a brief review of the basic steps in the Navier Stokes equations are given.

4.2.1 Navier Stokes Equations

Considering a CV in figure 4.1, with a length dx, dy, dz and velocity components du, dv, dw in x,y and z direction respectively, the continuity equation can be derived. For this fluid particle, the mass flow entering the domain, must be equal to mass outflow of the domain. This yields to equation 4.1.

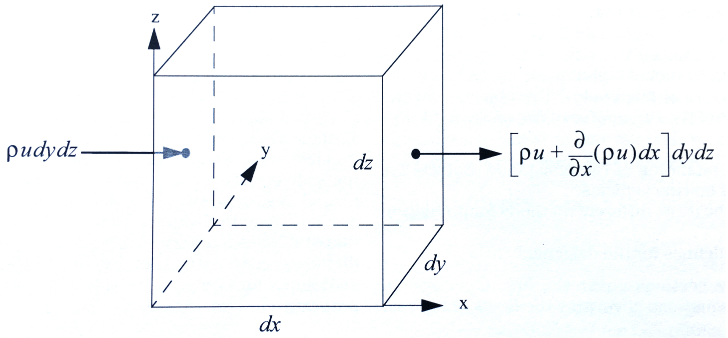

Figure 4.1: Mass flow through fluid element or control volume, by Larson & Raven [20]

$$\frac{\partial}{\partial x}\rho u dxdydz + \frac{\partial}{\partial y}\rho v dxdydz + \frac{\partial}{\partial z}\rho w dxdydz = 0 \tag{4.1}$$

Then, for an incompressible flow where the density ρ is constant, equation 4.1 can be written as,

$$\frac{\partial u}{\partial x} + \frac{\partial v}{\partial y} + \frac{\partial w}{\partial z} = 0 \tag{4.2}$$

In vector notation in equation 4.3, this is written as the divergence of velocity vector **u** is equal to zero, where **u** = u,v,w.

$$\nabla \cdot \mathbf{u} = 0 \tag{4.3}$$

Here, the divergence of a vector, denoted with $\nabla\cdot$ stands for the operator $\left[\frac{\partial}{\partial x}, \frac{\partial}{\partial y}, \frac{\partial}{\partial z},\right]$

The Einstein summation convention can be used to write this equation in an compact form,

$$\frac{du_i}{dx_i} = 0 \tag{4.4}$$

where subscipt i = 1,2,3 is used to declare $u_1 = u$, $u_2 = v$, $u_3 = w$. For every i, a summation with the previous terms are conducted. The introductory of the Einstein convention comes in play to write the Navier Stokes equations in a more compact form.

In addition to the continuity equation, equations for force equilibrium or momentum can be set up. The relevant forces that need to be modelled are the pressure force, dF_p and viscous forces dF_ν, where body forces originating from gravity are not modelled. For a the fluid element of figure 4.1, the force equilibrium can be translated to equation 4.5.

$$dm \cdot \mathbf{a} = dF_p + dF_\nu \tag{4.5}$$

From equation 4.5, the Navier Stokes equations for momentum conservation can be derived, which is written in Einstein notation in equation 4.6. The complete derivation can be found for example in Larsson & Raven [20]. The momentum equation assumes the fluid is incompressible and isothermal which means that the density and viscosity are constant and thus not dependent of temperature. In this way, the energy equation doesn't need to be included.

$$\frac{\partial u_i}{\partial t} + \frac{\partial}{\partial x_j}(u_j u_i) = -\frac{1}{\rho}\frac{\partial p}{\partial x_i} + \frac{1}{\rho}\frac{\partial \sigma_{ij}}{\partial x_j} \tag{4.6}$$

The stress tensor σ_{ij} in the viscous term of the momentum equation, is defined in equation 4.7.

$$\sigma_{ij} = \mu S_{ij} \tag{4.7}$$

where the rate of strain tensor S_{ij} is defined as,

$$S_{ij} = \left(\frac{\partial u_i}{\partial x_j} + \frac{\partial u_j}{\partial x_i}\right) \tag{4.8}$$

To quantify the pressure, a relation can be found using the Poisson equation. The Poisson equation is derived by taking the divergence (by using the continuity equation in equation 4.3) of the momentum equation so that mass conservation is preserved, see equation 4.9. For example, the derivation can be found at: $http://www.thevisualroom.com/poisson\_for\_pressure.html$

$$\frac{\partial}{\partial x_i}\left(\frac{\partial p}{\partial x_i}\right) = -\frac{\partial}{\partial x_i}\left[\frac{\partial \rho u_i u_j}{\partial x_j}\right] \tag{4.9}$$

A method to solve these equations directly without the introductory of additional equations, is known as direct numerical simulation (DNS) which requires very fine grid cells and very small time steps to solve the smallest turbulent length and times scales in the flow. These length and time scales are known as the Kolmogorov length and time scale. However, for flows with medium to high Reynolds number, the computational expense is out of range in industrial applications. Consequently, empirical methods have been developed to model turbulence, also known as turbulence models, which is explained in section 4.4.

Besides DNS, other solution techniques are used to reduce the computational cost of solving the Navier Stokes equation, such as resolving the larger and more anisotropic turbulent energy length scales known as subgrid scales (SGS) by a filtering process called Large Eddy Simulation (LES). The smallest and more isotropic turbulent length scales are modelled by turbulence models. Since LES and DNS are methods that resolve turbulence at different extent, these methods are also denoted as scale resolved simulations (SRS).

A second method is by averaging the Navier Stokes equations, or known as Reynolds Average Navier Stokes (RANS) equations, where the average flow is solved for stationary flows. Also unsteady behaviour can be captured by RANS, when a flow shows strong vortex shedding, known as unsteady RANS (URANS). The principle of the RANS equation are explained in section 4.3.

4.3 RANS equations

In statistically steady flows, where phenomena such as vortex shedding plays a less significant role, the variables in the Navier Stokes equation are subdivided in,

$$u_i(x,t) = \bar{u}_i(x) + u_i(x,t)' \qquad p(x,t) = \bar{p}(x) + p(x,t)' \qquad \sigma_{ij}(x,t) = \bar{\sigma}_{ij}(x) + \sigma'_{ij}(x,t) \tag{4.10}$$

where the upper bar presents the average value and the fluctuations are denoted by u', p' and σ'. Substituting the mean and fluctuating terms of equation 4.10 in the momentum equation of eq. 4.6, and average the whole equation, leads to the general formula for the Reynolds-averaging Navier-Stokes (RANS) equation, see equation 4.11.

$$\frac{\partial \bar{u}_i}{\partial t} + \frac{\partial}{\partial x_j}(\bar{u}_i \bar{u}_j) + \frac{\partial}{\partial x_j}(\overline{u'_i u'_j}) = -\frac{1}{\rho}\frac{\partial \bar{p}}{\partial x_i} + \frac{1}{\rho}\frac{\partial \bar{\sigma}_{ij}}{\partial x_j} \tag{4.11}$$

From this averaging process, an additive term appears from the convective term, R_{ij}, which is commonly combined with the viscous stress tensor σ_{ij}, so that the RANS equations get the final form in equation 4.12.

$$\frac{\partial \bar{u}_i}{\partial t} + \frac{\partial}{\partial x_j}(\bar{u}_i \bar{u}_j) = -\frac{1}{\rho}\frac{\partial \bar{p}}{\partial x_i} + \frac{1}{\rho}\frac{\partial}{\partial x_j}(\bar{\sigma}_{ij} + R_{ij}) \tag{4.12}$$

where,

$$R_{ij} = -\rho \overline{u'_i u'_j} \tag{4.13}$$

The fluctuation terms $\overline{u'_i u'_j}$ equation 4.12 have introduced six new unknowns, also known as Reynolds stresses which need to be modelled. Therefore turbulence models are introduced to model these stresses, which is explained in more detail in section 4.4.3. Another method for solving the Reynolds stresses, is by the Boussinesq assumption which relates the Reynolds stresses R_{ij} to the rate of strain tensor S_{ij} according to equation 4.14.

$$R_{ij} = \mu_t S_{ij} - \frac{2}{3}\rho k \delta_{ij} \tag{4.14}$$

with the Kronecker delta δ_{ij} to be defined as,

$$\delta_{ij} = \begin{cases} 1 \text{ for } i = j \\ 0 \text{ for } i \neq j \end{cases} \tag{4.15}$$

The Boussinesq assumption assumes that the turbulence kinetic energy is assumed to be isotropic, so that $\overline{(u')^2} = \overline{(v')^2} = \overline{(w')^2}$. In situations where the flow behaves more anisotropic, this assumption gives less accurate results and then it might be better to solve the Reynolds stress in Reynolds Stress Model, such as the EARSM turbulence model discussed in section 4.4.3.

For a stationary flow, where the flow has a constant velocity profile, except for small turbulence fluctuations, the flow field can be considered as constant over a infinite time. In this way, the local time derivative disappears due to time averaging, so that the RANS equation reduces to equation 4.16 for steady problems. By not discretizing (or solving) the fourth dimension time, the computation time is considerably reduced.

$$\frac{\partial}{\partial x_j}(\bar{u}_i\bar{u}_j) = -\frac{1}{\rho}\frac{\partial \bar{p}}{\partial x_i} + \frac{1}{\rho}\frac{\partial}{\partial x_j}(\bar{\sigma}_{ij} + R_{ij}) \tag{4.16}$$

For types of flows that show a largely unsteady character, such as bluff bodies which show vortex shedding behaviour, solving the mean flow by excluding the time-derivative term in equation 4.16, will sometimes not capture fluctuations in the solution. For unsteady RANS simulations, equation 4.12 needs to be solved, which includes the time-derivative term. This is done by computing an ensemble average over a small timestep Δt.
The timestep Δt can be estimated by the Courant Friedlich-Lewy number, that indicates if a particle can travel with a velocity u_i through a typical cell with size Δx_i within a selected time step Δt, see equation 4.17.

$$CFL = \frac{u_i \Delta t}{\Delta x} \tag{4.17}$$

For explicit time integration schemes, the CFL should be below 1, because this can give convergence problems affecting the numerical results. For an implicit time integration scheme, which is applied in the current solver ReFRESCO, the CFL number may become larger, but it is desired to keep CFL numbers below 10. Other criteria to choose the time step are bated the Strouhal number, which is a dimensionless parameter that relates the frequency of vortex shedding to freestream velocity, U_∞ and a characteristic length, L such as the airfoil thickness or the diameter of a cylinder, see equation 4.18.

$$St = \frac{fL}{U_\infty} \tag{4.18}$$

An estimate for the vortex shedding frequency of Turbosail foil can be made based on the Strouhal number of a cylinder, which is around 0.2 at a Reynolds number of $6 \cdot 10^5$.

4.4 Turbulence

Turbulence is a complex phenomena, where vortices (recirculation of a flow or eddies) are produced in the presence of objects or driven by temperature differences. When the pressure difference between fluid particles are large, without being damped due to viscosity, vortices are created. A flow becomes turbulent instead of laminar when the inertial forces are dominant over the viscous friction forces, thus for higher Reynolds number in the order of $Re > 10^4$. A laminar flow can be characterized as a smooth flow, where the streamlines are parallel to each other, while there is minimal mixing. In contrary to a laminar flow, a turbulent flow enhances mixing and is very dissimilar and chaotic.

In DNS the flow is resolved for the smallest turbulent structures, but with current computational resources, industrial use for medium to high Reynolds numbers is out of range. In order to analyse the flow, using less computational demanding techniques, the turbulence needs to be modelled. A principle called turbulence energy cascade, describes the energy transfer from large vortices with high kinetic energy to smaller vortices, where kinetic energy is finally transferred or dissipated into heat due to viscous friction. This principle is used to model the turbulence in additional equation(s) (zero-, one- and two-equation) for the kinetic energy, k and dissipation rate ω, where there are a variety of turbulence models to model different types of flow. Turbulent models are based on empirically obtained parameters, where one tries to identify which turbulent model is most appropriate for a particular problem. In this thesis, a verification study is conducted, where the influence of different turbulence modelling techniques are investigated and compared. The three selected turbulence models are the two equation $k - \omega\ SST$ of Menter 2003 [32], based on the Boussineq assumption, discussed in section 4.4.1. Secondly, the transition from laminar to turbulent flow in the boundary layer is modeled using the Local Correlation Transition Modeling (LCTM) model, which is indirectly coupled to the SST 2003 model of Menter, with two additional transition equation, explained in section 4.4.2. Thirdly, the Explicit Algebraic Reynolds Stress Model (EARSM) is selected which accounts for anisotropic behavior of turbulence with additional equations for the Reynolds stresses.

4.4.1 $k - \omega$ SST of Menter 2003

The $k - \omega$ *SST* turbulence model of Menter [32], is a very common turbulence model to be applied in industrial applications which is based on two transport equation for the turbulent kinetic energy k and specific dissipation rate ω. The turbulence kinetic energy k is specified in equation 4.19 from the instantaneous fluctuating velocity terms u_i' from equation 4.10.

$$k = \frac{1}{2}[\bar{u}'^2 + \bar{v}'^2 + \bar{w}'^2] \tag{4.19}$$

The two transport equation for k and ω are presented in equation 4.20 and 4.21.

$$\frac{\partial(\rho k)}{\partial t} + \frac{(\rho \bar{u}_i k)}{\partial x_i} = \tilde{P}_k - \beta^* \rho k \omega \frac{\partial}{\partial x_i}\left[(\mu + \sigma_k \mu_t)]\frac{\partial k}{\partial x_i}\right] \tag{4.20}$$

$$\frac{\partial(\rho \omega)}{\partial t} + \frac{\partial(\rho \bar{u}_i \omega)}{\partial x_i} = \alpha \rho S^2 - \beta \rho \omega^2 + \frac{\partial}{\partial x_i}\left[(\mu + \sigma_\omega \mu_t)\frac{\partial \omega}{\partial x_i}\right] + 2(1 - F_1)\rho \sigma_{w2}\,\frac{1}{\omega}\frac{\partial k}{\partial x_i}\frac{\partial \omega}{\partial x_i} \tag{4.21}$$

With blending function F_1 defined as,

$$F_1 = \tanh\left\{\left\{\ \min\left[\max\left(\frac{\sqrt{k}}{\beta^* \omega y}, \frac{500\nu}{y^2 \omega}\right), \frac{4\rho \sigma_{\omega 2} k}{CD_{k\omega} y^2}\right]\right\}^4\right\} \tag{4.22}$$

where $CD_{k\omega}$ is,

$$CD_{k\omega} = \max\left(2\rho \sigma_{\omega 2}\frac{1}{\omega}\frac{\partial k}{\partial x_i}\frac{\partial \omega}{\partial x_i}, 10^{-10}\right) \tag{4.23}$$

The relation between turbulent kinetic energy k and ω is based on the Boussinesq assumption, which follow from the turbulent kinetic eddy viscocity, ν_t in equation 4.24.

$$\nu_t = \frac{a_1 k}{\max(a_1 \omega, S, F_2)} \tag{4.24}$$

$$F_2 = \tanh\left[\left[\max\left(\frac{\sqrt{k}}{\beta^* \omega y}, \frac{500\nu}{y^2 \omega}\right)\right]^2\right] \tag{4.25}$$

$$P_k = \mu_t \frac{\partial \bar{u}_i}{\partial x_j}\left(\frac{\partial \bar{u}_i}{\partial x_j} + \frac{\partial \bar{u}_j}{\partial x_i}\right) \qquad \rightarrow \tilde{P}_k = \min(P_k, 10 \cdot \beta^* \rho k \omega) \tag{4.26}$$

With blending functions:

$$\alpha = \alpha_1 F + \alpha_2(1 - F) \tag{4.27}$$

Similar equation holds for β and σ. $\beta^* = 0.09$, $\alpha_1 = 5/9$, $\beta_l = 3/40$, $\sigma_{kl} = 0.85$, $\sigma_{\omega l} = 0.5$, $\alpha_2 = 0.44$, $\beta_2 = 0.0828$, $\sigma_{k2} = 1$, $\sigma_{\omega 2} = 0.856$

4.4.2 Local Correlation Transition Modeling

In problem description of section 4.1, it is described that all test cases are analysed for a Reynolds number of $6 \cdot 10^5$. Boundary layer flows in the region of $10^4 - 10^6$ are familiar for their characteristic to transform from laminar to turbulent flow. The importance of transition modelling becomes relevant when there is a large influence of laminar to turbulent flow transition. The type of boundary layer flow, 'laminar' or 'turbulent' affects the boundary layer thickness, the skin friction and the streamline curvature around the foil and in the shear layer, which can eventually result in significant influence on the generated lift and drag coefficients. For a flat plate, the boundary layer thickness δ, as function of Reynolds number is given in figure 4.2.

It is known for many turbulence models, such as the SST model of Menter [32], that these models are not able to accurately capture the transition region at correct Reynolds number. In order to better capture

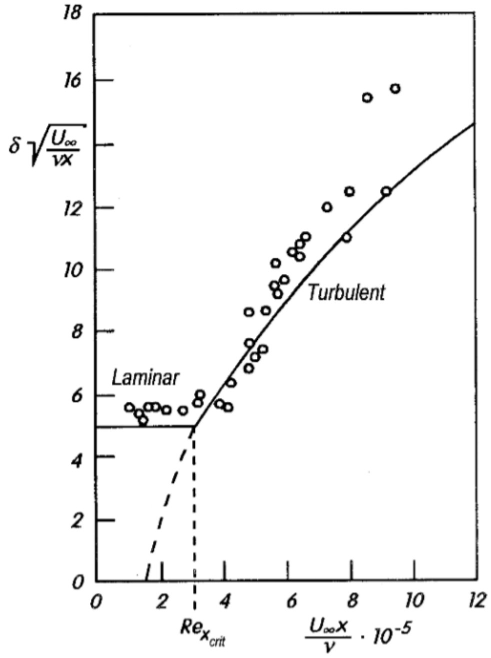

Figure 4.2: Boundary layer thickness δ, as function of Reynolds number for a flat plate at zero incidence, according to Schlichting & Gersten [28]

the transition zone, Langtry et al [30] have developed a method to model this transition behaviour with two additional transition equations, derived from the momentum equations, also known as the Local Correlation Transition Modeling (LCTM) model. In ReFRESCO, the LCTM model of Langtry is adopted. A complete description of the LCTM transition model is out of scope of this thesis, however a brief description of the governing equations is given in this section. The two additional transition equations for the intermittency γ and the local transition momentum thickness Reynolds number, $Re_{\theta t}$ are given in equation 4.28 and 4.29.

$$\frac{\partial(\rho\gamma)}{\partial t} + \frac{\partial}{\partial x_j}(\rho \bar{u}_j \gamma) = P_\gamma - E_\gamma + \frac{\partial}{\partial x_j}\left[\left(\mu + \frac{\mu_t}{\sigma_f}\right)\frac{\partial \gamma}{\partial x_j}\right] \tag{4.28}$$

$$\frac{\partial(\rho \tilde{R}e_{\theta t})}{\partial t} + \frac{\partial}{\partial x_j}(\rho \bar{u}_j \tilde{R}e_{\theta t}) = P_{\theta t} + \frac{\partial}{\partial x_j}\left[\sigma_{\theta t}(\mu + \mu_t)\frac{\partial \tilde{R}e_{\theta t}}{\partial x_j}\right] \tag{4.29}$$

The $k - \omega$ SST model described in section 4.4.1 is coupled to the additional momentum equations for γ and θ with the effective gamma, γ_{eff} in equation 4.30 which follows from equation 4.20.

$$\frac{\partial(\rho k)}{\partial t} + \frac{(\rho \bar{u}_j k)}{\partial x_j} = \tilde{P}_k - \tilde{D}_k + \frac{\partial}{\partial x_j}\left[(\mu + \sigma_k \mu_t)]\frac{\partial k}{\partial x_j}\right] \tag{4.30}$$

Where,

$$\tilde{P}_k = \gamma_{eff} P_k, \qquad \tilde{D}_k = \min(\max(\gamma_{eff}, 0.1), 1.0) D_k \tag{4.31}$$

From a recent study by Eça et al [31] on the influence of transition modeling using the LCTM model, it appears that the inlet quantities, such as turbulence intensity I and the eddy viscosity μ_t, are important parameters that influence the transition point in the boundary layer. The turbulence intensity is a measure for the turbulent kinetic energy, k, which is related to the free stream velocity U_∞ in equation 4.32.

$$k = \frac{3}{2}(U_\infty \cdot I)^2 \tag{4.32}$$

Therefore, in order to choice the correct inlet parameters, experiments are often essential to determine these right quantities. However, also without having knowledge about the right quantities to be implemented, it is interesting to see if the transition equations have a large influence on the lift and drag coefficients. It appears that for the higher I and eddy viscosity u_t, the larger is the region with turbulent boundary layer. Therefore, the choice is made to use a particularly small turbulence intensity I and eddy viscosity u_t, to have the highest potential to see a laminar boundary layer flow region compared to the original $k-\omega$ SST model. In section 6.3, a comparison between the standard SST and SST + LCTM model is made to see differences in the boundary layer and produced lift and drag coefficients.

4.4.3 EARSM

In ReFRESCO, the implemented EARSM model (Explicit Algebraic Reynolds-Stresses Model) refers to EARSM TNT model, described by Don et al [42]. This EARSM TNT model is based on the Turbulent Non-turbulent (TNT) $k{-}\omega$ model of Kok [41] which is modified by replacing the Boussinesq eddy-viscosity approximation by a more general turbulence closure hypothesis proposed by Wallin and Johansson [43]. The main concept of the EARSM model is that an anisotropic stress tensor a_{ij} is introduced in the term for eddy viscosity in equation 4.33 and 4.35 to model the Reynolds stresses τ in the transport equations for k and ω.

$$\nu_t = C_\mu k \tau \tag{4.33}$$

where τ becomes,

$$\tau^{-1} = \beta^* \omega \tag{4.34}$$

and

$$\frac{\tau_{ij}}{\rho} = 2\nu_t S - \frac{2}{3} k \delta_{ij} - a_{ij}^{ex} k \tag{4.35}$$

Chapter 5

Numerical set up

5.1 Testcases

When performing CFD computations, one is always interested in the credibility of the results. In order to qualify and quantify if the outcome of the numerical simulation are reliable, a scientist can perform a verification study where the result of different models may eventually be compared with experimental results, if available. This is also known as a verification & validation procedure of the numerical model. Although there are some experimental results of the Turbosail available from Cousteau [1], a clear description of the test condition are lacking, which makes it hard, or somewhat impossible to make a justified validation of the numerical model. However, if the CFD computations show a similar pattern, or promising results, this can motivate to construct a real model to do experiments in order to validate the CFD results. As a final goal, CFD can serve as a optimization tool, to investigate different profiles which lead to an optimum wing profile for a particular operational profile. This operation can be the highest C_L/C_D ratio at the lowest aspirational power, which is a favourable characteristic for head to beam wind headings of the ship relative to the wind. Another strategy can be to maximize the lift, at cost of some additional drag. In this section, the test set up of the conducted simulations are described which give an overview of the verification study.

5.1.1 2D Testcases

As an initial start, a 2D dimensional flow is analysed using SST as turbulence model for steady (SRANS) and unsteady RANS (URANS) computations for testcase 1.1-1.5., reviewed in chapter 6. In section 6.1, the sensitivity of the domain size is analysed in testcase 1.1 where in section 6.2, a grid dependency study is carried out to estimate the discretization error in testcase 1.2. In testcase 1.3, the effect of additional transition equations are solved to observe if transition from laminar to turbulent flow in the boundary layer plays an important role, see section 6.3. Subsequently, in testcase 1.4 for a particular grid, the lift and drag forces are calculated for a range of angle of attack are to obtain the familiar Cl, Cd - curves which can be compared to presented experimental values from Cousteau [1], presented in section 6.4. After the static analysis, transient (or unsteady) 2D computation are performed. A complete grid dependency study for URANS, varying the grid size and time step independently has not been carried out, although the time step size has been varied for one particular grid in testcase 1.5, see section 6.5. It can be seen from these testcases that there has been chosen to use a more pragmatic approach to investigate the discretization error for unsteady computations. In section 6.6, a range of angle of attacks are calculated in transient mode for two suction rates in testcase 1.6. Additionally, to see the Turbosail characteristics without aspiration applied, testcase 1.7 performs an unsteady RANS SST computation. The motivation for URANS is that it is expected that vortex shedding plays a more dominant role, so that URANS is better able to capture this behavior. An overview of all 2D testcases and presented in table 5.1, where Appendix C, shows all computations results for each testcase.

Despite the fact that the flow has not been solved in a third (z) direction (so turbulence is forced to be 2-dimensional and thus not physical), a first indication of the characteristics of the Turbosail can be observed. The 2D calculation also have the advantage to test the convergence behaviour at less computational expenses compared to 3D computations.

Table 5.1: Overview 2D Testcases

2D Testcases	Turbulence model	Description
1.1	SRANS SST	Domain size variation
1.2	SRANS SST	Grid dependency study
1.3	SRANS SST + LCTM	Transition modeling
1.4	SRANS SST	Range of α
1.5	URANS SST	Influence time step Δt
1.6	URANS SST	Range of α
1.7	URANS SST	Range of α, without aspiration

5.1.2 3D Testcases

The next step is to add more cell in z-direction to perform a 3D steady RANS computation with the SST model without LCTM, for a more physical modelling of turbulence. Again, a pragmatic approach is applied in order to evaluate the magnitude of the discretization error. At first, two grids of different spanwise lengths (z-direction) are analysed in testcase 2.1 for a steady state condition. Hence, it is known that the size in spanwise direction may effect the solution due to the boundary conditions, for example found by [22]. Then, for one grid in the 2D plane of table 5.4, grid nr 4, the number of cells in z-direction extended for three grid spacings, Δz, $\Delta z/2$ and $\Delta z/4$. Subsequently based on the grid refinement study in spanwise direction, one grid size is selected to calculated the lift and drag coefficients for a range of angle of attacks, α in testcase 2.2. In testcase 2.3, one angle of attack is analysed using the EARSM model to compare differences between turbulence models in the verification study. After investigating the influence of different turbulence models and modeling strategies such as 2D and 3D flows, a final 3D model with finite aspect ratio of $A_R = 5.5$ is analyzed in testcase 2.4. This model is a representation of the real model (although the profile is not 100% identical). This model requires an different grid, which is in detail described in section 5.3.1. An overview of the 3D simulations are given in table 5.2.

Table 5.2: Overview 3D Testcases

3D Testcases	Turbulence model	Description
2.1	SRANS SST	Domain size variation in spanwize z- direction
2.2	SRANS SST	Range of incoming angles, α
2.3	SRANS EARSM	Investigating anisotropic turbulence with EARSM
2.4	SRANS SST	Finite aspect ratio ofA_R=5.5

5.2 Grid Assembly

In this section, the method to generate of grid (or mesh) is discussed, where in section 4.2 already a small introductory of the definition of a grid is given.

For complex geometries with additional structure details, it is sometimes too difficult or impossible to generate hexathedral cells or structured grids since the quality of the grid becomes very poor. Then, unstructured grid can resolve this problem, since it can be built around more complex geometries. However, the accuracy of structured cells is much higher than unstructured cells and therefore the preference goes to construct structured grids, if possible. To make structured and high quality orthogonal grids, the choice for mesh program Pointwise is made, which is a grid generator for structured (and unstructured) grids. The main advantage of Pointwise over other grid generators is that the program has a function to extrude a grid from the Turbosail contours in normal direction outwards or inwards to create the complete domain, see figure 5.4. As a result, the first grid cell adjacent to the wall are perfectly orthogonal, which is the most accurate way to solve the boundary layer. Smoothing parameters are used to compute every next cell from extrusion adjacent to the current grid, which is a hyperbolic function. In this way, a very smooth and high quality grid is generated for the entire domain.

The quality of a grid can be characterized by several quantities, such as the minimum and maximum angle between two adjacent cells, the aspect ratio of one single cell, thus length over height ratio of a cell, orthogonality, (denoted by smoothness), area ratio, skewness and more. Except in the region of the boundary layer, high aspect ratio cells should be minimized, especially when unsteady computations are conducted, which require low CFL numbers.

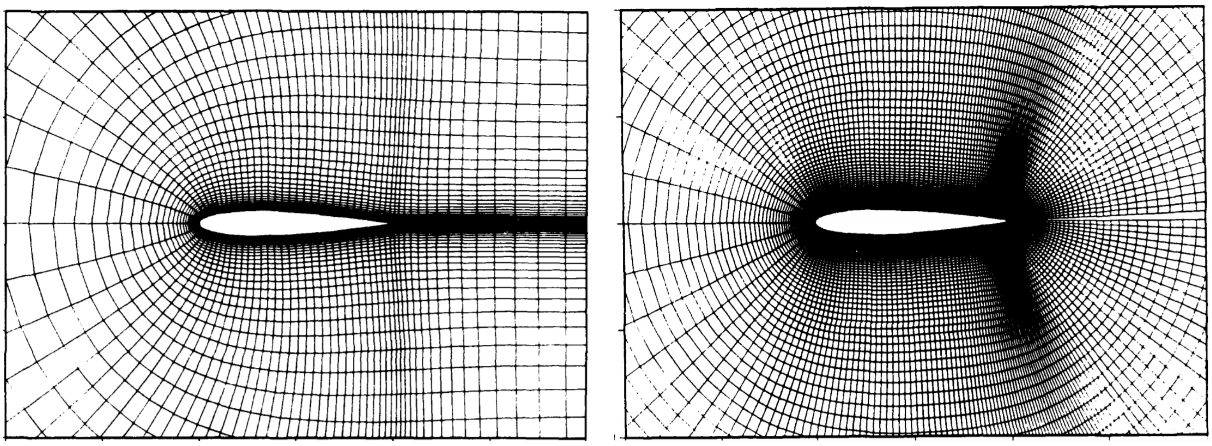

(a) C-grid (b) O-grid

Figure 5.1: Example of two grid types, from Lutton [25].

Most common structured grids for cylinders are of H-type or O-type, while for airfoils, additionally C-type of grids appear to be popular for a numerical model. Figure 5.1 shows two examples of C- and O-grid topologies as a mesh strategy. For the type of geometry of a Turbosail, a C-grid is not favourable because it is more difficult to generate the grid and leads to lower quality of cells, which is therefore not further considered as a possible method. For calculating the high lift coefficients of foils, an O-grid is more favourable than H-type, since the boundary condition (BC) at the far field affect the solution. The influence of the domain size on the solution is investigated in section 6.1.

The following steps are taken to conduct the grid, which are explained in sections 5.2.1 - 5.2.3.

- Quantify air properties.
- Predict wall spacing in the boundary layer by dimensionless wall spacing, y^+.
- Generate the grid from normal extrusion
- Check the quality

5.2.1 Air Properties

The material properties considered are assumed for air with a temperature of 15 C° at atmospheric pressure $p_{atm} = 1013.25 hPa$. It is most likely that ships equipped with mechanical sails will have the largest benefit from the wind in regions such as the North Atlantic, North sea, etc.. where the wind speed is annually above the global average. Therefore, the air temperature of $15 C^\circ$ is a good assumption. In table 5.3 the properties of air of given. It must be noted that only the dynamic viscosity and density are the variables of importance, since the energy equation (that gives a relation between pressure, density and temperature) is not solved for an incompressible isothermal flow.

Table 5.3: Air properties implemented in ReFRESCO

Properties	**Symbol**	**Value**	**Units**
Atmospheric pressure	p_{atm}	1013.25	hPa
Temperature	T	15	C°
Density	ρ_{air}	1.2257	kg/m^3
Kinematic viscoscity	ν	0.000014657	m^2/s
Dynamic viscosity	μ	1.797E-05	$kg \cdot m^{-1} s^{-1}$

The Reynolds number Re, is a dimensionless parameter relating the inertial forces and viscous forces in a flow, see equation 5.1.

$$Rn = \frac{\rho_{air} U_\infty L_C}{\mu} \tag{5.1}$$

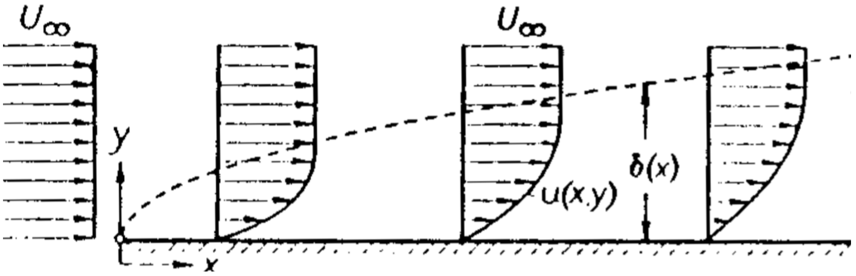

Figure 5.2: A schematic representation of a boundary layer and the boundary layer thickness $\delta(x)$, by Schlichting [29].

The Reynolds number can be used to identify the magnitude of turbulence and is important for the grid spacing in the boundary layer to capture the correct velocity field. This grid spacing is also referred to dimensionless wall spacing y^+, which is explained in section 5.2.2. Including the chord length L_C, freestream wind velocity U_∞ (which is identical in this case to the apparent wind velocity U_{AW}) the Reynolds number can be calculated using the air properties of table 5.3.

$$Re = \frac{\rho \cdot U_\infty \cdot L_C}{\mu} = \frac{1.2257 \cdot 10.0 \cdot 1.00}{1.797 \cdot 10^{-5}} = 6.8 \cdot 10^5. \tag{5.2}$$

5.2.2 Dimensionless wall spacing y$^+$

The boundary layer is a thin region of airflow adjacent to the wall surface of the Turbosail, also known as the boundary layer thickness δ, where the air velocity consist of a strong streamline curvature. At the wall surface, the air particles can be approximated to be zero, which is called a no slip condition while further away to the wall, the flow velocity develops until the freestream velocity is reached. The boundary layer thickness δ is characterized as the region where $\delta(x) = 0 - 0.99 \cdot U_\infty$. An example of this boundary layer is shown in figure 5.2.

All turbulence models are by definition based on empirically based parameters to approximate among others, the streamline curvature in the boundary layer. In the grid of the model, the cells adjacent (and preferably normal) to wall, cells require enough cells to calculate this streamline curvature. In this way, the flow streams in straight direction through the cell, parallel to the wall. In this way, cells are more efficient to resolve the flow. This principle is also true for cells further away from the wall, see figure 5.3.

Figure 5.3: Efficient cell topology, figure from [26]

The smallest cell requirement of the cells normal to the wall denoted with y, can generally be approximated by using the definition of dimensionless wall spacing y^+ in equation 5.3, which should be below 1, $y^+ < 1$. For example, Feriger & Peric [21] give some guidelines to predict the initial cell spacing, y_1 in the boundary layer.

$$y^+ = \frac{\rho u_\tau y_1}{\nu} \tag{5.3}$$

where u_τ is the shear velocity, given by equation 5.4

$$u_\tau = \frac{\sqrt{|\tau_w|}}{\rho} \tag{5.4}$$

Many formulations exist to calculate the shear stress τ_w, for example from the Schlichting correlation [29] in equation 5.5

$$C_f = [2log_{10}(Re) - 0.65]^{-2.3} \quad \text{for } Re < 10^9 \tag{5.5}$$

Consequently, the first cell normal to the wall, y_1, is calculated from equation 5.3- 5.5 and becomes $y_1 = 3.3 \cdot 10^-5$, which is an initial guess. However, from first calculations it was observed that at the leading edge region, there is a large increase in velocity so that the desired y^+ below one of was not met. Finally, to comply with $y^+ < 1$, the initial wall spacing is set to $y_1 = 2.0 \cdot 10^{-5}$.

In ReFRESCO, y^+ is computed from the $k - \omega\ SST$ turbulence model where the shear velocity u_τ, is calculated by using the von Karman constant κ equation 5.6, which is implemented in the momentum equations by equation 4.21 and 4.21.

$$k = \frac{u_\tau^2}{\sqrt{\beta^*}}, \qquad \omega = \frac{u_\tau}{\sqrt{\beta^* \kappa y_1}} \tag{5.6}$$

where $\kappa = 0.41$ and $\beta^* = 0.09$

5.2.3 Grid for 2D lift-drag coefficients

From the problem description in section 4.1, there are two main objectives to be fulfilled. First conduct a verification study to calculate lift-drag coefficients for a infinite span by modeling the Turbosail with only one cell in spanwise direction, which is thus a truly 2-dimensional flow. Additionally, the lift-drag coefficients are computed for infinite span by adding more cells in z-direction, to solve the Navier Stokes equations also for z-direction, which is more physical and realistic flow. The second objective is to calculate the lift and drag for a finite Turbosail wing with an aspect ratio of A_R=5.5, to see how wing vortex shedding affects lift and drag forces. In this section, the methodology is decribed on how to generate the grid for a infinite span calculations.
With the initial cell spacing, y_1, to be known from section 5.2.2, the grid can be extruded in normal direction outwards with a specified growth ratio, see figure 5.4a. The cell spacing in chordwise direction (along the Turbosail contours) is more concentrated at the leading edge due to the higher curvature of the profile, around the flap and at the circular aft region, which determines the cell density in the wake. By choosing smoothing parameters in Pointwise properly, a high quality grid is generated, which gives the final grid in figure 5.4b. The grid of the entire domain is shown in figure 5.5. The size of the domain is an important parameter in the way that the Turbosail 'feels' the boundaries and that has a direct effect on the lift and drag produced, which is set at a radius of $R = 100 \cdot L_C$, concluded from the domain sensitivity study in section 6.1.

The minimum and maximum included angle for a medium grid (grid 4) are 80° and 100° respectively, which show that the grid has a good orthogonality. For the grid refinement study of testcase 1.2, explained in section 6.2, a number of grids are produced from coarse (30.000 cells) to very fine (1 million cells) for a 2D grid, see table 5.4.

The script from Pointwise for grid refinements to produce geometrically similar grids, leaded to invalid grids. Therefore, the desired grid refinement is accomplished by manually increasing the number of points along the Turbosail profile and by specifying a smaller growth ratio. Each grid refinement increases the number of points in the xy-plane with a factor 2, so that the refinement factor in one dimension (x,y or z- direction) magnifies with a factor $\sqrt{2}$. An overview of all 6 grids is shown in table 5.4, presenting the main characteristics such as, initial cell size (first grid cell from normal extrusion), dimensionless wall spacing y^+ (defined in equation 5.3), growth ratio and number of cells of the total grid in the xy plane. x^* refers to the total points along the Turbosail profile and y^* are the number op points used for extruding the grid in normal direction to create the O-grid.

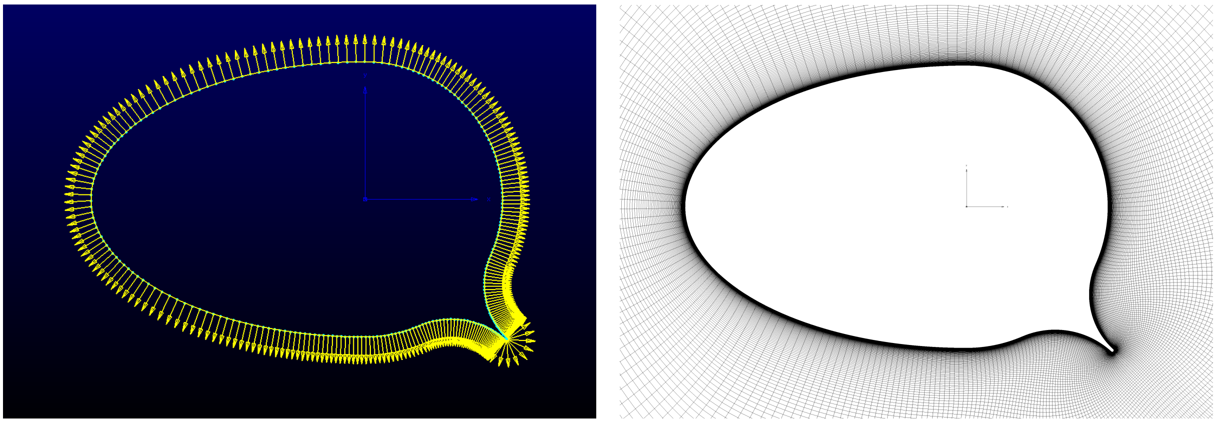

(a) Normal extrusion from Turbosail profile.

(b) Medium grid (grid 4) after extrusion

Figure 5.4: Method of grid generation

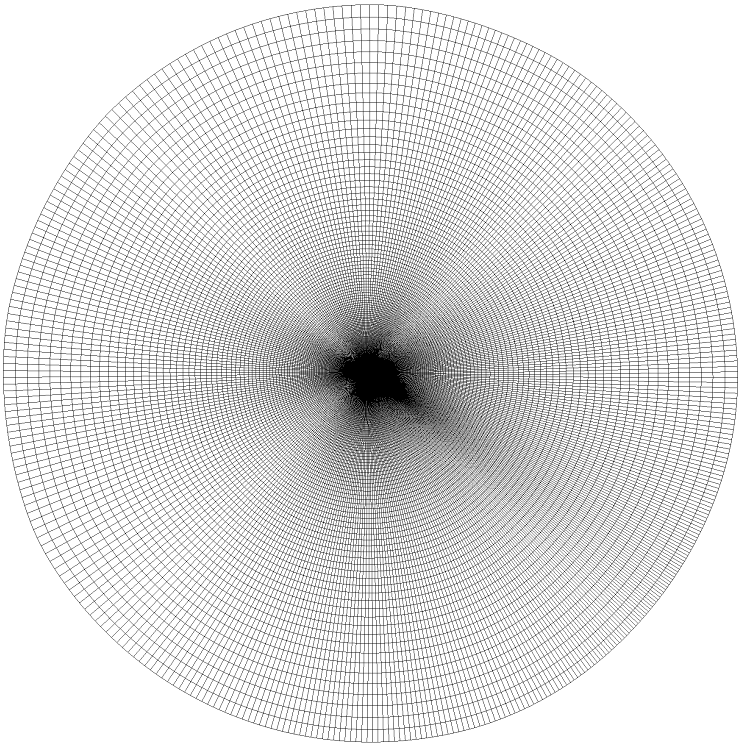

Figure 5.5: The complete domain size of an O-grid with a radius of $R = 100 \cdot L_C$

Table 5.4: Characteristics of 2D grids

Grid nr. i	x^*	y^*	**xy plane**	**growth ratio**	**initial** Δs	$max\ y^+$
1	1079	1020	1.100.580	1.012	5.00E-06	0.324
2	763	722	550.886	1.017	7.07E-06	0.421
3	539	510	274.890	1.025	1.00E-05	0.577
4	381	361	137.541	1.035	1.41E-05	0.804
5	269	255	68.595	1.050	2.00E-05	1.123
6	190	191	36.290	1.071	2.83E-05	1.520

5.3 Boundary Condition for Infinite Span

A definition of all planes in the domain and the corresponding 'family names' in ReFRESCO is depicted in figure 5.5. The boundary condition of each family name is subscribed in this section.

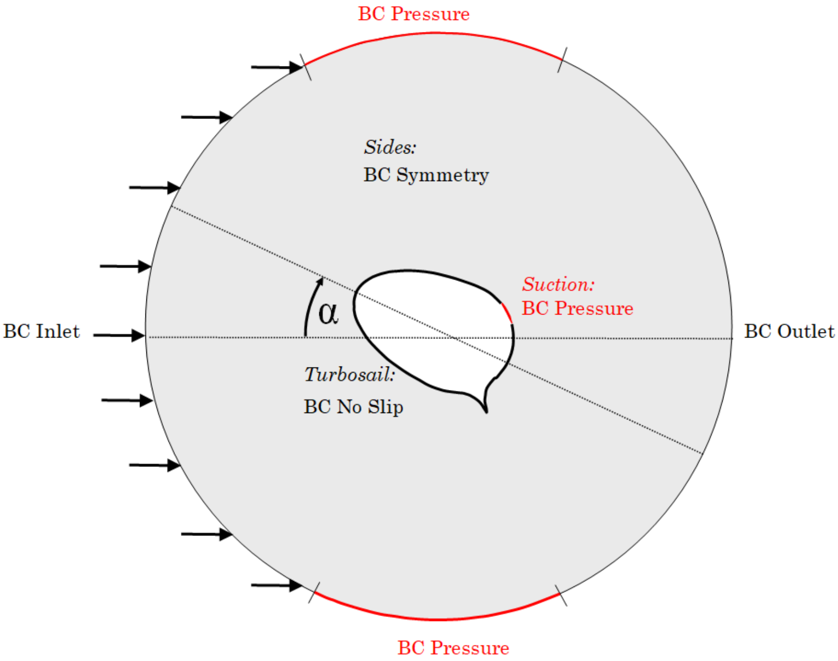

Figure 5.6: Schematic representation of boundary conditions. The family name *InletOutlet* has a autodetect BC function, which includes BC inlet, BC pressure and BC outlet.

InletOutlet. At the InletOutlet BC, which includes the inlet, outlet and a farfield, the autodetect boundary condition is applied. Autodetect is an option to be chosen in ReFRESCO for a boundary condition that detects the inlet, outlet and the farfield, based on the flow direction and the specified angles for auto detection. This function has the comfort not to change the axis rotation in the grid program POINTWISE, but by simply changing the inlet flow direction. At the inlet the freestream velocity is specified in x,y and z- direction including the static pressure p_{stat}. Furthermore the turbulence quantities are specified, such as eddy viscosity and turbulence intensity, which however, showed not significant influences by varying these parameters. At the Outlet, a static pressure, p_{stat} boundary condition is applied, which follows from equation 5.7 by Bernoulli. This equation that states that the total pressure is the sum of the static pressure p_{stat} and the dynamic pressure $\frac{1}{2}\rho_{air}U^2$, where the gravity term is negligible compared to the other terms and therefore excluded in the equation 5.7.

$$p_t = p_{stat} + \frac{1}{2}\rho_{air}U^2 \tag{5.7}$$

The relative pressure $p_{t,rel}$ is related to the atmospheric pressure, p_{atm}, according to equation 5.8. Other variables are determined from the interior domain.

$$p_{t,rel} = p_t - p_{atm} \tag{5.8}$$

At the farfield, the pressure boundary condition is applied, where the relative pressure is set to zero.
Turbosail. The surface that subscribes the Turbosail contours without the suction region is defined by the family name 'Turbosail' which consist of a 'no slip' boundary condition where the velocity at the surface is set to zero.
Suction. At the suction side, a pressure boundary condition applied, where a certain suction pressure, p_{suc} is set to obtain the desired dimensionless suction speed, C_q. The procedure on how to calculate the dimensionless suction speed is described in the following.
The mass flow through BC 'Suction', can be determined by extracting the velocity components in x,y,z direction of all cells in one xy-plane. For a 2D xy plane of only 1 cell thick in z-direction, the total mass flow through the 'Suction' boundary can exact be calculated by the one only xy-plane. When model

consist of a 3D model having multiple cells in the z-plane, then suction should ideally be calculated analysing all boundary data at the ’Suction’ BC. However, also an i number of xy-planes need to be introduced, to calculate the suction coefficients C_q at different span location and by taking the average of all C_q when equal spacing between the planes is used. This would only be necessary when a variance in suction velocity in x,y-direction at the aspiration region is observed. The massflow through the ‘Suction’ boundary, denoted with Q is calculated by the integral in equation 5.9.

$$Q = \sum_{i=1}^{N} z_{span,i} \int \mathbf{v}_{suc,i} \cdot \mathbf{n} \; ds \tag{5.9}$$

Where ds is the distance between each grid point along the ’Suction’ boundary, $\mathbf{n}$ is the normal vector of each grid cell projected inward and $\mathbf{v}_{suc,i}$ is the velocity vector in x,y,z for the grid cells in xy-plane at the suction location. This can also be visualized in figure 5.7. $z_{span,i}$ is the length in span direction over which the suction speed is calculated in the ensemble of xy-planes, so that the total span $z_{span,tot}$, becomes,

$$z_{span,tot} = \sum_{i=1}^{N} z_{span,i} \tag{5.10}$$

With the mass flow Q, to be known, the suction coefficient can easily be calculated by equation 5.11, that was already introduced in equation 2.7.

$$C_q = \frac{Q}{S \cdot U_\infty} \tag{5.11}$$

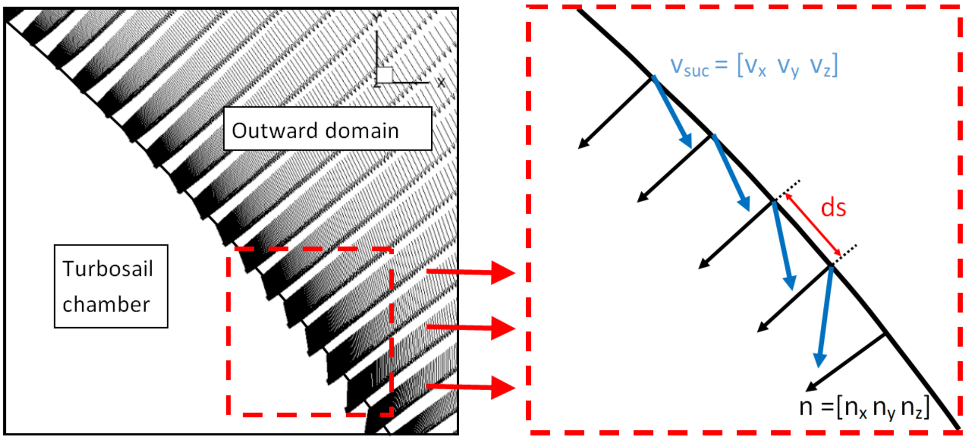

Figure 5.7: Left, velocity vectors adjacent to the suction boundary. Right, definitions for determination of mass flow through Suction boundary.

As an initial start, one can estimate the suction pressure based on the contour plot for pressure coefficient C_P along the Turbosail surface, given by Cousteau [1] for the situation with maximum lift. The dimensionless pressure is defined by dividing the total (relative) pressure with the dynamic pressure $\frac{1}{2}\rho_{air}U^2$ in equation 5.12.

$$C_P = \frac{p_{t,rel}}{\frac{1}{2}\rho U_\infty^2} \tag{5.12}$$

The C_P distribution from experiments is also compared with the numerical result in figure 6.2. At the aspiration region in figure 6.2, it can be seen that the pressure coefficient has a value of around $C_P \approx 4.5$. which is the dimensionless pressure, Finally, in equation 5.13 the initial guess for suction pressure p_{suc} can be estimated, rewriting equation 5.12. The desired suction pressure can finally be determined by a few iterations until the desirable suction coefficient is reached within 2-3%. If the initial pressure is chosen too small, this will result in a negative massflow directed outward such that suction becomes blowing.

$$p_{suc} = C_P \cdot \frac{1}{2}\rho_{air}U_\infty^2 = 4.5 \cdot \frac{1}{2} 1.225 \cdot 10^2 = 278 Pa \tag{5.13}$$

Sides. The boundary condition for the two side planes, are considered as frictionless walls which are subjected with a symmetry BC (Neumann BC). The derivatives of the quantities normal to this plane are set at zero.

5.3.1 3D Grid for Finite Span of A_R=5.5

The grid for the finite Turbosail with an aspect ratio of 5.5 requires a modified grid, by also making a grid inwards the Turbosail. For a half-eliptical, half cylindric body without a flap, generation of a structured grid would not be very complicated. However, to conduct a high quality structured grid including a flap is more difficult.

Due to the number of extra grid points inward the Turbosail, an the need for a larger domain above the top of the wing, it is chosen to select grid 5 from table 5.4 as a base grid to built the entire domain for the finite aspect ratio of 5.5. The methodology for making the inward grid is described in the following.

1. First extruding cells in normal direction inwards the profile, applying a growth ratio of about 1.15. Also, 25 extra points are added around the flap edge to have sufficient number cells to prevent bad quality of the cells, such as aspect ratio, minimum and maximum included angle, etc.
2. Subsequently, in the region around the flap, an assembled grid is generated from which again, the grid has been extruded inward from normal extrusion. This leads to a oval contour which can easily be built inwards.
3. A pole is introduced in the middle of the oval contour from which the entire domain is assembled.
4. At last, the pole is removed and by splitting the current grid in for edges, a final inward domain is conducted. Using the function 'solve' in POINTWISE, the quality of the grid is improved which gives the final grid shown in figure 5.8.

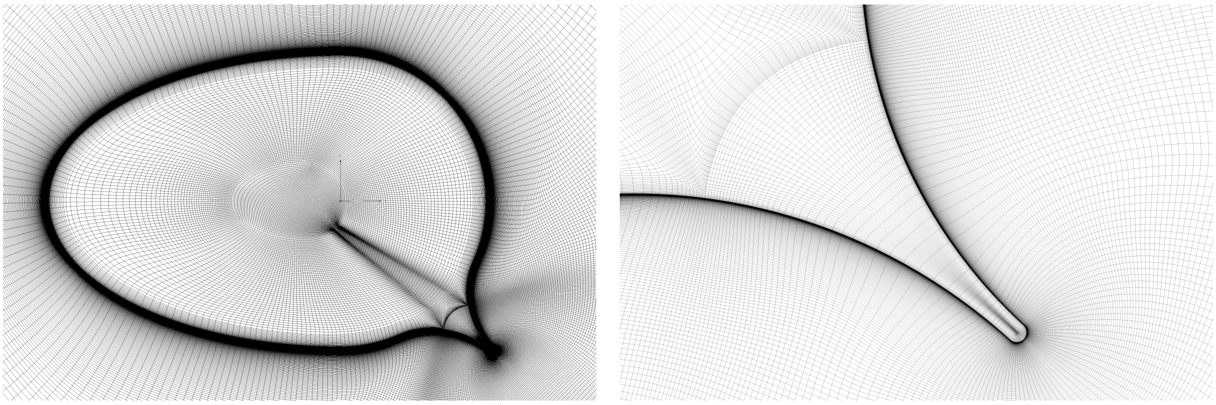
(a) Assembled grid inwards Turbosail (b) Grid topology around Flap region

Figure 5.8: xy-plane at top of Turbosail at z=5.5m

By having an inward grid in the xy-plane, the final grid in 3 dimensions can be constructed. At the top of the Turbosail, the grid spacing is dense to a level which complies with a $y^+ \approx 1$. From the bottom to the top, the outward xy-plane is extruded in a total of 150 points in z-direction. Above the top, the inner an outer domain are both extruded in z-direction with a total of 120 points. It was found from Jung et al [27] that a span height of 3 times the chord length, $3 \cdot L_C$, is sufficient to calculate the wing vortex shedding with enough accuracy. However, to have confidence that the domain boundaries do not affect the solution considerably, a larger span height of 10 metres is chosen to extent above the top of the Turbosail foil. The grid in the yz-plane including the boundary conditions can be observed in figure 5.9.

5.3.2 Boundary Conditions for finite aspect ratio A_R=5.5

The boundary conditions for the domain change for the plane at the top, which becomes a pressure boundary condition with a relative pressure of $p_{t,rel} = 0$, which is equal to the atmospheric pressure, p_{atm}. The bottom is still modelled as a frictionless wall, where a slipwall BC condition is applied.

However, in the real case, this would be a no slip wall, so that the produced lift at the bottom will decline. To model the wall, an extra boundary layer must be modelled which increases the number of cells even further, which goes for this thesis beyond computational resources. At the boundaries with family names *InletOutlet*, *Turbosail* and *Suction*, the boundary condition remain unchanged, see section 5.3.

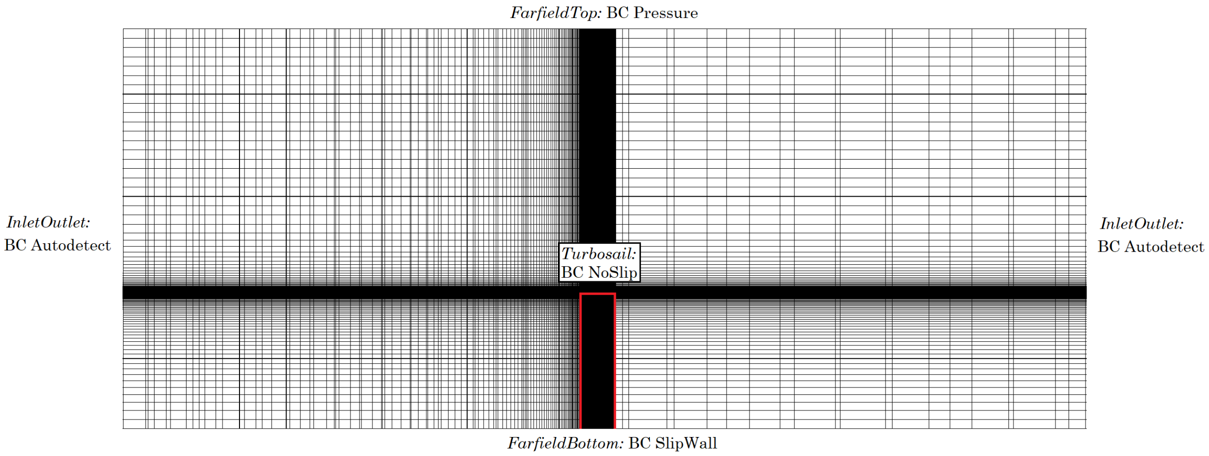

Figure 5.9: yz-plane for finite aspect ratio A_R=5.5.

5.4 ReFRESCO

The used software for conducting the CFD computation is ReFRESCO, the in house CFD software from MARIN. The official description for the solver ReFRESCO is quoted below from the ReFRESCO website [38].

ReFRESCO (www.refresco.org) is a community based open-usage CFD code for the Maritime World. It solves multiphase (unsteady) incompressible viscous flows using the Navier-Stokes equations, complemented with turbulence models, cavitation models and volume-fraction transport equations for different phases. The equations are discretised using a finite-volume approach with cell-centered collocated variables, in strong-conservation form, and a pressure-correction equation based on the SIMPLE algorithm is used to ensure mass conservation. Time integration is performed implicitly with first or second-order backward schemes. At each implicit time step, the non-linear system for velocity and pressure is linearised with Picard's method and either a segregated or coupled approach is used. In the latter, the coupled linear system is solved with a matrix-free Krylov subspace method using a SIMPLE-type preconditioner. A segregated approach is adopted for the solution of all other transport equations.

The implementation is face-based, which permits grids with elements consisting of an arbitrary number of faces (hexahedrals, tetrahedrals, prisms, pyramids, etc.), and if needed h-refinement (hanging nodes). For turbulence modelling, both RANS/URANS and Scale-Resolving Simulations (SRS) models such as SAS, DDES/IDDES, XLES, PANS and LES approaches can be used. The code is parallelised using MPI and subdomain decomposition, and runs on Linux workstations and HPC clusters.

Chapter 6

2D Results

This chapter reveals the results of the 2D numerical computations of testcase 1.1-1.6 in section 6.1-6.6.

6.1 Domain variation

The domain size around the Turbosail is an important quantity to consider, when one is interested in calculating the lift and drag coefficient of the Turbosail. Since the Turbosail is promised to generate very high lift coefficient around $C_L = 8$, the mass flow is redirected, which is essentially the main principle that lift is produced on a wing. This can also clearly be seen in figure 6.6, where the streamlines are shown and are redirected after interacting with the Turbosail. The influence of the domain size is also proven to be important by Peyro [22], who performed a numerical study about a stabilizer fin using ReFRESCO. Peyro stated that a domain with a total length and height of at least $[H, L] = 35 \cdot L_c$ is needed to accurately determine the lift coefficient. However, for this fin, the produced lift is approximately around 0.6, which is more than a factor 10 less than the generated lift of a Turbosail. Since the domain size may influence the results when is chosen to small, a domain variation study is carried out in test case 1.1.1-1.1.5 to determine a sufficient domain size.

The grids are assembled from one rather fine base grid, counting 764 points along the Turbosail profile, which is extruded in normal direction for different radii, resulting in different domain sizes. The method of assembling a grid with different domain size is described in the following. For an initial grid with radius, R, of 20 times the chord length, $R = 20 \cdot L_C$, gives a grid with 764 x 628 = 479.792 cells. Subsequently, for larger radii, the grid is further expanded (in normal direction) with the same growth ratio. A number of grids are generated with different radii of 20, 50, 100, 200 and 500 metres (chord length, $L_C = 0.996m$), which correspond to testcase 1.1.1-1.1.5 respectively. In table 6.1, the lift and drag coefficient, including the order of convergence denoted with C_{it}, are presented for a constant suction pressure of $p_{suc} = -287Pa$. This suction pressure corresponds for testcase 1.1.1-1.1.5 with an suction coefficient of $C_q = 0.047$.

Table 6.1: C_L and C_D coefficients for different domain sizes with radii, R for an angle of attack $\alpha = 30$, with a suction speed of Cq = 0.047 .

Testcase ID	**R** [m]	**xy plane cells**	C_L [-]	C_D [-]	C_{it}
1.1.1	20	764 x 628	7.756	0.499	$5.2 \cdot 10^{-}8$
1.1.2	50	764 x 681	7.894	0.346	$5.6 \cdot 10^{-}8$
1.2.2	100	764 x 721	7.947	0.294	$1 \cdot 10^{-}8$
1.1.4	200	764 x 761	7.967	0.267	$5.8 \cdot 10^{-}8$
1.1.5	500	764 x 814	7.982	0.251	$5.6 \cdot 10^{-}8$

It can be observed from table 6.1, that the lift coefficient C_L increases while the drag C_D reduces for larger radii, R for the domain size. This difference in lift and drag is caused by a different pressure field around the Turbosail, which is visualized for the complete domain for a small pressure range in figure 6.1. The pressure boundary from autodetect is set at $p_{t,rel} = 0\ Pa$, which can clearly be observed by the green edge region. This boundary pressure of zero, affects the pressure distribution inwards to the

Turbosail. Small differences in the pressure distriubtions between both solutions lead to different stream lines that lead eventually to difference in lift and drag.

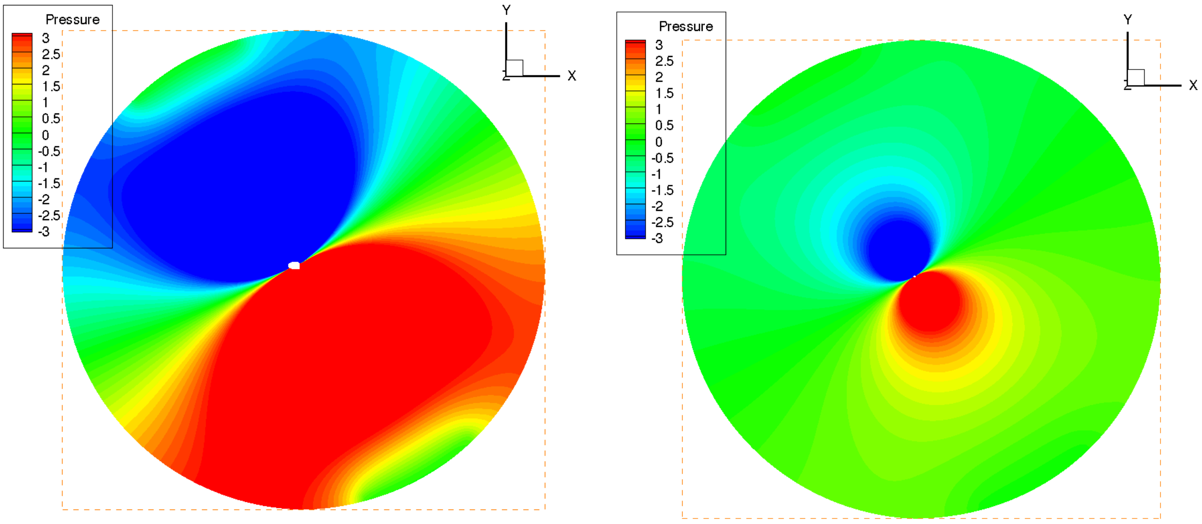

(a) Testcase 1.1.1 with domain radius of $R = 20 \cdot L_C$ (b) Testcase 1.1.3 with domain radius of $R = 100 \cdot L_C$

Figure 6.1: Global pressure field around Turbosail for a 2D flow

In figure 6.2, the dimensionless pressure distribution Cp along the profile is shown for three different radii, R = [20m, 100m, 500m]. Comparing test case 1.1.1 and 1.1.5 for a radius of 20m and 500m respectively, the increased lift and reduced drag for a radius of 500m is caused by a lower maximum pressure at suction side of the profile, while at the pressure side the pressure is similar for both cases. A radius of R=100m requires 14% additional cells, while a radius of R=500m needs 30% more cells. The accuracy in lift is however not so much affected, which differs with -0.4% between R=100m and R=500m. Although the drag coefficient C_D is somewhat +17% higher for R=100m compared to R=500m, the portion relative to the total resultant force is just +0.5 %. The decision is made to use a radius of R=100m, for the further 2D and 3D calculations in the xy-plane.

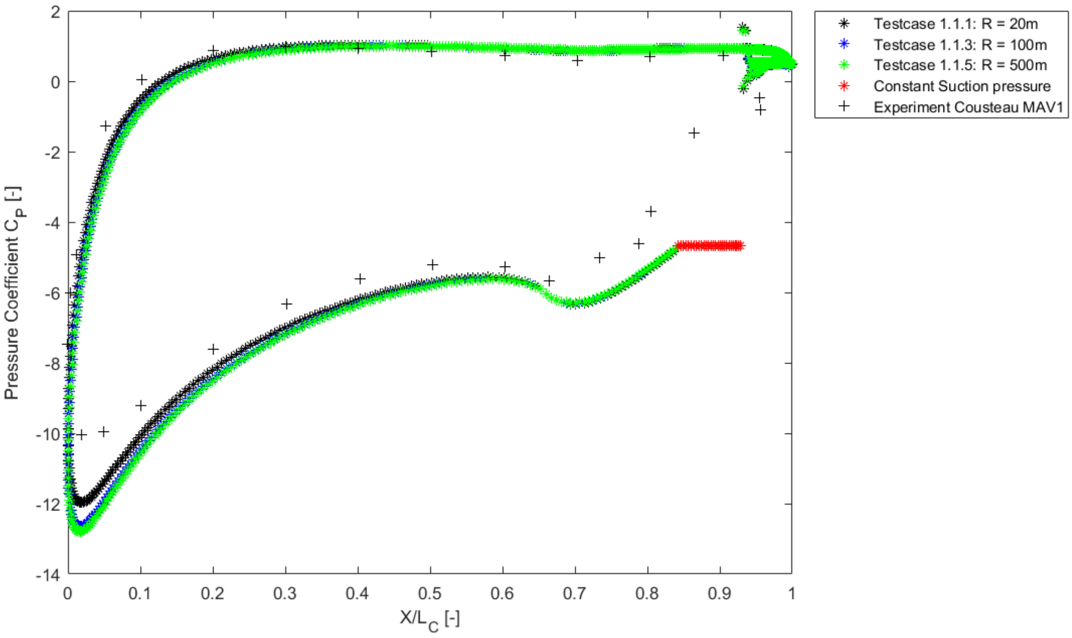

Figure 6.2: Dimensionless pressure distribution, C_P, as function of the x-coordinate along the Turbosail surface using the SRANS SST turbulence model for different domain radii, R.

6.2 Grid Refinement study

When doing real experiments to analyse the flow around objects, one is always interested in predicting the uncertainty in the experiments. Similarly, for numerical simulation one also needs to quantify the numerical uncertainty or error of the model.

In section 6.1, a justified domain size is selected which shows that a radius of $R = 100m$ is a good compromise between additional cells and accuracy of calculating lift and drag coefficients.
As a continuation, this section estimates the numerical error proposed by the method of Eça & Hoekstra [23]. The numerical uncertainty of a model can be subdivided in discretization error $U_{discretization}$, iterative error U_{it}, and round-off error $U_{round-off}$, see equation 6.1.

$$U_{num} = U_{round-off} + U_{it} + U_{discretization} \tag{6.1}$$

The method of Eça and Hoekstra shows how to estimate the discretization error $U_{discretization}$, which will now be denoted with ϵ_ϕ of a quantity ϕ (C_L and C_D in this case), to find the numerical uncertainty U_ϕ of the exact solution ϕ_{exact} by a grid refinement study, which can be reviewed in Appendix D. The method is valid under the condition that the solution is converged to a sufficient level, so that the iterative error is two orders smaller than the discretization error. Also the round-off error must be two orders lower than the discrization error, to accurately predict the discretization error. From common practice, it is often true that a double precision accurate computation give a round-off error which is at least two order lower than the discretization error.

The calculation consist of a 2D steady RANS simulation using the SST turbulence model of Menter, described in section 4.4.1. which are solved in testcase 1.2.1-1.2.6 for grid 1-6 respectively, see table C.2 in Appendix C. The convergence rate of the computations was below $4 \cdot 10^{-}7$, which leaded to a sufficient convergence of the forces in the order have a iterative error around approximately 0.1%. At the suction BC, a pressure of $p_{suc} = -287Pa$ is applied to obtain a suction coefficient of $C_q = 0.047$. In figure 6.3, the C_L and C_D results of testcase 1.2.1-1.2.5 for 5 grids of different grid size are presented as function of the relative grid size step, h_i/h_1, where subscript i refers to the grid number. The coarsest grid 6, of testcase 1.2.6 was out of the asymptotic range and is not included in the uncertainty estimation. As an example on this relative step size definition, in one dimension (x or y), the refinement factor is $\sqrt{2}$ so that the $h_2/h_1 = \sqrt{2}$. Finally by finding a polyfit according to the procedure of Eça and Hoekstra, the numerical uncertainty U_ϕ for C_L and C_D can be estimated for a particular grid. A power series expansion with p = 1.65 and a weighted approach leaded to the best fit through the data point, see figure 6.3. It is decided to quantify the uncertainty for grid 4, which is a sufficient grid to do the further analysis of testcase 1.3 - 1.6. The uncertainty U_ϕ for grid 5 is presented in figure 6.3 for C_L and C_D and shows that U_ϕ is about 0.9% for C_L and significantly larger for C_D with $U_\phi = 9.1\%$.

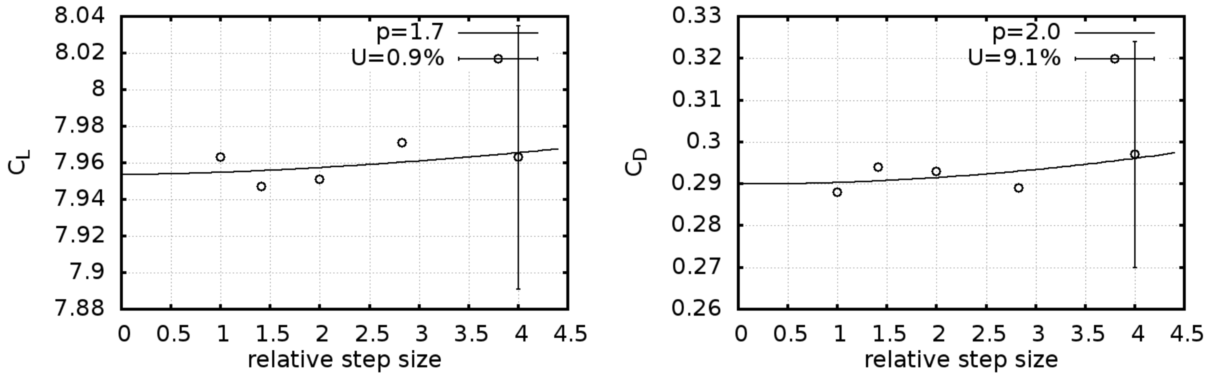

(a) Testcase 1.2.4: without transition modeling.

(b) Testcase 1.3.1: with transition modeling.

Figure 6.3: Method of grid generation

6.3 Local Correlation Transition Modeling

In this section, the influence of the LCTM model, introduced in section 4.4.2 is investigated for two grids, grid 3 and 4 in table 5.4. The turbulence intensity and eddy viscosity at the inlet need to be specified in such a way, that the desired turbulence intensity is reached in front of the Turbosail. For testcase 1.3.1 and 1.3.2, the turbulence intensity and eddy viscosity is chosen to be small, in order to have a region with a laminar boundary layer. From Eça et al [31] it is found that the standard SST model without transition modeling often gives a too early production of a turbulent boundary layer, while in reality the boundary layer is laminar. From testcase 1.3.1 and 1.3.2, it is expected to see a change in the transition point from laminar to turbulent and it is interesting to see if this change in transition point affects the lift and drag coefficients considerably. The turbulence intensity I in front of the profile is set at a very low value of I = 0.024% with an eddy viscosity of $\mu_t = 0.33\mu$. For Eça et al [31] it is found that low values for turbulence intensity ($I \approx 0.2\%$) give the largest region in the boundary layer to be laminar, thus the largest effect on the numerical solution.

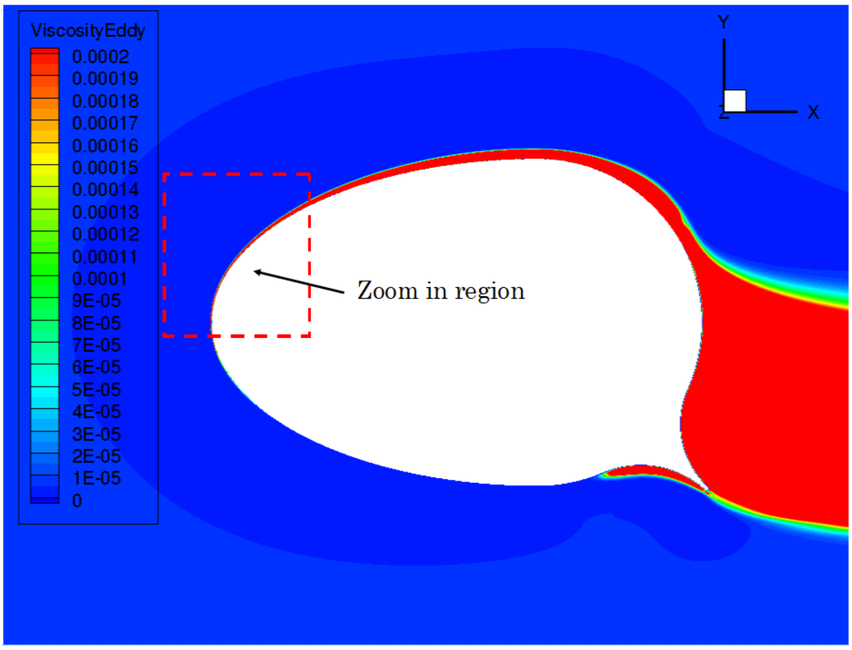

Figure 6.4: Testcase 1.2.4: Global contours for eddy viscosity μ_t without transition modeling.

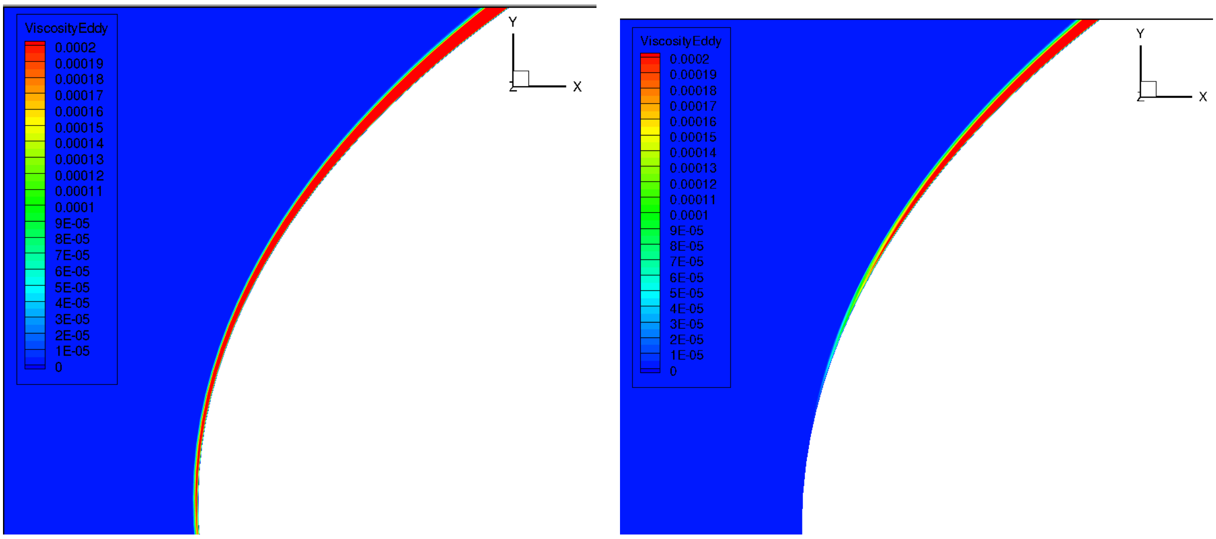

(a) Testcase 1.2.4: without transition modeling.

(b) Testcase 1.3.1: with transition modeling.

Figure 6.5: Comparison of eddy viscocity in boundary layer in the zoomed in region at the leading edge.

A boundary layer can be characterized as being turbulent, when the eddy viscosity μ_t, (which is directly related to the kinetic energy) with relation to the dynamic viscosity μ has a ratio of $u_t/u > 1$. Therefore, the eddy viscosity is compared between the turbulence models with and without transition model of testcase 1.3.1 and 1.2.4 respectively. The global contours of the eddy viscosity for testcase 1.2.4 without transition model is presented in figure 6.4. Differences between with or without transition modeling, appear at the leading edge region as expected as can be seen in figure 6.5. The region of a turbulent boundary layer is shifted slightly in the direction of the trailing edge, but this effect has hardly any influence on the total forces. The lift and drag coefficients of testcase 1.3.1 and 1.3.2 are presented in table 6.2 and shows hardly any difference compared to testcase 1.2.3 and 1.2.4 without transition modeling.

From these observations, it is concluded that the transition model does not lead to different values for lift and drag for estimating the 2D lift coefficient for infinite span. Furthermore, for a full scale Turbosail with a total span of 11 metres, it is expected that the transition model becomes less relevant, since the Reynolds number is higher than $Re > 1 \cdot 10^6$ and is almost beyond the region where transition modeling is important.

Table 6.2: Comparison of lift and drag coefficients with and without transition modeling.

Testcase ID	**Grid nr i**	C_L	C_D	$C_{it,\gamma}$
1.3.1	4	7.958	0.290	$1.6 \cdot 10^{-}4$
1.3.2	3	7.938	0.295	$2.4 \cdot 10^{-}4$

6.4 2D Steady SST Results

This section shows the results of the calculated lift and drag coefficients for a range of angles of attack α and at two suction speeds, $C_q = 0.047$ in testcase 1.4.1-1.4.7 and $C_q = 0.032$ in testcase 1.4.8-1.4.13. In section 6.2, the numerical uncertainty is estimated for grid 4, which is selected for current test case 1.4. The solved equations consist of a 2D steady state RANS using the SST turbulence model of Menter 2003 [32], reviewed in section 4.4.1. In table 6.3 and 6.4, C_L and C_D are solved for a suction of $C_q = 0.047$ and $C_q = 0.032$ respectively. The suction coefficient of $C_q = 0.047$ and $C_q = 0.032$ is realized by process of trial and error by choosing the suction pressure smartly by interpolation, which gives different required suction pressure p_{suc}, see also table 6.3 and 6.4. The method of calculating the suction coefficient C_q is given in section 5.3. In section 6.6, the steady and unsteady results of the 2D simulation are presented in the C_L,C_D curves in figure 6.15.

Table 6.3: Lift and drag coefficients for 2D steady RANS computations using SST turbulence model for a range of angle of attack α at a suction rate of $C_q = 0.047$

Testcase ID	α	C_L	C_D	p_{suc} [Pa]	C_q [-]
1.4.1	0	4.04	0.146	-310	0.0469
1.4.2	5	4.79	0.175	-317	0.0473
1.4.3	10	5.52	0.203	-320	0.0476
1.4.4	15	6.22	0.227	-318	0.0472
1.4.5	20	6.88	0.246	-312	0.0461
1.4.6	25	7.49	0.270	-305	0.0475
1.4.7 =1.2.4	30	7.97	0.289	-287	0.0480

Table 6.4: Lift and drag coefficients for 2D steady RANS computations using SST turbulence model for a range of angle of attack α at a suction rate of $C_q = 0.032$

Testcase ID	α	C_L	C_D	p_{suc} [Pa]	C_q [-]
1.4.8	0	3.81	0.13	-275	0.0318
1.4.9	5	4.58	0.1436	-282	0.0312
1.4.10	10	5.32	0.1617	-285	0.0311
1.4.11	15	5.99	0.1795	-282	0.0313
1.4.12	20	6.53	0.2001	-270	0.0325
1.4.13	25	6.80	0.2207	-235	0.0326

From table 6.3 and 6.4, it can clearly be seen that C_L and C_D both increase, for higher angles of attack α which is the main principle of lifting devices. Comparing the two suction speeds of for example case 1.4.6 and 1.4.13 shows what is expected from the experiments of Cousteau, a higher suction speed gives a higher lift force.

The velocity contours along the Turbosail are presented for $\alpha = 10°$ and $\alpha = 30°$ at $C_q = 0.047$ in figure 6.6a and 6.6b respectively. It can be observed for both angle that in the wake of the flap, there is a recirculation region, where the flow is detached from the main stream velocity. This is also expected, since at a sudden point, the flow becomes separated from the boundary layer, when the pressure gradients become too large.

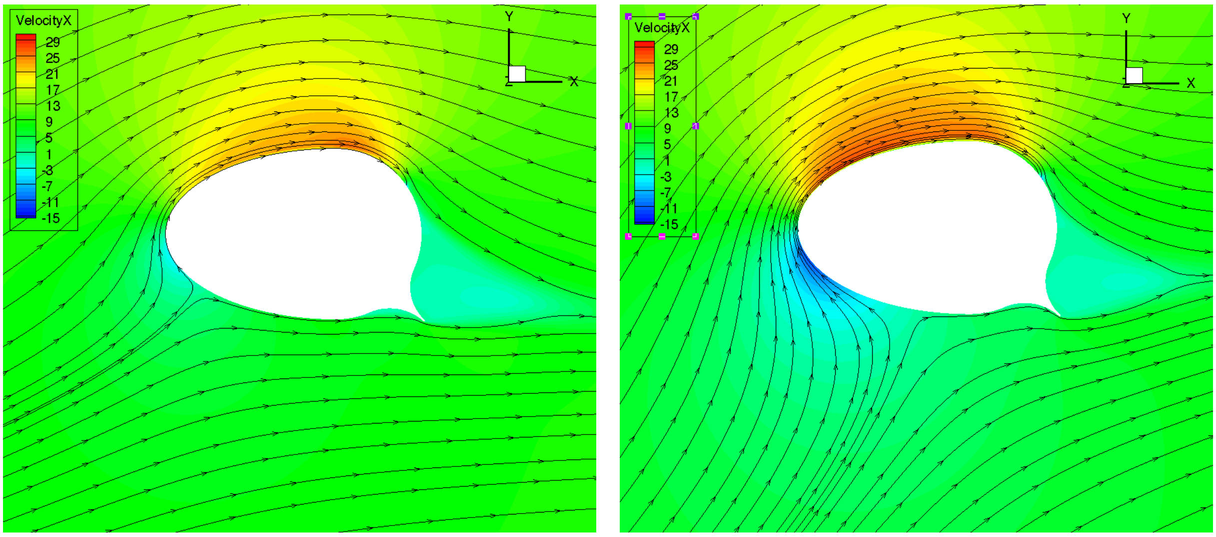

(a) Testcase 1.4.3: $\alpha = 10°$.

(b) Testcase 1.4.7: $\alpha = 30°$.

Figure 6.6: Results for 2D steady RANS SST, showing the velocity in x-direction for two angles of attack, α.

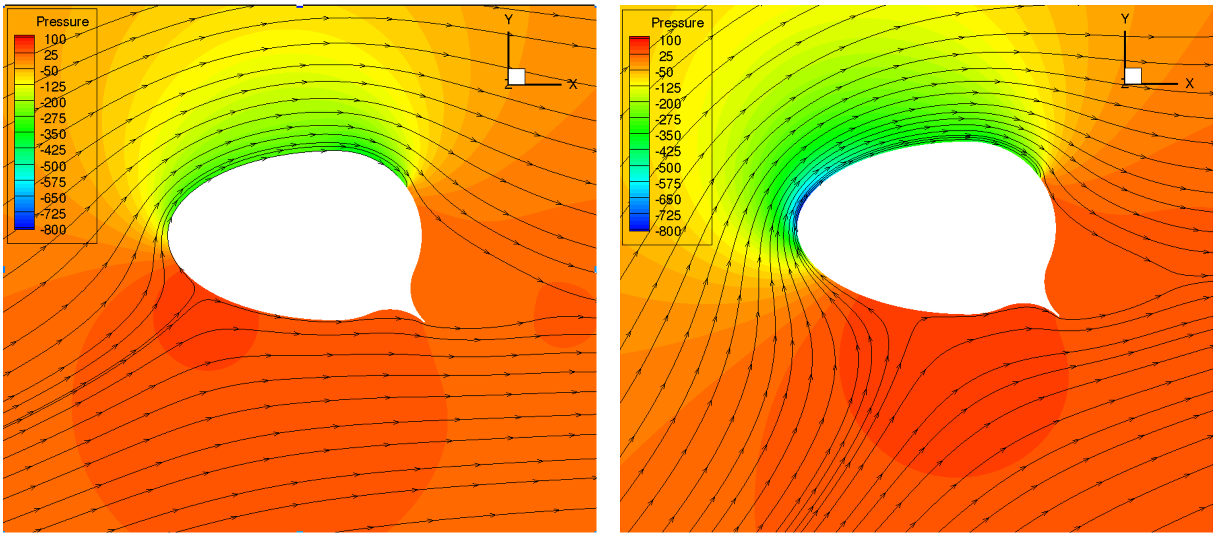

(a) $\alpha = 10°$

(b) $\alpha = 30°$

Figure 6.7: Results for 2D steady RANS SST, pressure field for two angles of attack, α.

Evaluating the required suction pressure p_{suc} in table 6.3 at $C_q = 0.047$, it can be seen that the largest minimum peak occurs at an angle of $\alpha = 10°$, with a suction pressure of $p_{suc} = -320$ Pa for testcase 1.4.3. This lower required pressure can be explained by the fact that the minimum pressure region is located in the middle of the chord length at the suction side of the profile, see figure 6.7a.

For larger angles of attack, for example $\alpha = 30°$ in figure 6.7b , the lower pressure peak shift more forward to the leading edge, increasing the lift significantly. This low pressure is a result of the accelerated air stream, which leads according to the law of Bernoulli to a low pressure, see equation 5.7. Moreover, the suction pressure p_{suc} reduces slightly to a lower minimum peak of $p_{suc} = -287$ Pa. Consequently, this means that the fan installed on the Turbosail needs less power at a constant suction speed C_q, for a higher angle of $\alpha = 30°$ compared to $\alpha = 10°$.

6.5 2D Unsteady SST, time step variation

As a second model,the RANS equations are solved in transient mode, which includes the local time derivative, $\frac{\partial u_i}{\partial t}$, of equation 4.16. A three time level implicit backward discretization scheme is used in ReFRESCO. A CFL number of 10 or lower is advised, for numerically stable and accurate results. For explicit, a rule of thump is to set the CFL below 1, however when using a implicit time discretization scheme, larger CFL number are omitted. The definition of the CFL number can be revised in equation 4.17. In table 6.5 a number of time steps Δt are selected for testcase 1.5.1-1.5.4 to see what is the effect of Δt on the solution. For each testcase, the local CFL number is presented around Turbosail in figure 6.9.

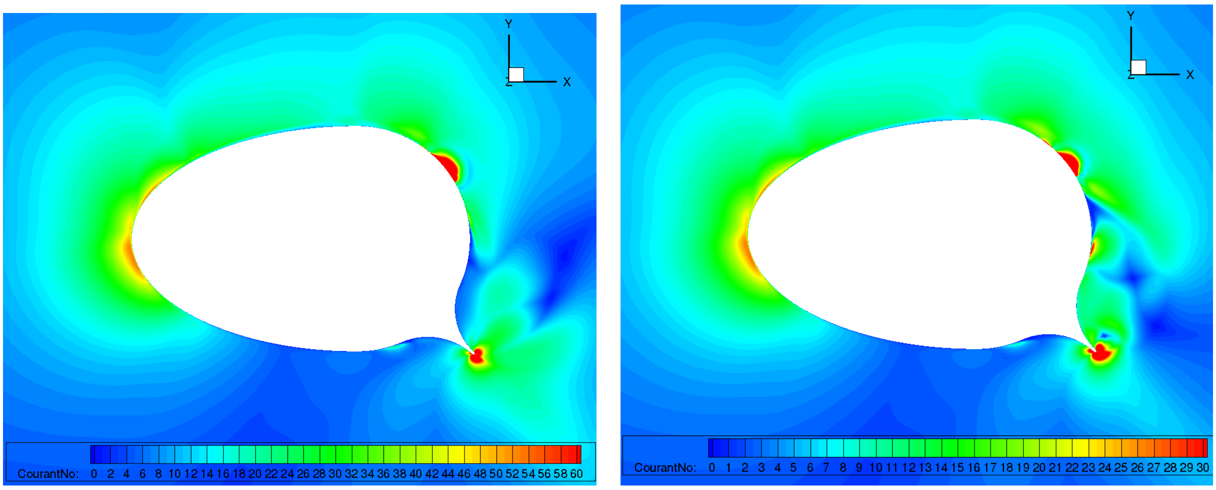

(a) $\Delta t = 0.01s, CFL_{ave} = 40$

(b) $\Delta t = 0.005s, CFL_{ave} = 20$

Figure 6.8: Results for 2D steady RANS SST, pressure field for two angles of attack, α.

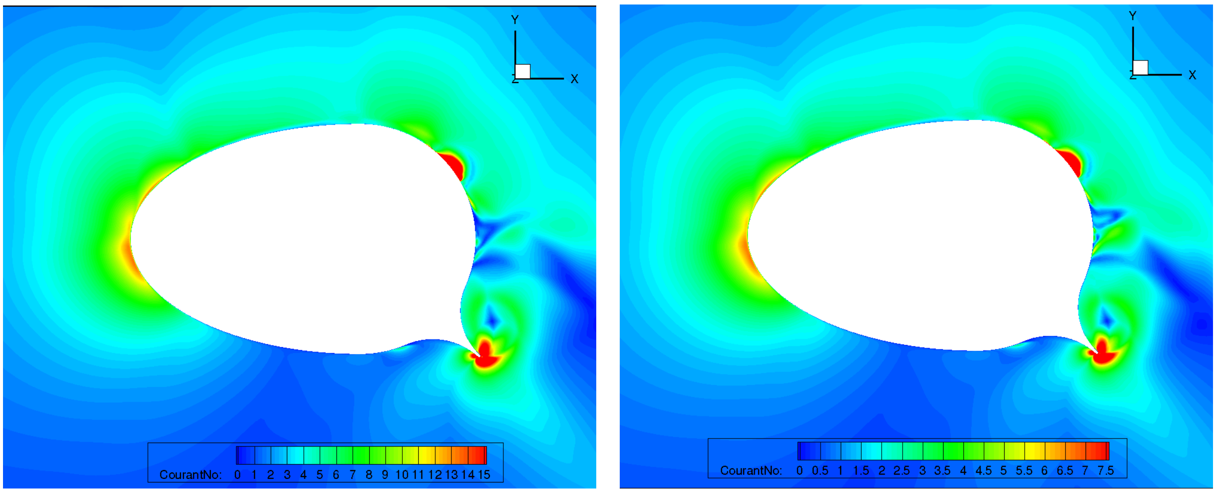

(a) $\Delta t = 0.0025s, CFL_{ave} = 10$

(b) $\Delta t = 0.00125s, CFL_{ave} = 5$

Figure 6.9: Local CFL number of testcase 1.5.1-1.5.4 for different time steps Δt, at constant angle $\alpha = 30°$ and a constant suction pressure of $p_{suc} = -287Pa$.

For every time step refinement of a factor two, the local CFL number reduces also with the same magnitude as expected. Outside the boundary layer the CFL number is below the given average, where the values are within light blue to green zone. Locally, in the boundary layer region and around the flap much higher CFL number occur. In order to meet CFL numbers below 1 in the boundary layer of the suction region, the time step size reduced to the order of $\Delta t = 10^{-6}s$, but this is computational very expensive.

When starting a transient calculation with CFD, the previous solution from a steady RANS calculation is often used to reduce the computational time. The solution from transient calculation, does not show immediately the desired average of the solution but requires a certain simulation time. In order to make qualitative quantification of the average lift and drag coefficient, the transient scanning technique (TST) of Brouwer et al [44] is adopted. The TST method uses the cumulative auto-covariance approach also given by Brouwer [45] over a given time series. The auto-covariance method calculates the standard deviation u_1 of the mean by equation 6.2.

$$u_1 = \sqrt{\frac{1}{T}\int_0^T \left(1 - \frac{\tau}{T}\right) C_{xx,biased}(\tau)d\tau} \tag{6.2}$$

where, τ is the time difference, $C_{xx}(\tau)$ is the autocovariance function for a stationary process and T is the time length of the signal.

A time history of the C_L and C_D are solved for the 2D URANS SST turbulence model and depicted in figure 6.10 for all 4 different time steps

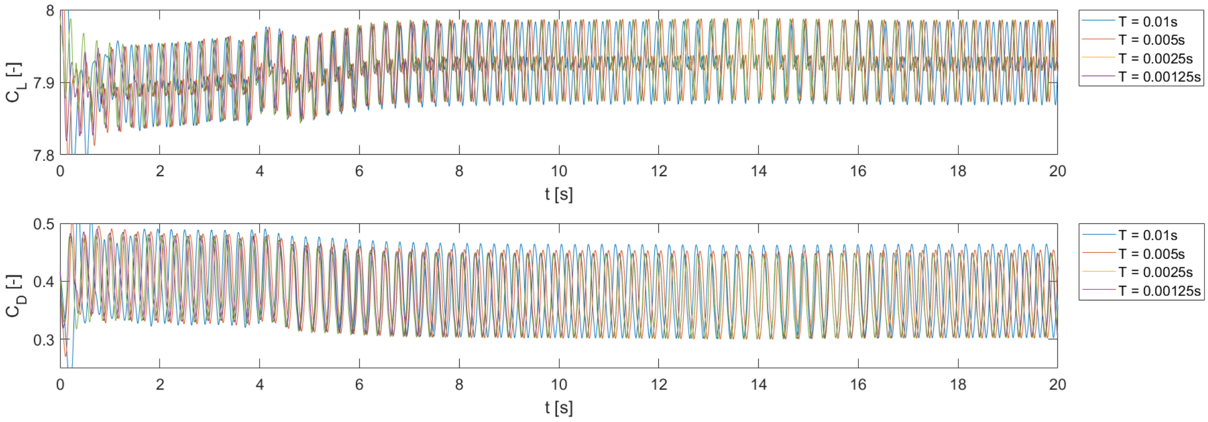

Figure 6.10: Time series for C_L and C_D of testcase 1.5.1-1.5.4.

For each timeseries of test case 1.5.1-1.5.4 in figure 6.10, the TST method is applied to calculate the uncertainty of the mean within 95% confidence bounds. The signal of the each time series is reversed, so that the typical 'hockey stick' can be observed when the uncertainty starts to increase due to start-up effects. The TST results for testcase 1.5.1-1.5.4 are presented in figure ??.

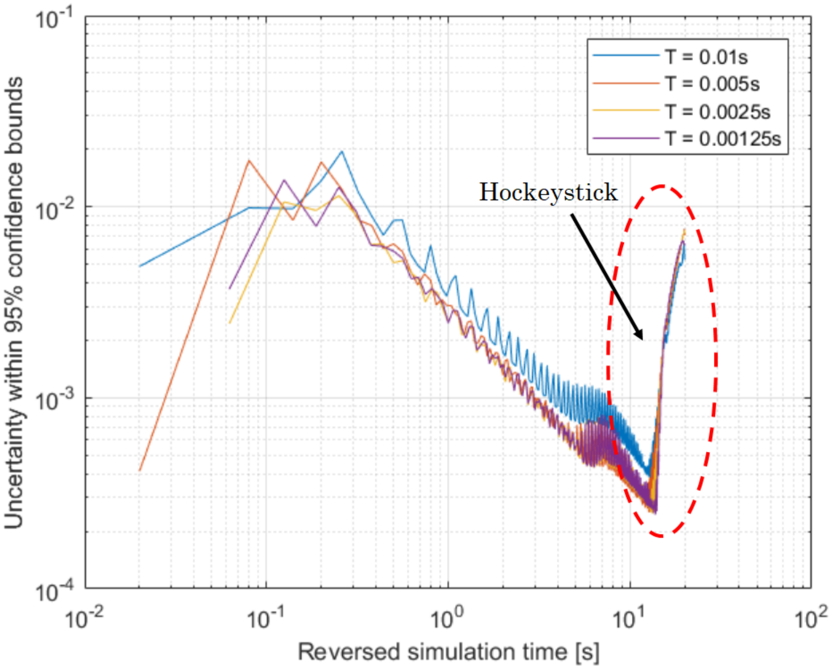

Figure 6.11: TST Results for testcase 1.5.1-1.5.4.

From the TST results in figure 6.11 and the time series in figure 6.10, a clear start-up effect (hockestick in the TST results) can be observed in the first period of the time signal ([T = 0-8s]). In table 6.5, the average of C_L and C_D are computed over [T = 8-20s] and the uncertainty u_1 is calculated for both C_L

and C_D. From table 6.5, it can be concluded that the differences between the timesteps for calculated mean value for C_L are almost negligible and for C_D are about 2% between testcase 1.5.1 and 1.5.4. For the next URANS calculations in testcase 1.6 of section 6.6, the selected time step is $\Delta t = 0.025s$, since the average CFL number is generally below $CFL < 10$. Also the TST results showed that the differences in C_L and C_D were small.

Table 6.5: Test case 5.1, Applying TST to estimate numerical uncertainty of the time signal.

Testcase ID	**Δt in [s]**	**Average CFL [-]**	$C_{L,mean}$ [-]	$U_{Cl,95} \cdot 10^{-3}$	$C_{D,mean}$ [-]	$U_{Cd,95} \cdot 10^{-3}$
1.5.1	0.01s	40	7.9279	0.4239	0.3823	0.4419
1.5.2	0.005s	20	7.93	0.2985	0.3775	0.5627
1.5.3	0.0025s	10	7.9302	0.3139	0.3753	0.5328
1.5.4	0.00125s	5	7.9306	0.361	0.3742	0.5623

6.6 2D Unsteady SST Results

From the time step variation study in section 6.5, a substantiated time step of $\Delta t = 0.0025s$ is selected to solve the unsteady RANS equations with SST turbulence model for a range of angles of attack, in testcase 1.6.1-1.6.14 for three suction coefficients of $C_q = [0;\ 0.032;\ 0.047]$. Additionally, a few number of angles of attack α are included to capture the stall point. The stall point is the situation where the Turbosail reaches its maximum lift, where after the lift collapses and the separation point in the boundary layer shifts towards the leading edge. The lift and drag coefficients can be reviewed in table C.7 - C.9 in Appendix C. From table C.9, it can be seen that the suction pressure is adapted with respect to the steady state result of testcase 1.4. In order to realize the desired suction coefficient of $C_q = 0.047$ and $C_q = 0.032$, the suction pressure p_{suc} is set at a lower minimum (pressure becomes more negative). By solving the RANS equations in transient mode, the constant pressure leads to a fluctuating mass flux through the aspirated suction region. As a result, the velocity in x,y components are monitored at the suction boundary for each time step, to find values for C_q over time. The suction coefficient is calculated by taking the average over the last 500 time steps. An example of the time history for C_q can be seen in figure 6.12.

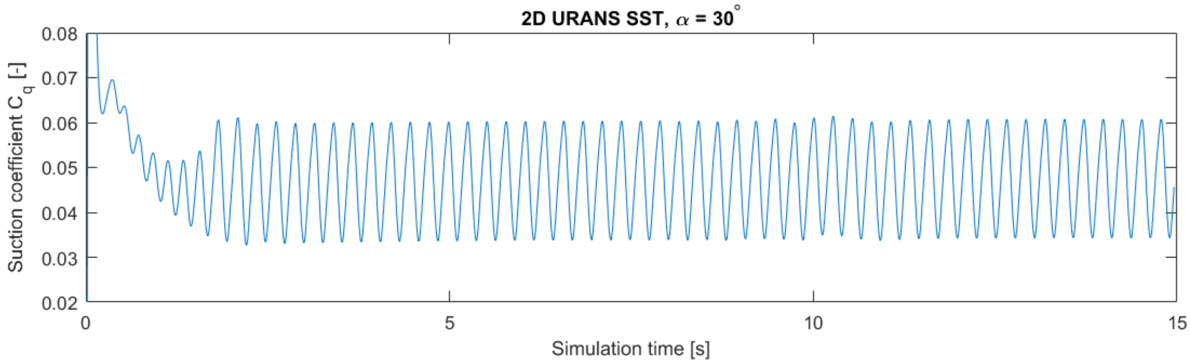

Figure 6.12: Suction coefficient C_q during the simulation time of URANS calculation of testcase 1.6.4.

The minimum and maximum values for C_q are also presented in table C.7 and C.8 to give an impression of the magnitude of the fluctuating suction speed. It can be questioned if this fluctuating mass flux occurs in reality, and as a recommendation for a next study, it would be more realistic and ideal to model the total inner domain or champer of the Turbosail to induce a more natural inflow through the suction boundary. From the current grid, it would not be so difficult built such a new model. Then, the fan can be modeled by an actuator disk (circular plane) as a constant pressure or a constant mass flow at the top or bottom.

From the velocity and pressure contours in figure 6.13 and 6.14 for $\alpha = 10°$ and $\alpha = 30°$, it can clearly be observed that the velocity in the wake has a different pattern compared to the steady state solution discussed in section 6.4. Although it is not entirely visible from one figure at a particular time step, the velocity and pressure fields show vortex shedding in the wake of the Turbosail, which has a completely different solution compared to the steady state solution in figure 6.6 and 6.7. The vortex shedding

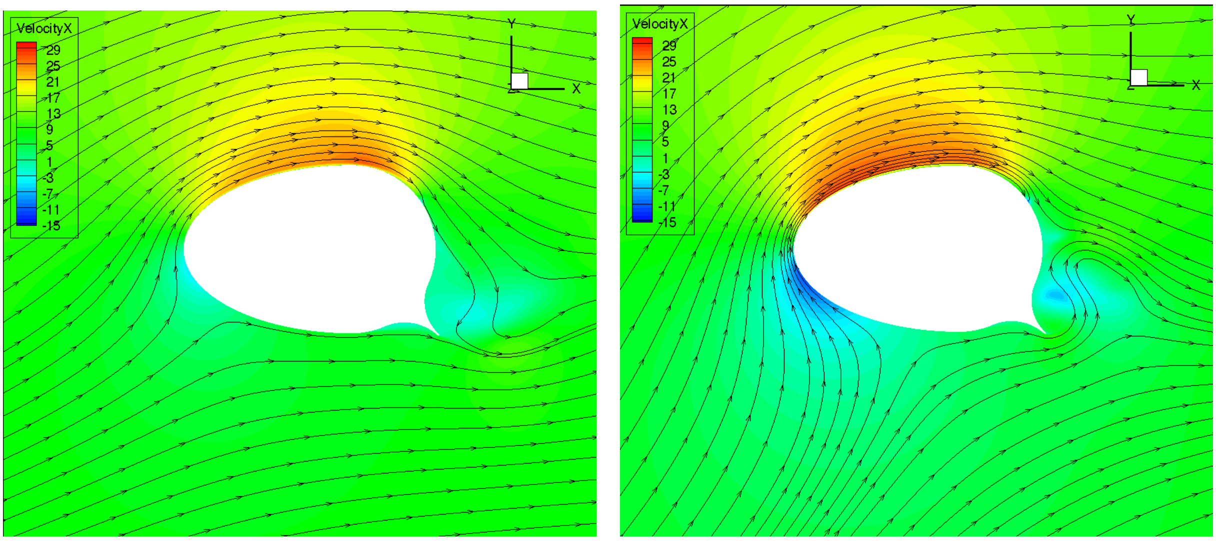

(a) Testcase 1.6.2: $\alpha = 10°$ (b) Testcase 1.6.4: $\alpha = 30°$

Figure 6.13: Results for 2D unsteady RANS SST, showing the velocity in x-direction for two angles of attack, α.

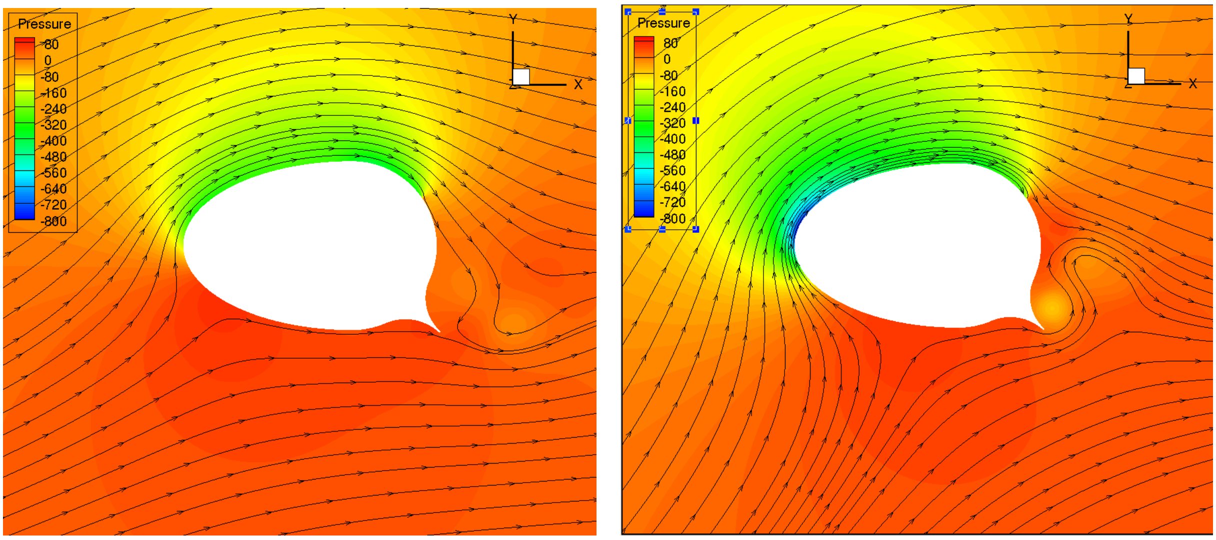

(a) Testcase 1.6.2: $\alpha = 10°$ (b) Testcase 1.6.4: $\alpha = 30°$

Figure 6.14: Results for 2D unsteady RANS SST computations, pressure field for two angles of attack, α.

behaviour, in combination with a lower minimum required suction pressure p_{suc}, accompanies with a higher drag coefficient.

In figure 6.15, a complete overview is given of the generated lift and drag coefficients for a range of angles of attack according SRANS and URANS with the SST model of testcase 1.4 and 1.6 respectively. To qualify if these numerical results are realistic, a comparison is made of lift and drag coefficients presented by Cousteau for infinite span, which are also included in figure 6.15.

6.6.1 Discussion of C_L and C_D at a suction coefficient of $C_q = 0.047$

Considering the lift coefficient of the SRANS and URANS computations in figure 6.15 for a suction coefficient of $C_q = 0.047$, it can be seen that the difference for C_L are relatively small. For small values of $\alpha < 15°$, the lift coefficient is larger for URANS than for SRANS. At $\alpha = 10°$, URANS gives 6,1% more lift compared to SRANS. For larger angles of attack however, for $\alpha > 25°$, the difference in C_L becomes less, about +2.2% higher C_L for URANS compared to SRANS at $\alpha = 25°$. The difference for small

α, may be declared by the fact that a higher suction pressure is imposed for URANS computations, to attain a similar average suction coefficient C_q. From the fluctuations in figure 6.12, it can be noticed that the maximum suction coefficient $C_{q,max}$, is 30% higher compared to the average value. The high peak values, may be responsible for an averagely higher lift forces at small α. The difference in suction pressure between URANS and SRANS becomes less at higher angles of α, where the dissimilarities between C_L where lower. As discussed earlier in the problem description of section 4.1, the 2D simulations model a turbusail wing of infinite span since the flow is forced to be only two dimensional. These 2D lift and drag coefficients can now be compared to the experimental results of Cousteau for infinite span for a suction speed of $C_q = 0.047$, also included in figure 6.15. As can be observed from this figure, the lift coefficients are in close correspondence to the calculated lift coefficients from the 2D numerical results. At an angle of $\alpha = 30°$, which is close to the optimum angle of attack before stalling, the C_L obtained from 2D SRANS and URANS are 4.5 % and 4.4 % lower compared to the C_L found by experiments of Cousteau.

However, the stall point of the experiments takes place at $\alpha = 32°$, while the URANS calculation shows that the stall point is approximately between $\alpha \approx 35° - 40°$. The maximum lift force is generated for $\alpha = 35°$, where $C_{L,max} = 8.27$. To better capture the exact stall point, it is desired to introduce more points for α between $35° - 40°$. This dissimilitude in stall point is rather large and can be due to a few reasons. At first, the Reynolds number at which the experiments are conducted from Cousteau, do not give specific information about the presented Reynolds number and uncertainty of the experiments. Therefore, the stall point can earlier be reached when the Reynolds number is lower. Another interesting aspect is that Cousteau also reports the lift and drag coefficients for a finite aspect ratio wing of $A_R = 4$, see figure 2.7. In this graph, the stall point is shifted to a larger angle of $\alpha = 38°$, where the Reynolds number is also for this case, not presented. It is thus not so remarkable that the numerical results follow the trend that the stall point is located in the region between $\alpha_{stall} \approx 35° - 40°$. An explanation could be the difference in Reynolds number, but this is still an hypothesis.

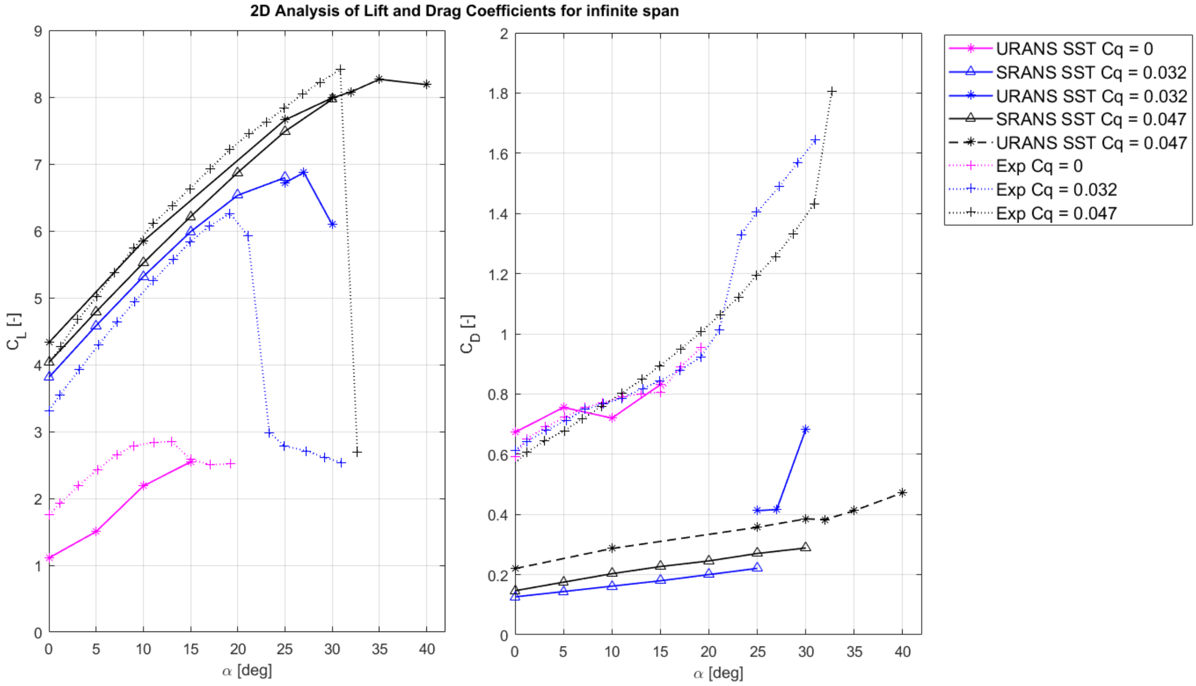

Figure 6.15: Comparison of the numerical results for lift and drag coefficients of steady and unsteady RANS calculations using the SST turbulence model, including the reported experimental results of Cousteau [1].

Regarding the drag coefficient C_D from figure 6.15, it can obviously be seen that there is a large discrepancy between the drag found by experiments and the numerical results of steady and unsteady computations. More specifically, for $\alpha = 30°$, the drag coefficient from experiments is $C_{D,exp} = 1.4$ while in contrary, SRANS and URANS give a much lower drag of $C_{D,\text{SRANS}} = 0.289$ and $C_{D,\text{URANS}} = 0.383$. It is not entirely clear how the experimental set up was from the experiments, therefore it is impossible to give a qualitative declaration why the gab between experiments and numerical prediction for drag are so large. A reason can be the effect of end plates on both ends in the experimental set up give additional drag. It is observed from the domain variation study in section 6.1 that the drag becomes larger when the distance to the farfield is reduced, thus for lower Radii of the domain size. For example, the drag already gives a value of $C_D = 0.5$ in testcase 1.1.1, for a domain radius of 20 metres. To make a fair comparison, the dimensions of the windtunnel should be modeled, since these parameters effect the lift and especially the drag considerably. Ideally, a more accurate subgrid resolving scale (SRS) model should be selected to obtain a higher accurate numerical result, for example DDES, XLES or LES to name a few. In the time span of this thesis, it eventually chosen to built a finite 3D model, to investigate the lift and drag coefficients of a finite Turbosail wing, which is discussed in section 7.4.

6.6.2 Discussion of C_L and C_D at a Suction Coefficient of $C_q = 0.032$

Now for the lower suction speed of $C_q = 0.032$, the expected pattern of a reduction of lift is observed for all angles of attack for both SRANS and URANS in figure 6.15. Unsteady RANS computation of testcase 1.6.8-1.6.10 are only carried out for the region where stall is expected, thus for $\alpha = [25, 27, 30]$ degrees, see table C.8. It can be observed that the difference for C_L between SRANS and URANS at $\alpha = 25°$ are almost equal. Beyond an angle of $\alpha > 27°$, the foil stalls and the lift collapses. The reduced suction coefficient of $C_q = 0.032$, has the positive quality that the mass flow is reduced by 32% compared to the higher suction coefficient of $C_q = 0.047$, while the maximum lift force is only reduced by 17 % from a $C_L = 8.27$ at $C_q = 0.047$, to $C_L = 6.87$ at $C_q = 0.032$. The optimal working point from operational point of view, depends on several parameters such as vessel speed, heading relative to the wind, wind speed, etc. and is discussed in chapter **??**.

The drag C_D, is however slightly increased to $C_D = 0.416$ at $C_q = 0.032$ for $\alpha = 27°$ compared to $C_D = 0.383$ at $C_q = 0.047$ for $\alpha = 35°$. This is in line from what is explained by Cousteau et al [1] that an increase of suction speed reduces the drag and increases the lift.

6.6.3 Discussion of C_L and C_D at zero suction speed, $C_q = 0$

At last, 2D unsteady RANS computations are performed for four angles of attack $\alpha = [0, 5, 10, 15]$ degrees in testcase 1.6.11-1.6.15, see figure 6.15 and table C.9. A good comparison can now be made to see the effect of applying boundary layer suction with respect to the situation when no suction or aspiration is applied.

Due to the asymmetry of the Turbosail, containing a flap, the Turbosail already starts to generate lift at zero angle of incidence. Although larger angles of attack have not been calculated, the maximum lift is reached at $\alpha = 15°$, where $C_L = 2.51$. It is however expected that the stall point is close to $\alpha = 15°$, since the increased lift (gradient of lift with respect to α) from 10 to 15 degrees, already start to decline. Comparing the lift of the numerical results with experiments, it can be seen that the numerical results under predict the lift for all angles of attack. At zero angle of incidence, experimental results already report a lift of $C_L = 1.8$, which seems rather high for a foil with a very small flap of just 15% of the chord length. It is doubted if these experimental lift coefficients are true, since the quality of the experiments such as the experimental uncertainty is unknown. The drag coefficient, however, shows more similitude between experiments and numerical results.

Chapter 7

3D Results

The 2D analysis in chapter 6, solves the flow only for x and y and disregards the z- direction in the momentum equations. However, the turbulence is 3D phenomenon and therefore it is important to see if a third dimension in z-direction would affect the lift and drag for an infinite aspect ratio wing, which is modeled with two frictionless walls. As mentioned in section 5.3, all boundary conditions remain unchanged, so that the frictionless walls are still considered as a 'symmetry' boundary condition.
In section 7.1, a refinement study is conducted by only varying the number of cells in spanwise direction. The goal is to investigate the influence of the grid density in z-direction, to make a selection of a sufficient amount of cells to accurately predict the spanwise flow for case of infinite span.
From the selection of number cells in z-direction, a range of angles of attack are computed using the steady RANS SST turbulence model in section 7.2. These lift and drag coefficients are compared to the 2D RANS SST numerical results of testcase 1.4, to see how the modeling of 3D flow affects the lift and drag coefficients.
In section 7.3, the SST turbulence model is replaced by the EARSM turbulence model. The EARSM model is already discussed in section 4.4.3, and uses Reynolds stresses to model anisotropic behaviour of a flow instead of the isotropic SST model, based on eddy viscosity according to the Boussinesq assumption.

7.1 Grid Refinement in Spanwise Direction

In testcase 2.1, a grid refinement in spanwise direction is made for a constant span length of h = 3m. The selected grid to be extruded in z-direction is grid 4 from the 2D analysis in table 5.4 which has 381 x 361 cell for the xy plane. In testcase 2.1.1-2.1.3, three grids are generated with a refinement factor of 2 in z-direction, where testcase 2.1.1 contains 70 cells in z-diriction, which gives 381 x 361 x 70 = 9.6 million cells. The lift and drag coefficient are calculated by solving the steady state RANS equations with the SST turbulence, where the results are shown in table 7.1.

Table 7.1: Lift and drag coefficients for infinite span at $\alpha = 30°$ and $C_q = 0.047$, using a 3D grid examining the refinement in z-direction.

Testcase ID	**Grid nr.**	**Nr. of cells in xy plane**	**Nr. of cells z- direction**	C_L	C_D	C_{it}
2.1.1	4.1	381 x 361	70	7.9661	0.2885	$1 \cdot 10^{-}8$
2.1.2	4.2	381 x 361	140	7.9663	0.2885	$1 \cdot 10^{-}8$
2.1.3	4.3	381 x 361	280	7.9661	0.2885	$1 \cdot 10^{-}8$

As can be seen from table 7.1, There is hardly any difference between the calculated lift and drag coefficients. This shows that the effect of the flow in spanwise direction has somewhat no influence on the calculated lift and drag by using the SST turbulence model. The effect of spanwise grid refinement on the velocity in z-direction is examined by placing a yz plane in the wake of the Turbosail at x = 0.5m. This plane is located 0.2m behind the Turbosail in the wake for grid 4.1 and 4.2, as can be seen in figure 7.1 and 7.2.

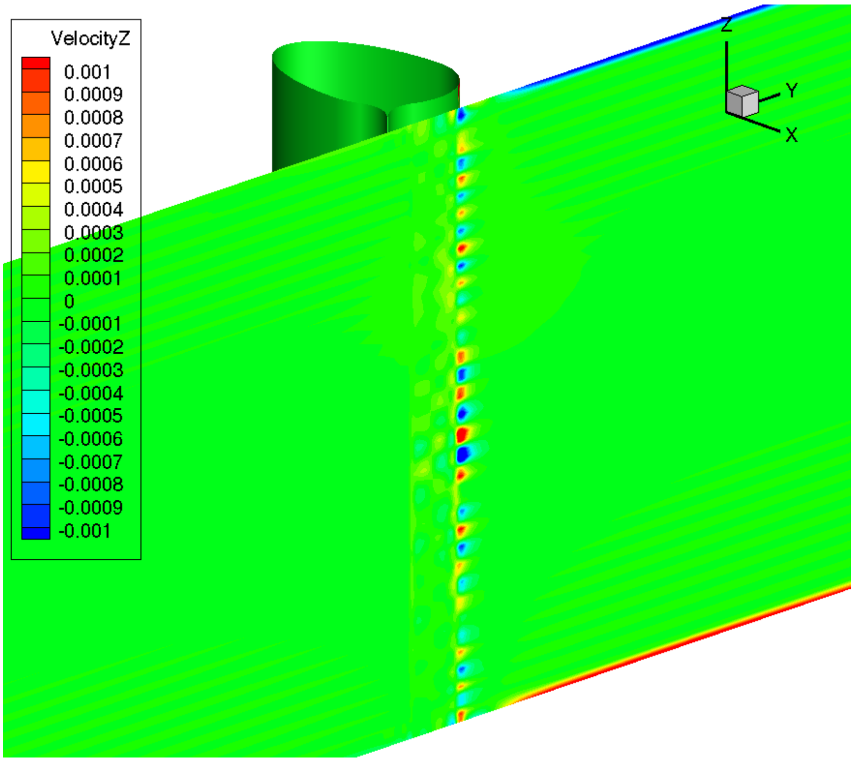

Figure 7.1: Velocity in z- direction for the yz plane at x = 0.5m for testcase 2.1.1 (grid 4.1).

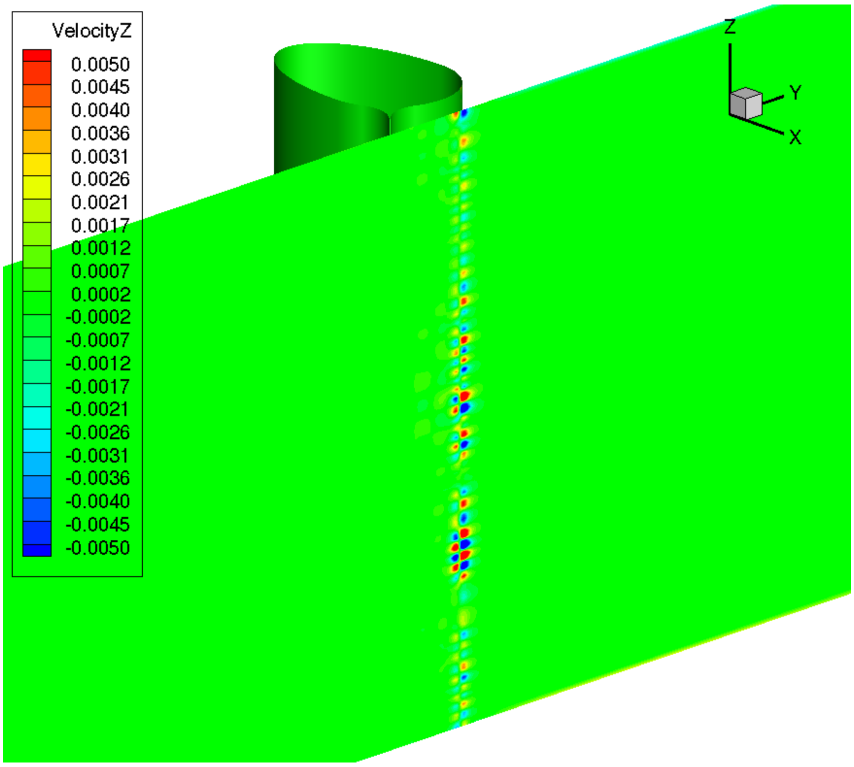

Figure 7.2: Velocity in z- direction for the yz plane at x = 0.5m for testcase 2.1.2 (grid 4.2).

In figure 7.1, For grid 4.1 in testcase 2.1.1, the z-velocity exhibits velocities between $U_z = -0.001 - 0.001 m/s$, which is of almost negligible magnitude compared to the free stream velocity of $U_\infty = 10 m/s$. Raising the number of cells by a factor two for grid 4.2, the z-velocities become a factor 5 larger, as can be seen in figure 7.2. Note that the axis range in the legend is scaled with a factor 5, to see the clear differences between grid 4.1 and 4.2. Further increasing the number of cells to 280, will give no significant change in z-velocities compared to 140 cells in grid 4.2. Therefore it is concluded that 140 cells in span direction are a sufficient amount to model any z- velocities in the SST turbulence model.

7.2 3D Steady SST Results

In section 7.1, a substantiated choice for the number cells in spanwise direction is chosen. This section calculates a range of angles of attack solving the steady RANS equations with SST turbulence model in testcase 2.2.1-2.2.7, which will be compared to the 2D SRANS computations of testcase 1.4.1-1.4.7 in section 6.4. As a first estimate for the suction pressure p_{suc}, the suction pressure is set to the value found by the 2D steady simulation of testcase 1.4. The computed results for lift and drag are presented in table C.11, which are compared to the 2D SRANS SST results of testcase 1.4 in figure 7.3. These lift and drag curves as function of α for the 3D SRANS SST model, give almost identical results to the lift and drag coefficients gathered from the 2D SRANS SST model.

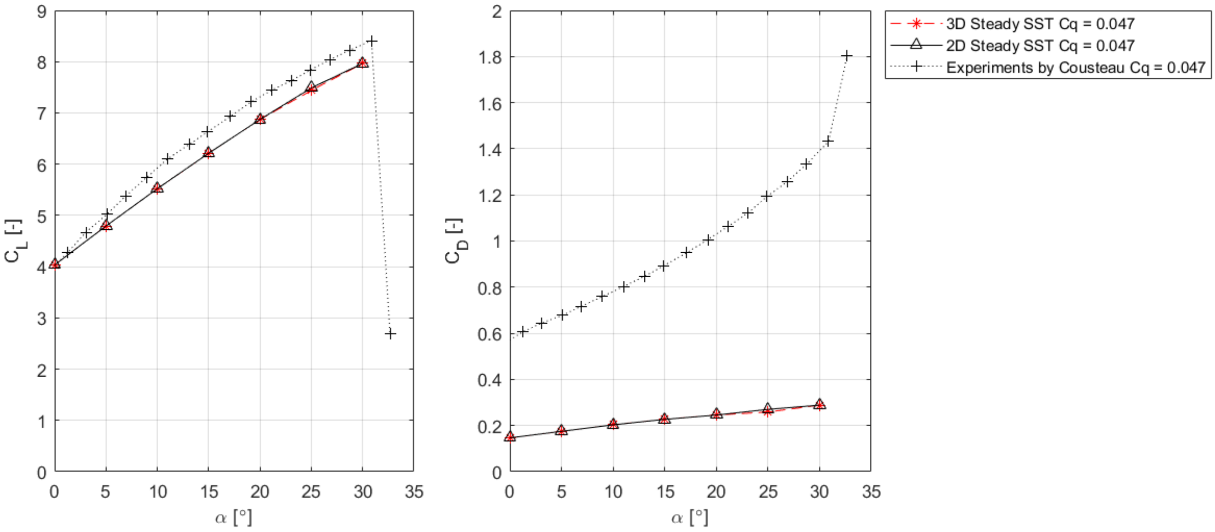

Figure 7.3: Lift and drag coefficients for 2D SRANS and 3D SRANS with the $k - \omega SST$ turbulence model for infinite span.

The velocity and pressure contours are examined for $\alpha = 30°$ in testcase 2.1.7, to compare with testcase 1.4.7 of figure 6.6b and 6.7b. As expected, the velocity and pressure profiles are identical. From this analysis it can be concluded that a 3D steady RANS calculation with the SST turbulence model does not give different results compared to the 2D SRANS SST computations. This shows that when the SST turbulence model is applied to calculate infinite span lift an drag coefficient, one suffices with setting up a 2D grid of one cell thick, which saves a considerable amount of computational resources.

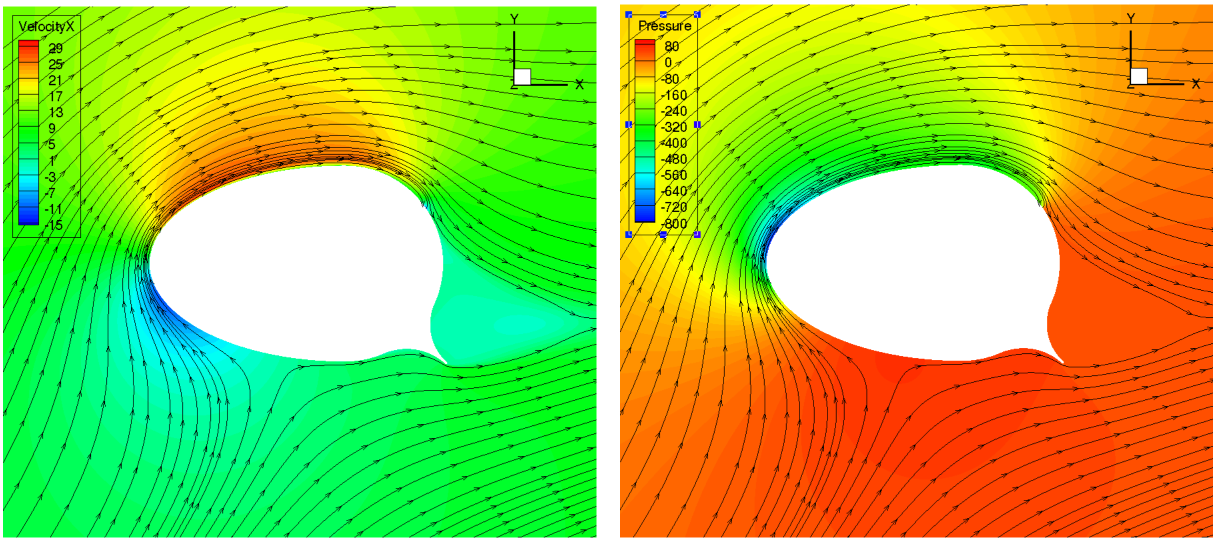

(a) Velocity in x-direction for $\alpha = 30°$.

(b) Pressure for $\alpha = 30°$

Figure 7.4: Results of testcase 2.1.7, velocity and pressure contours for 3D steady RANS SST computations

7.3 3D Steady EARSM

In the previous calculations, the SST turbulence model is used with and without transition modeling. As an expansion, the Explicit Algebraic Reynolds Stress Model (EARSM) model is investigated for one angle of attack, $\alpha = 30°$ in testcase 2.3.1 with grid 4.2 having 140 number of cells in spanwise direction. The EARSM model uses Reynolds Stresses to calculate the viscous stresses in the flow which accounts for anisotropy, in contrast to the SST model that assumes isotropic relation for the viscous stresses. In table 6.1, the calculated lift and drag coefficient are presented as well as the iterative convergence.

Table 7.2: Lift and drag coefficient of testcase 2.3.1 for 3D steady RANS computations using the EARSM turbulence model.

Testcase ID	α	C_L	C_D	p_{suc} [Pa]	C_{it}	C_q
2.3.1	30	7.938	0.283	287	$1 \cdot 10^{-5}$	0.047

The convergence rate stagnated at $1 \cdot 10^{-5}$ which is less compared to the SST model reach a convergence rate in the order of $1 \cdot 10^{-8}$. Scientifically, it would be desired to quantify this iterative error and also the discretization error, which might behave differently compared to the SST model. However, the discretization error is assumed to be in the same order of magnitude, but the reader should be aware of this assumption.

The velocity and pressure contours show similar values and streamline curvature compared to the 3D SST computation in testcase 2.1.7 in figure 7.4. However, differences appear in the wake, or recirculation area located at the aft of the flap. This wake has a more 3 dimensional and physical character, which also becomes clear after evaluating the velocity in z-direction in the yz-plane at x= 0.5m, see figure 7.6. The velocities in z-direction are in the order of 10% compared to the free stream velocity of $U_\infty = 10m/s$. In contrast to the SST model, the maximum z-velocities are in the order of 0.05% compared to the free stream velocity, which is almost a completely 2 dimensional flow. The effect of the more 3 dimensional flow on the total forces is very small, thus more physical modeling does not add accuracy for a case with infinite span.

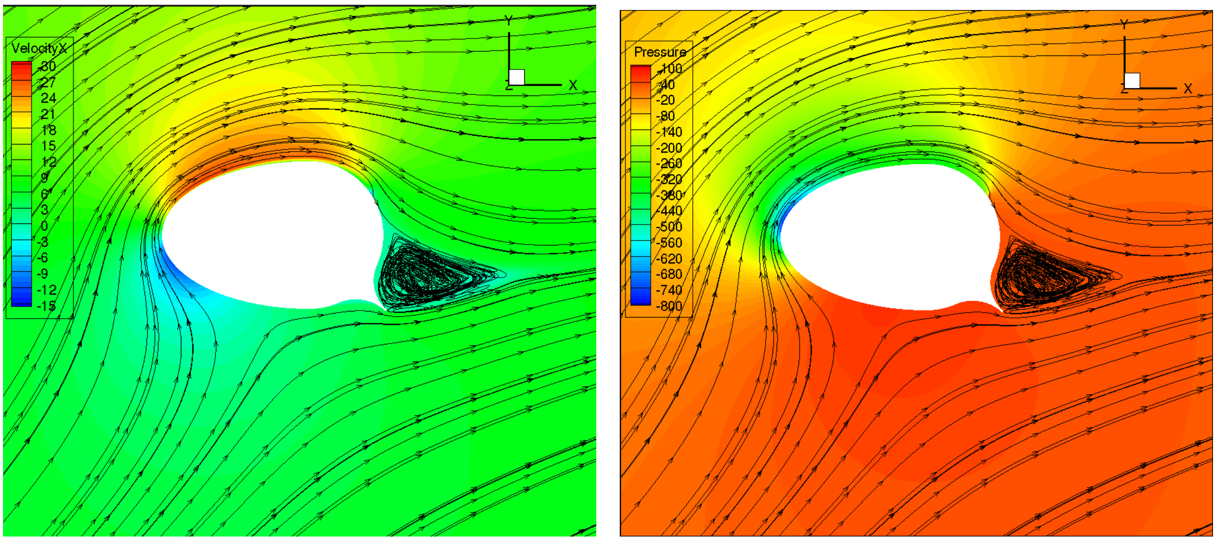

(a) Normal extrusion from profile. (b) Grid after extrusion

Figure 7.5: Solution for velocity in X-direction for testcase 2.3.2 and 2.3.5

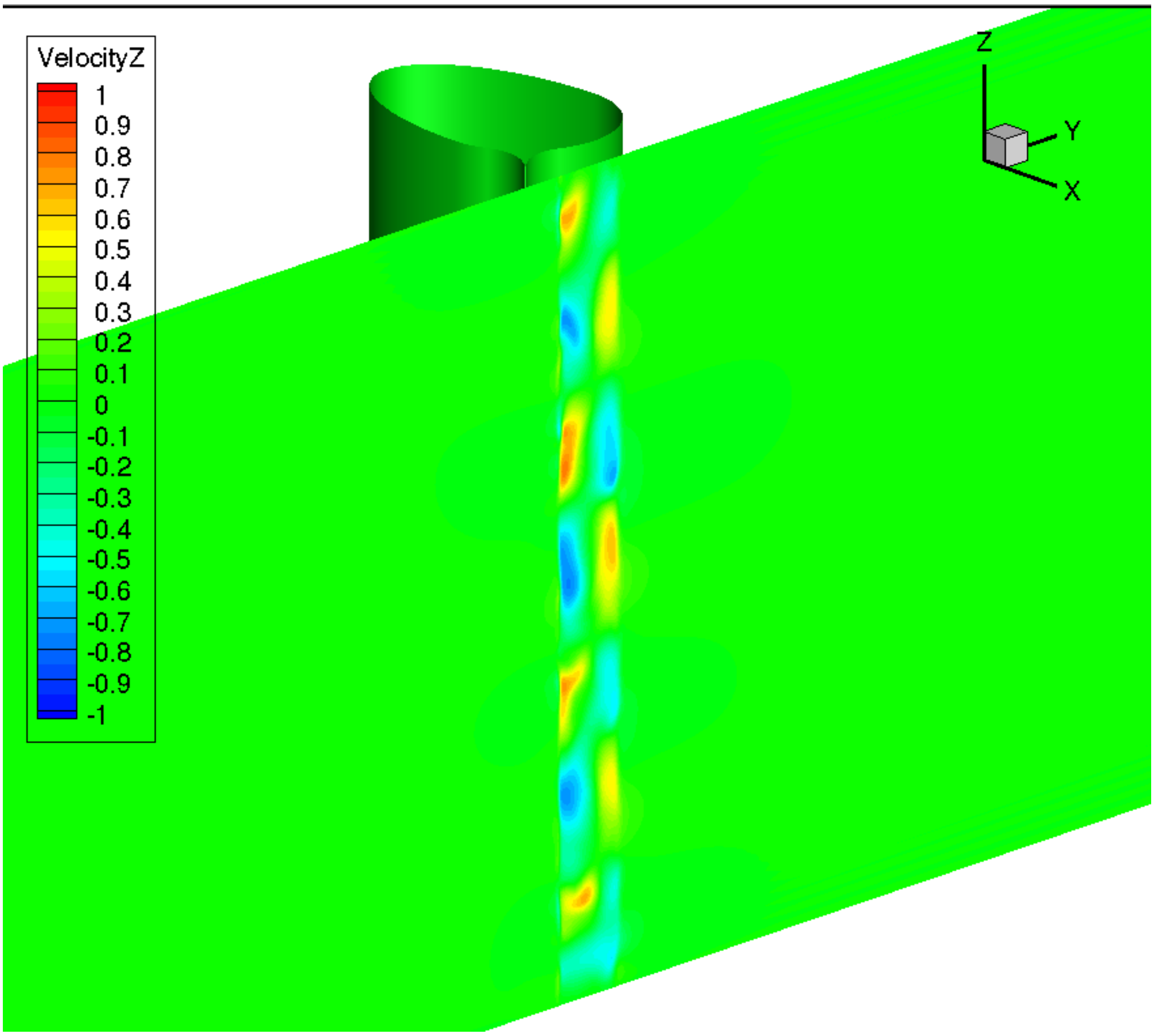

Figure 7.6: Velocity in z- direction for the yz plane at x = 0.5m for testcase 2.1.3 (grid 4.1).

7.4 Finite Turbosail, with an Aspect Ratio of $A_R = 5.5$

The most interesting case is to calculate the lift and drag coefficients for a single finite Turbosail with an aspect ratio of A_R=5.5, since a total of four Turbosails are conceptually placed on the ship in the FPP. In the analysis for a finite Turbosail, steady RANS computations are performed using the $k-\omega$ SST turbulence model, discussed in section 4.4.1. In section 5.3.1, the computational domain and the boundary conditions for the finite Turbosail are discussed. A modification to the suction region had to be made to improve the convergence of the calculation. Due to numerical instabilities, the suction region is not extruded along the full span of the Turbosail, but extruded from the bottom to just 8 centimetres away from the top, depicted in figure 7.8. The finite Turbosail is calculated for two suction speeds in testcase 2.4.1 and 2.4.2 and for one case with no suction in testcase 2.4.3. The results of testcase **2.4.1-2.4.3** are presented in table 7.3 and are discussed in the following. The average suction pressure C_{q,ave^*} is taken over a particular span height and is discussed in next section.

Table 7.3: Calculated lift and drag coefficients for a finite Turbosail with an aspect ratio of $A_R = 5.5$ for two suction speeds and one case without suction. For these test cases, the steady RANS equations are solved with the $k-\omega$ SST turbulence model.

Testcase ID	α	C_L	C_D	p_{suc} [Pa]	C_it	C_{q,ave^*}
2.4.1	30	5.78	1.44	-287		0.043
2.4.2	30	5.85	1.50	-300		0.050
2.4.3	15	1.32	0.39	no slip BC		

7.4.1 Aspiration results

The first suction speed is based on the 2D RANS SST simulations for infinite span of testcase 1.4.7 in section 6.4, where $\alpha = 30°$. It was found that the suction pressure required to assure a suction coefficient of $C_q = 0.047$, needs to be set at $p_{suc} = -287Pa$. This suction pressure is subjected to the finite Turbosail model in testcase 2.4.1. After analysing the suction coefficient along the total span of the foil for testcase 2.4.1, it was found that the desired suction coefficient of $C_q = 0.047$ was not obtained. In order to find the desired suction coefficient, a second suction pressure is chosen for testcase 2.4.2 and is set at $p_{suc} = -300Pa$.

In figure 7.8b, the velocity distribution in x-direction is presented for testcase 2.4.1. It is clearly visible that at the top, the amount of air flow through the suction boundary is way too high. When looking at the pressure contours at the top of the Turbosail of figure 7.8a, it can be seen that the pressure distribution around the suction region is lower compared to the suction pressure p_{suc}. Consequently, the high suction pressure results in a high suction speed at the top. The velocity in y-direction at the suction region in figure 7.8c gives a better representation of the amount aspirated air flow.

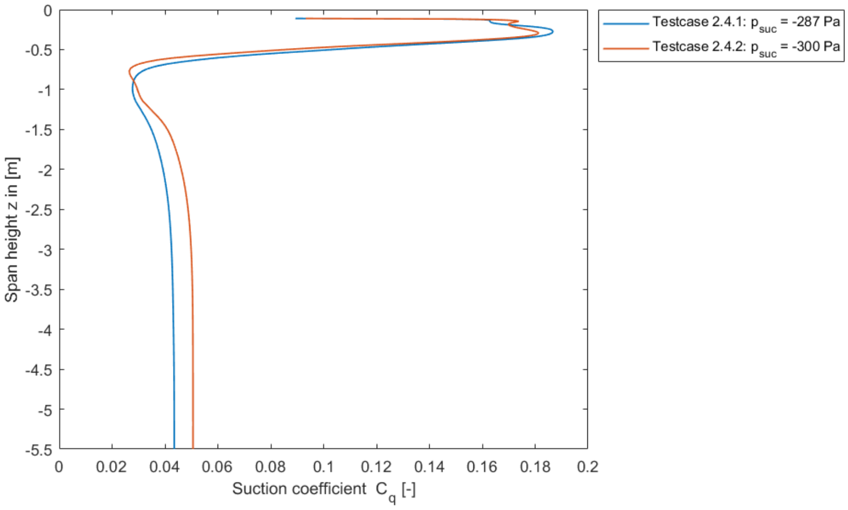

Figure 7.7: Distribution of suction coefficient along span height.

The mass flux of air through the suction region can also be presented as function of the suction coefficient C_q, along the span height. The procedure for calculating C_q is subscribed in section 5.3. The distribution of C_q along the span height for two suction speeds of testcase 2.4.1 and 2.4.2 is given in figure 7.7. On the y-axis, a span height of $z = -5.5m$, corresponds to the bottom. It can be observed that for a suction pressure of $p_{suc} = -287Pa$, the desired suction coefficient of $C_q = 0.047$ has not been reached at the bottom, where the suction coefficient has a value of around $C_q = 0.043$. However, at the top from $-1 < z < 0.08$, the suction coefficient exceeds $C_q = 0.047$. It is expected that the large suction speeds at the top do not contribute in the lift production, since the generated forces at the edge are declining due to a spanwise flow at the outer edge of a foil. The average C_q is therefore regarded as the average value from $-5.5m < z < -2m$, which is denoted with C_{q,ave^*}.

The high suction speed at the top can be prevented by applying a more gradual curved suction pressure at the top, which could be directly controlled by the amount of air mass flux through the suction boundary. The hypothesis is that the overall lift and drag will not largely be affected when the air suction at the top would attain more desirable suction coefficients of around $C_q = 0.047$ for this case. To verify if this hypothesis is true, a more advanced approach would be necessary to model the inner domain of the Turbosail (Turbosail chamber), by modeling one ore more axial fans at the top or bottom. Also other strategies are possible to model the aspiration, such as multiple fans distributed over the total span height. Some applications are presented for example in the Turbosail patent report [16].

In reality, it might be possible that the same phenomena will take place, more air flow is inserted through the top, so that the suction coefficients at the bottom becomes too low. In experiments, it is advised to measure the amount of air mass flux with wind measuring devices and multiple pressure sensors along the span height. By choosing the size of the holes in the suction region properly, the amount of air mass flux can attain the desired values.

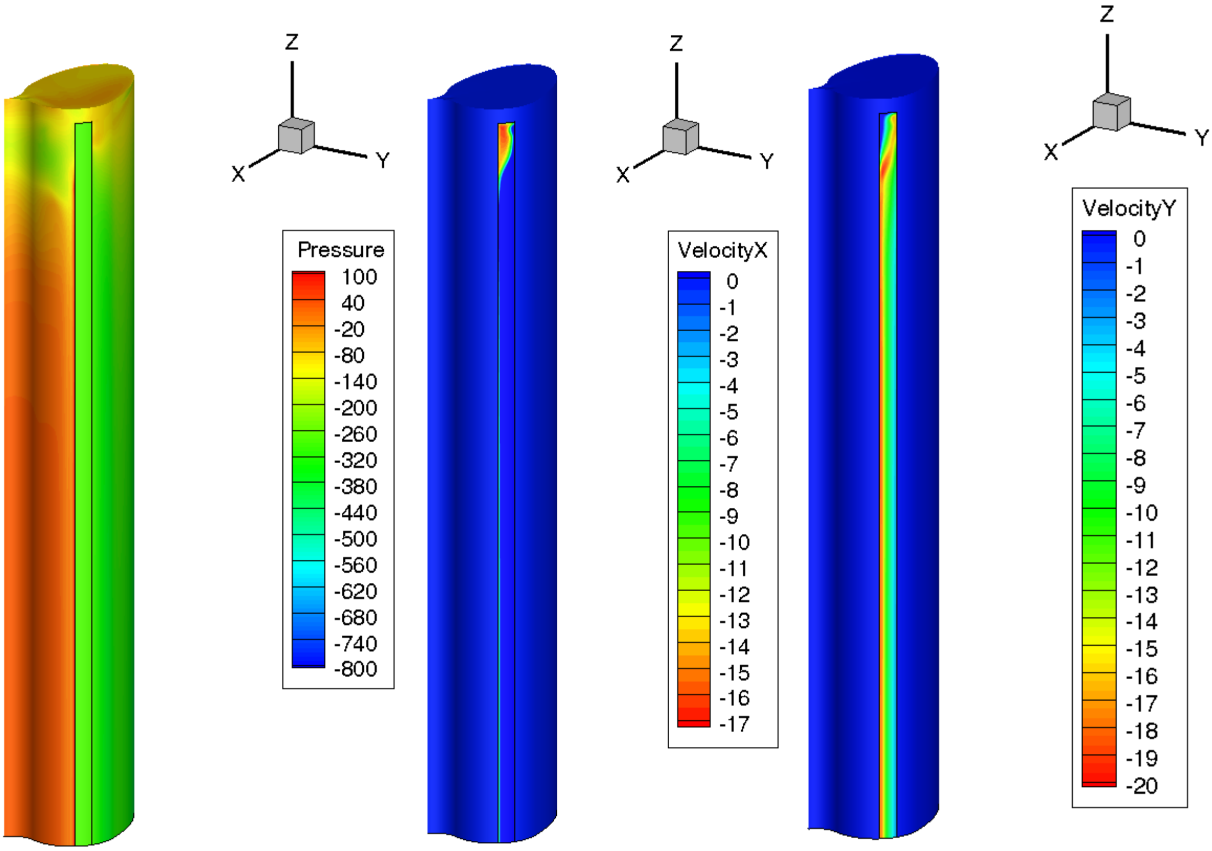

(a) Pressure contour. (b) Velocity in x-direction. (c) Velocity in y-direction.

Figure 7.8: Testcase 2.4.1: pressure and velocity profiles around Turbosail at suction region. The effect of modeling the suction region with a negative pressure, $p_{suc} = -287Pa$ becomes clearly visible in the x and y velocities in the suction region.

7.4.2 Generated Lift and Drag with Aspiration

The pressure contours and streamlines are depicted for testcase 2.4.1 in figure 7.9 for the pressure and suction sides of the foil. From table 7.3, it is shown that the lift and drag reaches values of $C_L = 5.78$

and $C_D = 1.44$ at an average suction coefficient of $C_{q,ave^*} = 0.043$ for testcase 2.4.1. The lower lift and higher drag are a consequence of the decline in lift generation towards the outer edge at the top of the Turbosail. Considering the pressure side at the bottom in figure 7.9a, the minimum pressure at the leading edge in the light blue region reaches a value of $p = -580Pa$ and declines towards the top. In contrast to the analysis for an infinite span in for example testcase 2.1.7 in figure 7.4b, the minimum pressure has much lower value of $p = -780Pa$. At the top, the (relative) pressure is around $p = 0Pa$ and this causes air leakage from the pressure side to the suction side of the foil and vice versa. Particularly at the suction side, this pressure difference causes a large pressure gradient as can be seen in figure 7.4a, reducing the amount of produced lift. This pressure difference at the top induces a so called 'tip vortex', where a spanwise flow can be observed in the wake of the Turbosail, see figure 7.10.

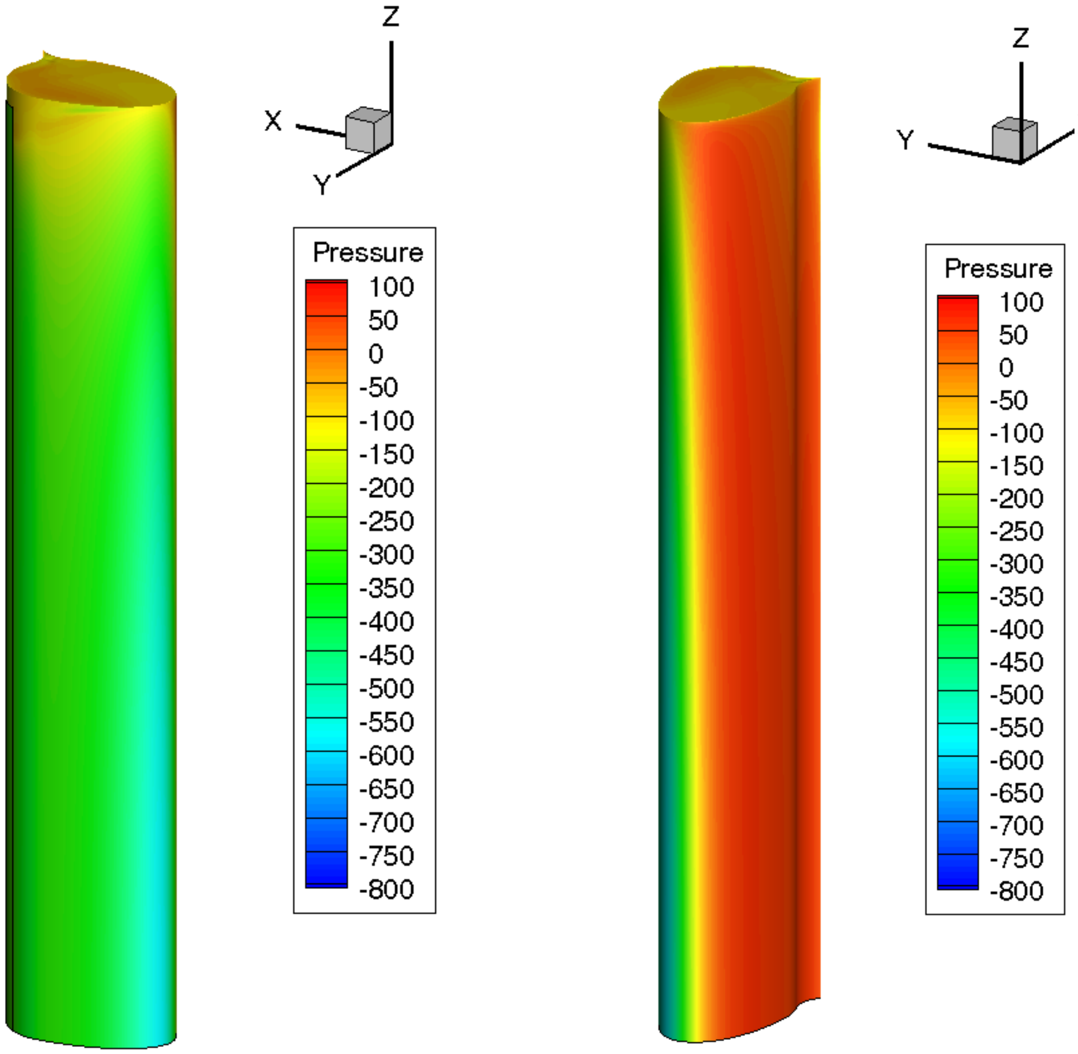

(a) Pressure contour.

(b) Velocity in x-direction.

Figure 7.9: Testcase 2.4.1: pressure and velocity profiles around Turbosail at suction region, to show the effect of modeling the suction region with a negative pressure, $p_{suc} = -287Pa$.

Comparing the lift and drag coefficients for to suction pressures of testcase 2.4.1 and 2.4.2 in table 7.3, it shows that the lift is slightly increased at the cost of a higher drag. The lower suction pressure is responsible for the higher drag, since this pressure force is almost parallel to the flow direction. The suction coefficient is increased from $C_{q,ave^*} = 0.043$ to $C_{q,ave^*} = 0.050$, an increase of 17%. Regarding these results, it is most likely for testcase 2.4.2 that the expenses of increase in drag and aspiration power (to achieve a higher suction coefficient of $C_{q,ave^*} = 0.050$) weight more than the increase of lift.

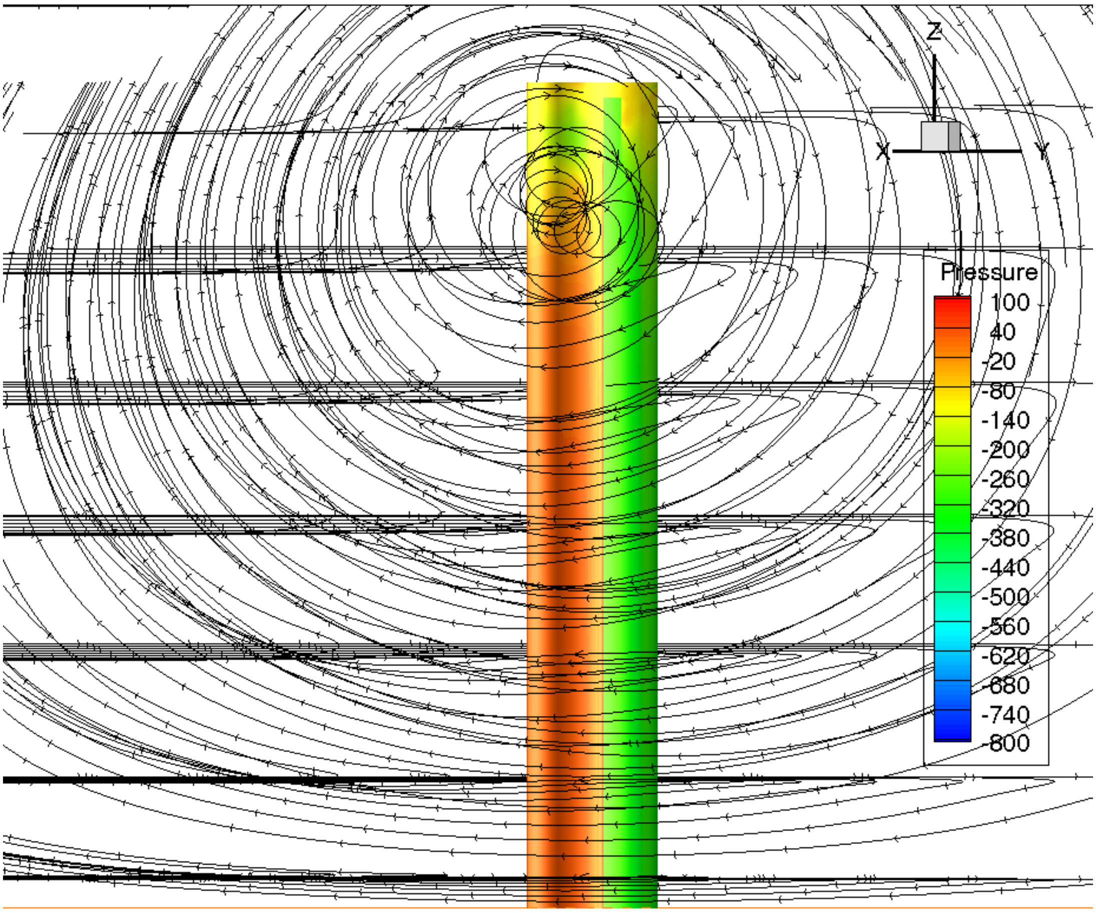

Figure 7.10: Streamlines in the wake of the turbosail with a finite aspect ratio of $A_R = 5.5$.

7.4.3 Lift and Drag without Aspiration

As reference case, the situation with no suction is desired to be known for the finite aspect ratio Turbosail at model scale. Parallel to this project, experiments are conducted and so, it would be the easiest way to validate the CFD results with experiments since the suction behaviour is disregarded. In table 7.3 of testcase 2.4.3, the lift and drag coefficients are calculated with no suction applied. The boundary condition at the suction region are changed into a no slip wall. In contrast to the 2D lift coefficients for infinite span and no applied suction of testcase 1.6.14 ($\alpha = 15°$) in figure 6.15, the lift reduces from $C_{L,2D} = 2.51$ to $C_L = 1.32$ and the drag becomes $C_D = 0.39$ which is obviously low compared to the drag coefficient of testcase 1.6.14. URANS simulations are desired which are expected to give a larger drag coefficient. These expectations are based on the 2D infinite lift and drag coefficients between steady and unsteady RANS computations of testcase 1.4 and 1.6. However, the lower lift coefficient of $C_L = 1.32$ may also result in a lower drag.

Chapter 8

Modified FPP

This chapter starts with a first derivation of Reynolds scaling, to see how these scaling law can be applied to scale forces from model scale to full scale. Subsequently, a method is proposed on how to predict the aspiration power P_a. At last a modified FPP is established which shows the fuel savings of wind-assistance by placing four turbosails.

8.1 Reynolds Scaling

In order to scale forces of a model to full scale, there are a number of similarity laws which have to be fulfilled or at least, should be considered when doing model scale tests. First, the model should comply with geometric similarity, which says that the ratio of length in all three dimensions are equal. The scale factor is expressed as,

$$L_{C,s} = \lambda \cdot L_{C,m} \tag{8.1}$$

Where subscript s, refers to the full scale chord length and subscript m refers to the model chord length. Secondly, kinematic similitude needs to be fulfilled, where both the model and full scale model have correct scale parameters for time and length and thus velocity. This rule always holds when dynamic similarity is fulfilled. At last, dynamic similarity says that the ratio of forces is the same for model and full scale. For a certain case, one is always looking at the dominating forces and tends to apply the dimensionless parameters presenting these dominating forces. In a viscous flow, such as the air flow around the Turbosail, the dominating forces are the friction forces caused by viscosity of the fluid. The dimensionless Reynolds number gives the ratio between inertia forces and viscous friction between air particles in the fluid, that characterizes the flow behaviour.

$$Rn = \frac{UL}{\nu} \tag{8.2}$$

8.1.1 Scaling Rules

Therefore the Reynolds number should be kept constant. In general it is difficult to comply with the scaling laws of Reynolds. However, the Turbosail model is at a scale 1:2, so the required wind velocities only need to be doubled. Reynolds scaling factors are derived in equation 8.3 − 8.6. Both model and full scale should have the same Reynolds number to full fill Reynolds scaling, where subscript s refers to full scale and m refers to model scale.

$$Re_s = Re_m$$

$$\frac{U_s L_s}{\nu} = \frac{U_m L_m}{\nu} \tag{8.3}$$

The kinematic viscosity term disappears and the scale factor λ of equation 8.1 is substituted.

$$U_s = U_m \cdot \frac{1}{\alpha} \tag{8.4}$$

The scaling factor for velocity can thus be derived from equation 8.4, which is $\frac{1}{\alpha}$. For a geometric scaled model, equation 8.1 shows that meters scale with factor α: $m \rightarrow \lambda m$. Further, the product of velocity and time gives a distance, from where the scale factor for time can be derived,

$$[s] = \frac{[m]}{\left[\frac{m}{s}\right]} = \frac{\alpha}{\frac{1}{\alpha}} = \alpha^2 \tag{8.5}$$

Consequently, time scales with $s \rightarrow \alpha^2 s$. Mass in [kg] is directly related to volume, so that the scaling factor is α^3 under the assumption that density is constant. Now, looking at the units from the Newton's second law, it can be derived what scaling factor should be applied in order to scale forces from model to full scale.

$$F = m \cdot a = [kg] \cdot \left[\frac{m}{s^2}\right] = \alpha^3 \cdot \frac{1}{\alpha} \cdot \frac{1}{\alpha^2} = 1 \tag{8.6}$$

From the dimensional analysis in equation 8.6, it can be seen that the scaling factor for forces is 1, so that the measured forces are equal to the force at full scale $F \rightarrow F$ when Reynolds scaling applied.
The suction coefficient needs to be constant to have the same relative suction velocity compared to the upstream velocity of air. The test procedure for a 1:2 model will be presented by the following calculations. In table **??** and **??**, the air suction in $\left[\frac{m^3}{s}\right]$ is presented for a range of wind speeds. As can be seen from table **??**, the measured forces on model scale at $V_{wind} = 20\ m/s$ correspond with the full scale forces at $V_{wind} =\ 10 m/s$, at the same Reynolds number. This calculation shows that forces at model, scale 1:1 with the full scale Turbosail. Cousteau has presented its lift and drag coefficients at a Reynolds number of Re = 130.000, which is equivalent to an apparent wind velocity of $V_{wind} = 2.0\ m/s$ at model scale 1:2. This is a very low wind speed, delivering no significant driving forces. The lift coefficients improve slightly for higher Reynolds numbers. Generally, the lift coefficient increases, as well as the lift drag ratio for higher Reynolds numbers. This effect has a positive effect on the measured results.

8.2 Performance Prediction of Turbosail

When the full scale Turbosail goes into operation, it is essential to predict the required fan power to see how the Turbosail performs with respect to effective power. The effective power of a Turbosail, $P_{E,turbo}$ can be defined as,

$$P_{E,turbo} = F_{X,turbo} \cdot v_s \tag{8.7}$$

where $F_{X,turb}$ is the forward force in the longitudinal axis of the ship of one single Turbosail and v_s is the ship speed. The forward directed force is defined in equation 8.8, using 3.7 and rewriting equation 3.8.

$$F_{x,turbo} = C_{X,turbo} \cdot \frac{1}{2} \rho_{air} U_{AW}^2 S_{turbo} \tag{8.8}$$

Where the thrust coefficient C_X is related to the lift-drag coefficients and the apparent wind angle α_{AW}, as already stated in equation 3.7. The values for C_L and C_D, can be found by the CFD computations of a finite aspect ratio Turbosail in section 7.4.

$$C_{X,turbo} = C_L \cdot sin(\alpha_{AW}) - C_D \cdot cos(\alpha_{AW}) \tag{3.7}$$

To find the reduction in brake power of the engine due to the assistance of Turbosails, the effective Turbosail power $P_{E,turbo}$ needs to be corrected after subtraction of aspiration power and accounting losses due to energy transition of the PTO (power take off). The PTO is coupled to the engine or propeller shaft and converts mechanical energy into electrical energy with an efficiency denoted with η_{PTO}. This electrical power is powers the axial fan in the Turbosail. The effective power of the Turbosail can now be defined in terms of brake power in equation 8.9.

$$P_{B,turbo} = P_{E,turbo} - \frac{P_A}{\eta_{PTO}} \tag{8.9}$$

Typical efficiencies for a PTO are $\eta_{PTO} \approx 0.9$, which are based on shaft generators from MAN Diesel [40].

8.2.1 Estimating Aspiration Power

At last, the aspiration power must be approximated. For a full scale model, a specific fan of typ AXC-1000 is to be selected for aspiration to attain suction speeds of maximum $C_q = 0.047$. This fan has a inner diameter of $\phi_{DI} = 1000mm$ and the maximum dimensions $T = 1288mm$ are given in figure fig:DimensionsAXC1000 of Appendix E, and should fit within the dimension of the Turbosail.

The power diagram of the AXC-1000 is depicted in figure **??** in Appendix E, and shows that the power is dependent on the angle of the fan blades $\phi_{FanBlades}$, pressure difference between inlet and outlet (equivalent to the suction pressure p_{suc}) in the Turbosail chamber) and the desired mass flow, Q. The temperature in the diagram corresponds to $T = 20C^{\circ}$, which is close to the temperature used in the FPP of $T = 15C^{\circ}$. In the product specification it is described that the fan can be controlled with a frequency controller. Without having experience with characteristics of this fan, it is assumed that working point from the power diagram scales linearly with the frequency controller to calculate other mass flows for a constant angle setting of the fan blades. This assumption is based on similar behaviour of the blade angles in a specific range. It can be seen from the P-Q curve and p-Q curves in figure 8.1 and 8.2 that the linear steepness, which can be quantified with a derivative $\Delta P/\Delta Q$ and $\Delta p/\Delta Q$ relationship, is by approximation similar for a range of blade angles between $\phi_{FanBlades} = [10^{\circ} - 20^{\circ}]$.

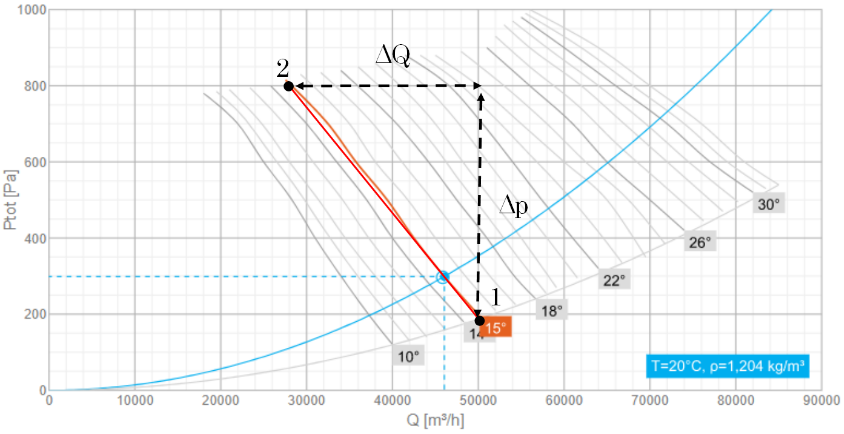

Figure 8.1: Relation between suction pressure p_{suc} and air mass flow Q for the axial fan AXC-1000.

In the FPP, this assumption makes it easy to calculate the aspiration power as function of apparent wind speed U_{AW} and suction pressure p_{suc}. In the following, the procedure is described on how to estimate the aspiration power of the fan.

1. Estimate the suction pressure p_{suc}. The suction pressure p_{suc} is estimated in equation 8.10 and 8.11 from numerical analysis of the 2D steady RANS computation resembling testcase 1.4.7 and 1.4.13 for the suction coefficients of $C_q = 0.047$ and $C_q = 0.032$ respectively.

$$C_{p,Cq=0.047} = \frac{p_{suc}}{\frac{1}{2}\rho_{air}U_{AW}^2} = \frac{-287}{\frac{1}{2}\cdot 1.225 \cdot 10^2} = 4.69 \tag{8.10}$$

$$C_{p,Cq=0.032} = \frac{p_{suc}}{\frac{1}{2}\rho_{air}U_{AW}^2} = \frac{-235}{\frac{1}{2}\cdot 1.225 \cdot 10^2} = 3.84 \tag{8.11}$$

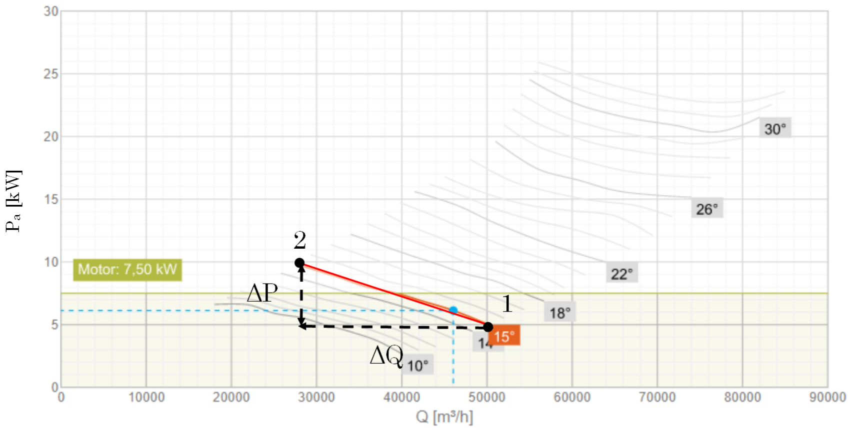

Figure 8.2: Relation between aspiration power P_a and air mass flow Q for the axial fan AXC-1000.

To calculate the suction pressure for every apparent wind speed U_{AW} and a constant C_q, the dimensionless pressure C_p of equation 8.10 or 8.11 can used to calculate the suction pressure for different apparent wind speeds.

2. Calculate the amount of mass flow for a specific C_q in equation 8.12 rewriting equation 2.7.

$$Q = C_q \cdot U_{AW} \cdot S \cdot 3600 \quad \text{in } [m^3/h] \tag{8.12}$$

3. For a constant p_{suc}, calculate working point of the fan with respect to mass flow Q, and aspiration power P_a. In the FPP, it is assumed that the angle of the blades is set at a constant angle 15°, so that the aspiration power is a function of mass flow, suction pressure and apparent wind speed, $P_a = f(Q, p_{usc}, U_{AW})$. For a constant angle of the fan blades $\phi_{FanBlades}$, the power diagram in figure **??** shows a somewhat linear relation between mass flow Q, and suction pressure p_{suc} for two working points 1 and 2 in table 8.1.

Table 8.1: My caption

Working point	**Q in** $[m^3/h]$	p_{suc} **in [Pa]**	P_a in [kW]
1	50000	180	5
2	28000	820	10

Two linear equations can be set up to calculate the working point for the fan, $P_{a,WP}$ and Q_{wp}, where subsript WP refers to working point.

$$P_{a,WP} = \frac{\Delta P}{\Delta p} \cdot p_{suc} + P_0 \tag{8.13}$$

$$Q_{WP} = \frac{\Delta Q}{\Delta p} \cdot p_{suc} + Q_0 \tag{8.14}$$

4. At last, the aspiration power can be computed in equation 8.15 for the desired mass flow Q, calculated in step 2 in equation 8.12. It is assumed that other mass flows Q can be realized by a frequency controller to control the RPM of the fan, using the same dP/dQ ratio.

$$P_a = \frac{P_{a,WP}}{Q_{WP}} \cdot Q \tag{8.15}$$

8.3 Modified Fuel Prediction Program

At last, as a final result, an answer can be given on the research question 1, in section 1.4, how large are the fuel savings for a general cargo ship of 4500 DWT by installing four Turbosails on deck for multiple wind speeds visualized in a polar diagram for all 360 degrees round true wind angles? This section discusses the modified FPP and concludes how large are the fuel savings having wind-assistance of four Turbosails on the ship.

The Turbosail fan power or aspiration power P_a, is determined in section 8.2 and can now be implemented in the FPP polar diagram to examine how the aspiration power reduces the gains of the Turbosail. Also to improve the accuracy of the FPP, the Turbosail forces are based on the numerical result of the 3D RANS finite aspect ratio of testcase 2.4.1 in section 7.4. It was found that the lift and drag where $C_L = 5.78$ and $C_D = 1.44$ with an approximated average suction coefficient of $C_{q,ave^*} = 0.043$. It must be noted, however, that the interaction between multiple Turbosails and the superstructure will definitely have impact on the produced lift, this should be further analysed by a numerical study or from real force monitoring of the full scale Turbosails in operation. In the FPP presented in this model, it is assumed that interaction between Turbosails are nor positive nor negative so that the interaction coefficient accounting for this effect is set to $C_{turbo} = 1$, see equation 3.8.

$$F_{x,wcu} = C_{X,turbo} \cdot \frac{1}{2}\rho_{air} U_{AW}^2 S_{turbo} \cdot n_{turbo} \cdot C_{turbo} \tag{3.8}$$

The effect of new lift-drag coefficients and aspiration power P_a, has been depicted in the modified polar plot in figure 8.3. This polar plot shows three ratios for each wind speed of 6,10 and 14 m/s. These ratio are:

- $\frac{P_{B,1}}{P_{B,0}}$, brake power for the propeller with WASP, $P_{B,1}$ relative to brake power for propeller without WASP, $P_{B,0}$.
- $\frac{P_{B,2}}{P_{B,0}}$, brake power for the propeller and aspiration power with WASP, $P_{B,2}$, relative to brake power for propeller without WASP, $P_{B,0}$.
- $\frac{FC_2}{FC_0}$, Fuel consumption due to brake power of propeller and fan, FC_2, relative to the fuel consumption based on the brake power without WASP, FC_0.

Correctly speaking, the FPP in figure 8.3 consists despite fuel consumption also brake power, so in this sense the FPP is also PPP (Power Prediction Program). However, in this section the term FPP is used for the polar plot.

The contribution of aspiration power to the total brake power becomes obviously clear from the FPP in figure 8.3. For a wind speed of $V_{wind} = 14m/s$ and a true wind angle of $TWA = 36°$, the fuel reduction is 0%, whereas the brake power for the propeller was reduced to 81%. The other 19% of brake power is reserved for the aspiration power needed to achieve the desired lift-drag forces of the Turbosail. The high requirement of suction power is due a higher air mass flow Q and a lower suction pressure p_{suc}, and is caused by the higher apparent wind speed. In head wind headings (or small true wind angles) of the ship, the apparent wind speed increases as a result of the summation of true wind speed and ship speed. To remain a constant suction coefficient C_q, the amount of air mass flux Q, must increase and also the suction pressure in the Turbosail champer reaches a lower minimum.
Based on the assumptions made in this FPP, it can be concluded that for a wind speed of $V_{wind} = 14m/s$, the ship starts to reduce its fuel consumption for true wind angles larger than $TWA > 36°$. The ratio for brake power (with and without aspiration power) and fuel consumption are given in table 8.2 for a range of TWA at $V_{wind} = 14$m/s and correspond to the values in the FPP of figure 8.3.

Table 8.2: Ratios of brake power and fuel consumption based on the FPP in figure 8.3 for an wind speed of $V_{wind} = 14m/s$.

TWA	**36**	**60**	**90**	**120**	**150**	**180**
$\frac{P_{B,1}}{P_{B,0}}$	0.84	0.57	0.47	0.55	0.74	0.94
$\frac{P_{B,2}}{P_{B,0}}$	1.00	0.70	0.53	0.58	0.76	0.96
$\frac{FC_2}{FC_0}$	1.00	0.75	0.61	0.65	0.81	0.97

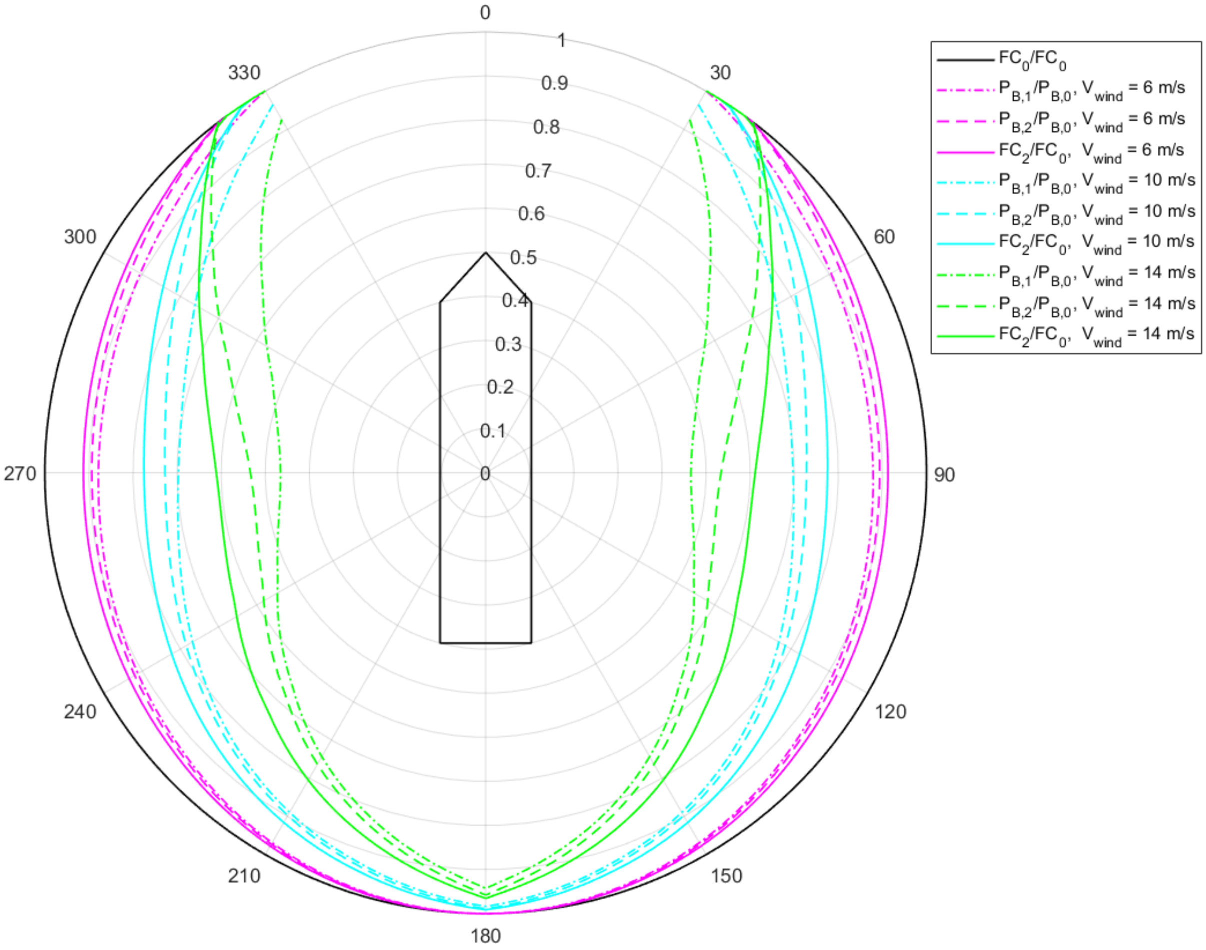

Figure 8.3: Modified FPP showing the reduction in brake power of propeller and/or fan and total fuel consumption using WASP as a ratio the original case without WASP.

It can be seen that the portion of aspiration power, denoted by $\frac{P_{B,2}}{P_{B,0}} - \frac{P_{B,1}}{P_{B,0}}$, is the highest for small TWA or upwind headings and reduces when TWA increases, thus for the more downwind headings. Regarding the most ideal coarse at $TWA = 90$ and $V_{wind} = 14m/s$ in table 8.2, the reduced brake power for the propeller is 58% $(1 - 0.42) \cdot 100\%)$. After accounting for aspiration power P_a, the final reduced brake power for propeller and fan becomes 51%. The less ideal specific fuel consumption, discussed in section 3.4 reduces the benefit from Turbosails even further. The final reduction of fuel is 43% compared to the case where no wind-assistance is applied. When the ratio of brake power of the propeller $P_{B,1}/P_{B,0}$ becomes less (for larger TWA), the relative losses due to aspiration power and more favourable SFOC for fuel consumption become less. The average fuel savings for three different wind speeds are calculated for the entire polar diagram, thus for 360 degrees round headings. For a true wind speed, V_{wind} of 6m/s, 10m/s and 14m/s, the average reduction in fuel consumption becomes 3.9%, 11% and 20% respectively.

8.3.1 Reducing Aspiration Power

From the polar diagram of the FFP in figure 8.3, it was shown that the aspiration power has a large contribution in particular upwind headings. The effect of reducing aspiration power could therefore improve the benefit from the Turbosails, despite the lower propulsive force of wind-assistance. Consequently, the reduced suction coefficient of $C_q = 0.032$ would be interesting to compare with the higher suction coefficient of $C_q = 0.047$ in the FPP. Although the lift and drag coefficients have not been calculated for a suction coefficient of $C_q = 0.032$ for an aspect ratio of A_R=5.5, a prediction of C_L and C_D for $C_q = 0.032$ can be made based on the 2D lift coefficients for infinite span and the finite aspect ratio Turbosail. Considering the SRANS SST calculation of testcase 1.4.7 ($C_q = 0.047$, $C_L = 7.97$) and testcase 1.4.10 ($C_q = 0.032$, $C_L = 6.8$), the reduction in lift is 14.7% while the suction coefficient lowers with 31.9%. Also the suction pressure becomes less with 18.1%. The lift coefficient for $C_q = 0.032$ becomes $C_L = 4.93$ and is estimated by reducing C_L for a finite aspect ratio of A_R=5.5 of testcase 2.4.1 with 14.7%. The drag coefficient is assumed to have the same value as the drag calculated for the finite aspect ratio of $C_D = 1.44$ of testcase 2.4.1. This is a safe assumption, since it is expected that the drag could be lower. Hence, the approximation formula of Prandtl for a finite wing says that the drag can be related to the lift coefficient, see equation 8.16.

$$C_D = \frac{C_L^2}{\pi A_{R,e}} \tag{8.16}$$

Where $A_{R,e}$ is the effective aspect ratio.

From section 8.2.1, it is described how to estimate the aspiration power for a certain C_q.
The ratio for fuel consumption FC_2/FC_0 and brake power $P_{B,2}/P_{B,0}$ are depicted for two suction coefficients in the FPP of figure 8.4, to show how a variation in aspiration intensity of the fan can improve the performance of a ship with Turbosails.

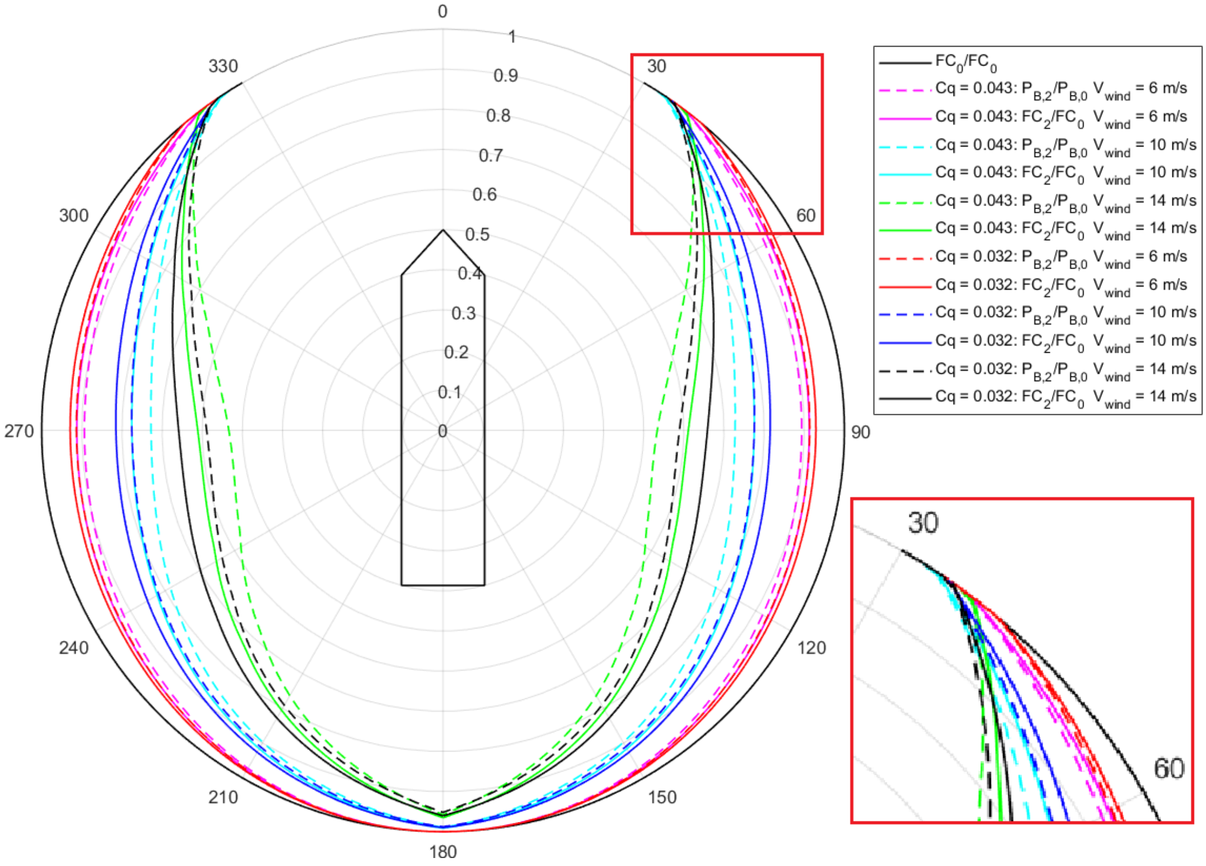

Figure 8.4: Comparison of two suction coefficients C_q of the Turbosails on the fuel consumption of the ship.

From figure 8.4, the reduction of aspiration power to operate at a lower suction coefficient of $C_q = 0.032$, has only an advantage of 1-2% for upwind coarses between $34° < TWA < 43°$. For $TWA > 43°$, a larger suction coefficient of $C_q = 0.043$ magnifies the fuel savings due to the higher lift force of the Turbosails.

Chapter 9

Conclusions & Recommendations

This chapter gives final conclusions regarding the performance of a ship which uses wind-assisted propulsion by placing four Turbosails on deck, as is defined in main research question in section 1.4. In the definition stage, an initial FPP is set up based on the available literature. The main points are concluded in section 9.1.1. The initial FPP excludes aspiration power, which turned out to be an important aspect to include in the FPP. Also the extraordinary high lift coefficients were doubted, and therefore a extensive CFD model is set up to verify the lift and drag coefficients. The working mechanism of a Turbosail is now better understood by conducting CFD computations for infinite and finite aspect ratio Turbosails. The effect of two aspiration speeds of the axial fan, which can be translated to suction coefficients C_q, are investigated for infinite span Turbosail discussed in section 9.1.2. Conclusions for the lift-drag coefficients of an finite aspect ratio Turbosail are given in section 9.1.4. With a proposed method to determine the aspiration power and the new lift-drag coefficients of the finite aspect ratio Turbosail, the FPP is modified and concludes what are the fuel saving of a ship with WASP in section 9.1.5. In section 9.2, recommendations for future work are given.

9.1 Conclusions

9.1.1 Definition Stage

In the definition stage, first conclusions are drawn in section 3.5. The main points are summarized from this section. It is concluded that for a reliable performance prediction of a ship with wind-assistance, an accurate relation between hydrodynamic side forces of the hull is desired. The rudder forces in the FPP are based on coefficients of Kornev, however, this model does not account for stall and for a specific shape of the rudder. The rudder forces can become dominant in added resistance due to the balance of side forces of the Turbosail. Consequently, the rudder deserves more attention for an improved FPP. Considering the importance of yaw ballance and force balance in side way direction (y-direction), the side forces due to the superstructure should be included in an improved FPP model. Also there should be accounted for the interaction effects between a number Turbosails and the superstructure, that may effect the lift and drag coefficients of each individual Turbosail.

Regarding the propeller efficiency η_p, the benefit with wind-assistance can further be improved with the use of CP-propellers. In the current engine configuration of the ship, the shaft RPM could only be reduced with 10%, but when reducing the shaft RPM even further, there is a potential to gain higher propeller efficiencies at about $\eta_P \approx 0.7$.

9.1.2 Lift-drag Coefficients for Infinite Span of 2D SRANS and URANS

The domain size of the grid showed to be an important parameter for the magnitude of the drag coefficient in testcase 1.1. It is found that the pressure field around the Turbosail effects the streamlines of the flow. A larger radii of the computational domain lowers the drag and increases the lift.

In testcase 1.4 and 1.6 the steady and unsteady RANS equations with the the $k-\omega$ SST turbulence model are selected for a 2-dimensional flow to obtain lift and drag coefficients for an infinite span Turbosail. The difference between SRANS and URANS appeared to be small for the generated lift coefficient, especially for larger angles of attack α. URANS showed that vortex shedding is present in the wake of the foil and these vortexes cause more pressure fluctuations leading to a lower average pressure in the wake of the foil. As a result, URANS showed a higher drag compared to SRANS simulations. The experimental results from Cousteau [1] for lift showed to be in close agreement to the numerical computations, although the stall point occurs at $\alpha = 32°$, while the URANS expects that stall occurs between $35° < \alpha < 40°$, for $C_q = 0.047$. Also for a lower suction coefficient difference in stall point are observed.

9.1.3 Comparison of Turbulence Models for Infinite Lift-drag Coefficients Using 3D SRANS SST and SRANS EARSM

A more physical three dimensional model is set up by expanding the number of cells in span direction for calculating lift and drag for infinite span Turbosail. 3D steady RANS computations are conducted in testcase 2.1 - 2.3 for the $k-\omega$ SST and EARSM turbulence models. The influence of a 3 dimensional flow appeared to be very small when the SST turbulence model is selected. The z-velocities in the wake showed a maximum of $U_z = 0.0005 \cdot U_\infty$, or 0.05% compared to the free stream velocity U_∞. The lift and drag were hardly influenced by adding more cells in z-direction. The more anisotropic EARSM turbulence model, showed to have a larger 3-dimensional effect on the flow. In the wake, the z-velocities attain values about maximum 10% relative to the freestream velocity. However, the effect on the lift and drag again, appeared to be small. Based on these results, it can be concluded that 2D computations for infinite span shows similar results as 3 dimensional computational domain for infinite span with $k-\omega$ SST or EARSM turbulence model.

9.1.4 Lift-drag Coefficients of Finite Turbosail with A_R=5.5

The finite aspect ratio Turbosail of $A_R = 5.5$ showed a reduction in lift and an increase in drag which is due to tip vortices at the free end of the Turbosail. Two suction pressures p_{suc} were applied which lead to suction coefficients close to the desired suction coefficient of $C_q = 0.047$ over a large range of the suction region along the span height. At the top however, the subjected pressure boundary condition leads to very high suction velocities. It is expected that a smooth reduction of this suction pressure reduces the suction speed at the top, at small costs of a lower lift, in section 9.2 recommendations are given how model the suction behaviour for an improved model. The lift and drag become respectively $C_L = 5.78$ and $C_D = 1.44$ for an average suction coefficient of $C_q = 0.043$.

9.1.5 Modified Fuel Prediction Program

When the Turbosail is placed on the ship, the performance of the Turbosail can be determined. The aspiration power is approximated by selecting a specific fan with maximum diameter and considering the relation between suction pressure, air mass flow and electrical power. The FPP is modified with the new lift-drag coefficients from the finite aspect ratio numerical analysis and by calculating the amount of electrical power. At last, the electrical power is added to the brake power accounting for mechanical losses and the final fuel consumption is computed for the FPP. This polar plot answers research question 1: the fuel savings that can be realized by placing four Turbosails on deck of each 5.5m lead to an average reduction in fuel of 4%, 10% and 20% for wind speeds of 6m/s, 10m/s and 14m/s respectively.

9.2 Recommendations

9.2.1 Fuel Prediction Program

The definition stage raises a number of questions regarding the FPP, which needs to be further investigated. This addresses the following remarks.

- The hydrodynamic side force of the hull and induced resistance due to leeway is an important parameter for the performance of motor-sailing ship. These hydrodynamic forces can be analysed by CFD or from experiments. However, another method can be to monitor all important relevant parameters on a real vessel and determine the hydrodynamic coefficients from practice.
- The rudder forces require an improved rudder model. A maximum rudder angle should be adopted which sets a restriction for the maximum side forces produced by the Turbosails.

- The FPP introduced in this thesis uses the open water diagram for a fixed propeller of the Wageningen B-series and should be replaced by the correct open water diagram of a CP-propeller. It should be analysed if the same conclusion can be drawn, that high propeller efficiencies can be realized by reducing the shaft RPM.
- From Schuiling [6] in section 2.8.1, it was found that the oblique inflow at the propeller plane effects the propeller efficiency. This topic receives more attention, when an accurate FPP is desired.
- When the ship is sailing under low engine power, maintenance costs of the engine may increase due to pollution of the turbine nozzle ring. For this shipowner, these cost lower the benefit from wind-assistance and is a point of consideration.
- It should be examined if the gearbox and shaft efficiency remain constant for other engine loads.
- Stability criteria with wind-assistance affect safety of a ship. It should be investigated if a ship with WASP complies with classification rules. The maximum heel angle can be a restriction for the crew on a ship. The stability criteria can be included in a FPP, to see when the dangerous situations occur.
- To determine the profit realized by wind-assistance, the fuel savings should be calculated for a ship and its operational profile. Weather routing may then improve the net benefit by choosing better routes based on the current weather conditions.

9.2.2 Turbosail

A number of recommendations can be made regarding the numerical study on a Turbosail with CFD.

- The used pressure boundary condition at the suction region of the Turbosail suffices as a first method to realize the boundary layer suction. However, for an improved model of the Turbosail with finite or infinite span, modeling of the inner domain of the Turbosail chamber is advised such that a axial fan is modelled with a specified mass flow at the top or bottom. Chamber modelling would give a more realistic suction behaviour. Possibly, other concluding remarks can be drawn regarding the aspiration power, that can be estimated with more confidence.
- Another way is to approximate the velocity field at with experiments, measuring the mass flow at different location across the Turbosail span, which can then be implemented as a boundary condition at the suction side. By defining a velocity field at the suction boundary, it is very easy to control aspirated flow, just by defining the suction speed and requires no iterations in contrast to a pressure boundary condition.
- A refinement study of the finite Turbosail in section 7.4 is desired to be conducted. However, modelling of the suction boundary condition should be revised. For example by the proposed methods described in the previous points, thus by modelling of the inner domain or a certain prescribed velocity profile.
- Expand the CFD model, to a case where the superstructure of the ship is modelled including a number of Turbosails. The interaction between multiple Turbosail on deck and the superstructure can be analysed by CFD to find the best location for the Turbosail with respect to the lift and drag forces. However, final performance of all Turbosails combined in a FPP, depends in a large extent also to the hydrodynamic side force and induced drift resistance of the hull + appendages. The choice for placement of several Turbosails should be chosen carefully in order to have a optimal performance.
- A more accurate and computational demanding scale resolved simulation (SRS) model would be recommended for example with DDES or LES to confirm if a simple 2D model is sufficient to calculate the lift and drag for aspirated profiles. Based on the outcome of a SRS model, a simple 2D model using steady or unsteady RANS may be sufficient to analyse other Turbosail geometries to find even better lift-drag characteristics.

Bibliography

[1] Charrier, B., Constans, J., Cousteau, J.Y., Daif, A., Malavard, L., Quinio, J.: Foundation Cousteau and Windship Propulsion, Wind Engineering and Industrial Aerodynamics, 20 (1985) page 39-60. *Elsevier Science Publishers*

[2] Fujiwara T., Hearn G.E., Kitamura F., Ueno M., Minami Y.: Steady Sailing Performance of a Hybrid-sail Assisted Bulk Carrier *Journal of Marine Science and Technology*

[3] Eggers R.: Operational Performance of Wind Assisted Ships *10th Symposium on High-Performance Marine Vehicles HIPER'16, October 2016*

[4] Dijkman, M.A.: Een haalbaarheidsstudie naar twee stand alone Wind Conversion Units, NHL Hoogeschool, Scheepsbouwkunde te Leeuwarden, june 2014

[5] van Tuijl, J.J.: Evaluation of Auxililiary Wind Propulsion Systems for Merchant Ships *ADEPT Report, 2012*

[6] Schuiling, B.: Effect of a Drift Angle on Propulsion Performance *Marin report No. 70033-1-RD, 2016*

[7] Viola I.M., Sacher S., Jinsong X., Wang F.: A numberical method for the design of ships with wind-assisted propulsion *Elsevier Science Publishers, Ocean Engineering 105(2015)33–42*

[8] Settels J.W.: Hydrodynamic Forces on Wind Assisted Ships using CFD *Delft University of Technology*

[9] Van der Kolk N.J.: Hydrodynamics of Wind-Assisted Propulsion: Modeling of Hydrodynamic Sideforce *Delft University of Technology*

[10] Kijima K., Katsuno T., Nakiri Y., Furukawa Y.: On the manoeuvring performance of a ship with the parameter of loading condition *Society of Naval Architects of Japan*

[11] Kramer J.A., Steen S., Savio L.: Experimental study of the effect of drift angle on a ship-lke foil with varying aspect ratio and bottom edge shape *Ocean Engineering 121 (2016) 530-545*

[12] Ankudinov V., et al: Ship Maneuvrability Assessment in Ship-Design-Simulation Concept *International Ship Maneuvering Conference, London, May 1987*

[13] Panel H-10 (Ship Controllability) of SNAME: Design Workbook on Ship Maneuverabilty *The Society of Naval Architecture and Marine Engineering (SNAME), Technical and Research Bulletin 1-44, 1993*

[14] Kornev H.N.: Lectures on Ship Manoeuvrability *Faculty of Mechanical Engineering and Marine Technology Chair of Modeling and Simulation, University Rostock, 2013*

[15] Conoship report: 'Wind Conversie Unit' Een verplaatsbare en instelbare windgedreven (hulp)voorstuwinsunit voor zeeschepen *2011*

[16] Cousteau J.Y., Malavard L., Charrier B.: USA Patent,'Apparatus for producing a force when a moving fluid' *1986*

[17] Hcini C., Abidi E., Kamoun B., Afungchui D.: A Turbosail profile analysis code based on the panel method *Energy volume 118, 2017*

[18] Klein Woud H., Stapersma D.: Design of Propulsion and Electric Power Generation Systems *Institue of Marine Engineering, Science and Technology, 2002*

[19] International Standard: Ships and marine technology - Guidlines for the assesment of speed and power performance by analysis of speed trial data *ISO 15016, 2002*

[20] Larsson L., Raven H.C.: The Principles of Naval Architecture Series *The society of Naval Architects and Marine Engineers, 2010*

[21] Feriziger J.H., Peric M.: Computational Methods for Fluid Dynamics *Springer-Verlag Berlin Heidelberg New York, 2002*

[22] Peyro G.: Analysis of flows on Stabilizer Fins using ReFRESCO: 2D, 3D, Static and Dynamic Effects *MARIN & ENSTA Bretagne, 2011*

[23] Eça L., Hoekstra M.: A procedure for the estimation of the numerical uncertainty of CFD calculations based on grid refinement studies *Elsevier, Journal of Computation Physics, 2014*

[24] de Jong P., Katgert M., Keuning L.: The Development of a velocity prediction Program for Traditional Dutch Sailing Vessels of the Type Skutsje *Hiswa Symposium, 2008*

[25] Lutton M.J.: Comparison of C- and O-Grid Generation Methods Using a NACA 0012 Airfoil *Air Force Institute of Technology, 1990*

[26] Hickel S.: Lecture slides from course: CFD for Aerospace Engineers *CourseID: AE4202, Technical University Delft, 2017*

[27] Jung J.H, Kim M.J., Yoon H.S., Hung P.A., Chung H.H., Park D.W.: Endplate effect on aerodynamic characteristics of three-dimensional wings in close free surface proximity *International Journal of Naval Architecture and Ocean Engineering, 2012*

[28] Schlichting H., Gersten K.: Boundary Layer Theory, chapter 2 *Springer-Verlag Berlin Heidelberg, 2017*

[29] Schlichting H., Boundary Layer Theory *Mc Graw Hill Book Company 7th edition, 1979*

[30] Langtry R.B., Menter F.R.: Correlation-Based Transition Modeling for Unstructured Parallelized Computational Fluid Dynamics. *AIAA Journal Vol. 47, No. 12, December 2009*

[31] E ça L., Lopes R., Vaz G., Baltazar J., Rijpkema D.: Validation Exercises of Mathematical Models for the Prediction of Transitional Flows *31st Symposium on Naval Hydrodynamics Monterey, CA, 11-16 september 2016*

[32] Menter F.R., Kuntz M., Langtry R.: Ten Years of Industrial Experience with the SST Turbulence Model *Turbulence, Heat and Mass Transfer 4, Begell House 2003*

[33] Schuttevaer: Zwaarste Jaar Ooit voor Scheepsbouw, URL: *https://www.schuttevaer.nl/nieuws/scheepsbouw-en-reparatie/nid24909-zwaarste-jaar-ooit-voor-scheepsbouw.html 22 June 2016*

[34] Knoop B. Lalkens P.: Nederlandse Zeevaart in Heftigste Crisis Ooit,URL: *https://fd.nl/ondernemen/1172025/nederlandse-zeevaart-in-heftigste-crisis-ooit 21 October 2016*

[35] Notenboom B.: URL: *https://decorrespondent.nl/4343/vaar-mee-op-de-esperanza-en-leer-de-ongekend-vervuilende-scheepvaart-kennen/1161197290880-1bfce49f 16 April 2016*

[36] Bazari Z.: IMO TTT Course on Energy Efficient Ship Operation, Module 2 - Ship Energy Efficiency Regulations and Related Guidelines *International Maritime Organisation, London, Januari 2016*

[37] Holtrop J., Mennen G.G.J.: An approximate power prediction method *International Shipbuilding-Progress 29 (335), 166-170, 1982*

[38] MARIN: ReFRESCO description, URL: http://www.refresco.org/resources/overview-2/ *ReFRESCO version 2.3.0, Januari 2017*

[39] Klein Woud H., Stapersma D.: Design of Propulsion and Electric Power Generation Systems *Institute Of Marine Engineers, October 2002*

[40] MAN Diesel & Turbo Shaft Generators for Low Speed Main Engines URL: http://marine.man.eu/docs/librariesprovider6/technical-papers/shaft-generators-for-mc-and-me-engines.pdf?sfvrsn=38 *MAN DIESEL & Turbo, Copenhagen, Publication no.: 5510-0136, Aug 2012*

[41] Kok J.C., Resolving the depence on freestream values for the $k - \omega$ turbulence model *Am. Inst. Aeronaut. Astronaut. (AIAA) J. 38 (7), 1292-1295*

[42] Dol H.S., Kok J.C., Oskam B.: Turbulence Modeling for Leading-Edge Vortex Flows. *In: Proceedings of the 40th Aerospace Sciences Meeting and Exhibit, American Institute of Aeronautics and Astronautics (AIAA).*

[43] Wallin S., Johansson A.V.: An Explicit Algebraic Reynolds Stress Model for Incompressible Turbulent Flows *Fluid Mechanics 403, 89-132*

[44] Brouwer J., Tukker J., van Rijsbergen M.: Uncertainty Analysis and Stationarity Test of Finite Length Time Series Signals *AMT'15 ,September 2015*

[45] Brouwer J., Tukker J., van Rijsbergen M.: Uncertainty Analysis of Finite Length Measurement Signals *3rd International Conference on Advanced Model Measurement Technology for the EU Maritime Industry (AMT), Gdansk Poland, September 2013*

Appendix A

Vessel dimensions

Table A.1: **Main characteristics reference vessel**

Lpp	84.94	m
B	14.40	m
depth	7.85	m
T (fully loaded)	5.80	m
Cb	0.812	-
Cm	0.998	-
Displacement	5960	Ton
Deadweight	4510 (approx)	ton

Appendix B

Fuel Prediction Program

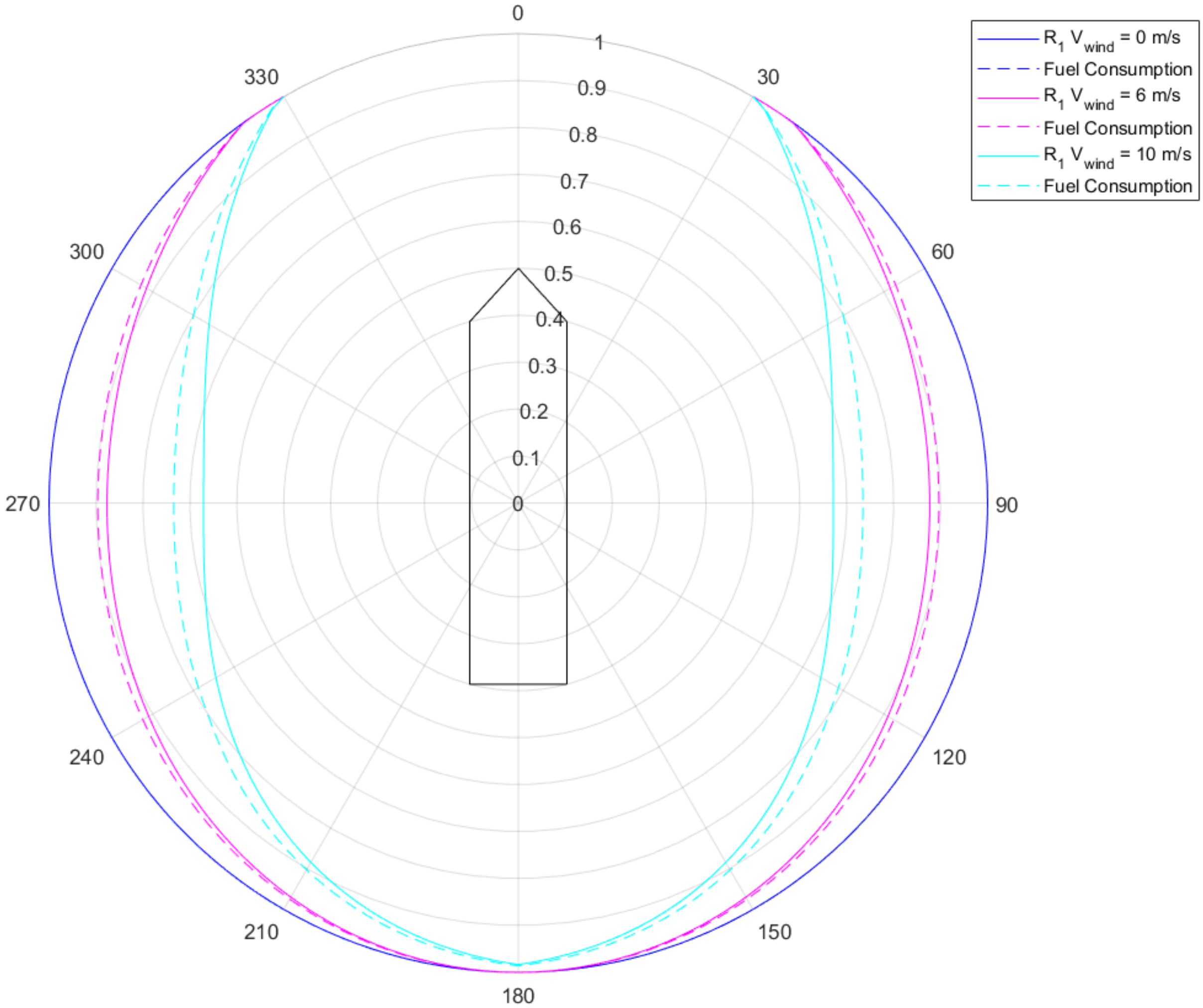

Figure B.1: FPP at a ship speed of $v_s = 11.5$ kts and engine speed of $n_e = 750$ RPM

Table B.1: $v_s = 11.5kts$, $n_e = 750$ RPM, TWA $= 90$ °, $R_0 = 109kN$

V_{wind}	R_1/R_0	η_D	SFOC [g/kWh]	FC_1/FC_0	FC[ton/h]
0	1	0.546	192.07	1	0.198
6	0.877	0.546	196.25	0.896	0.178
10	0.671	0.534	205.57	0.735	0.146

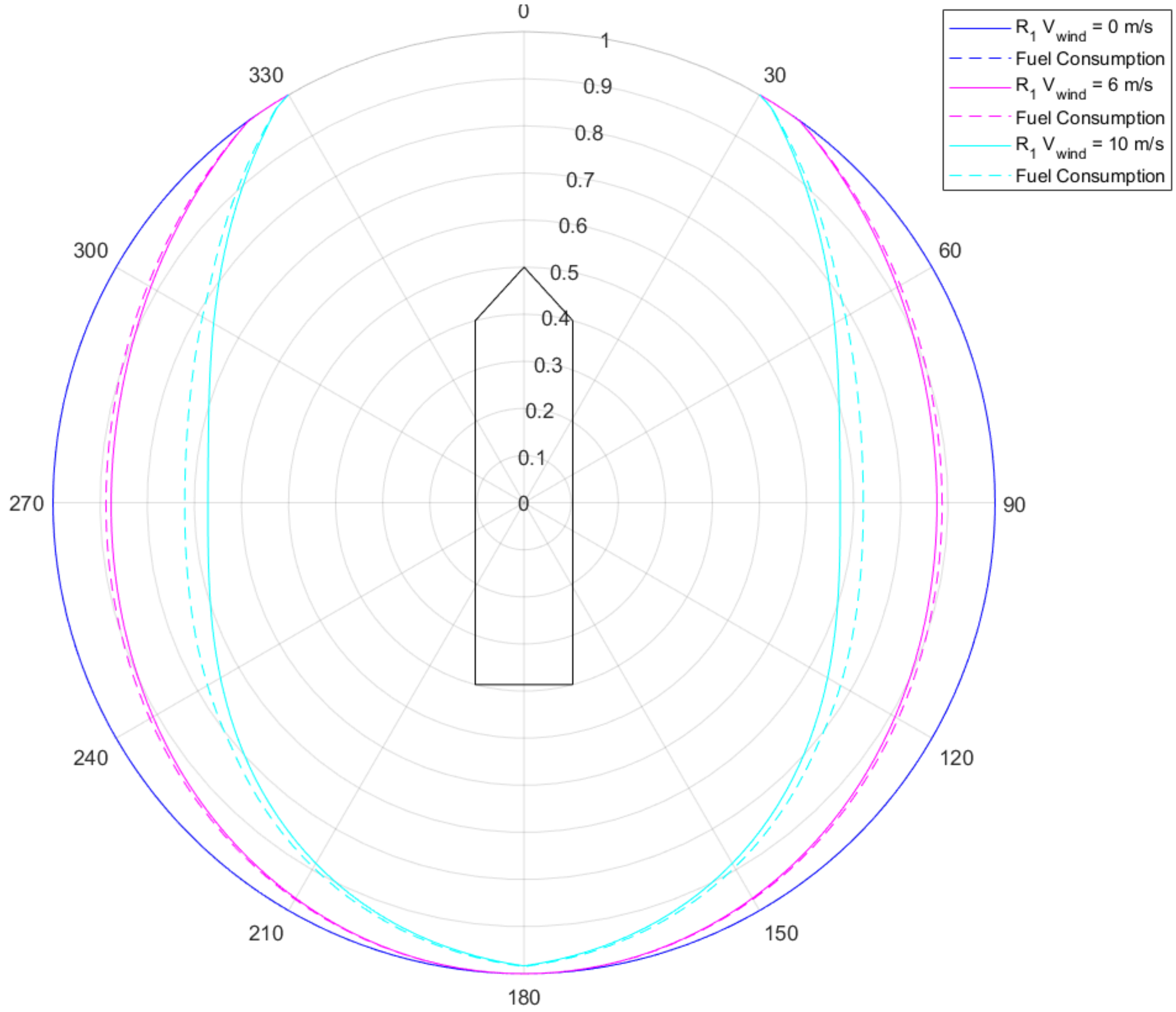

Figure B.2: FPP at a ship speed of $v_s = 11.5$ kts and engine speed of $n_e = 680$ RPM

Table B.2: $v_s = 11.5kts$, $n_e = 680$ RPM, TWA $= 90$ °, $R_0 = 109kN$

V_{wind}	R_1/R_0	η_D	SFOC [g/kWh]	FC_1/FC_0	FC[ton/h]
0	1	0.564	193.07	1	0.193
6	0.877	0.571	197.82	0.886	0.171
10	0.671	0.567	208.14	0.720	0.139

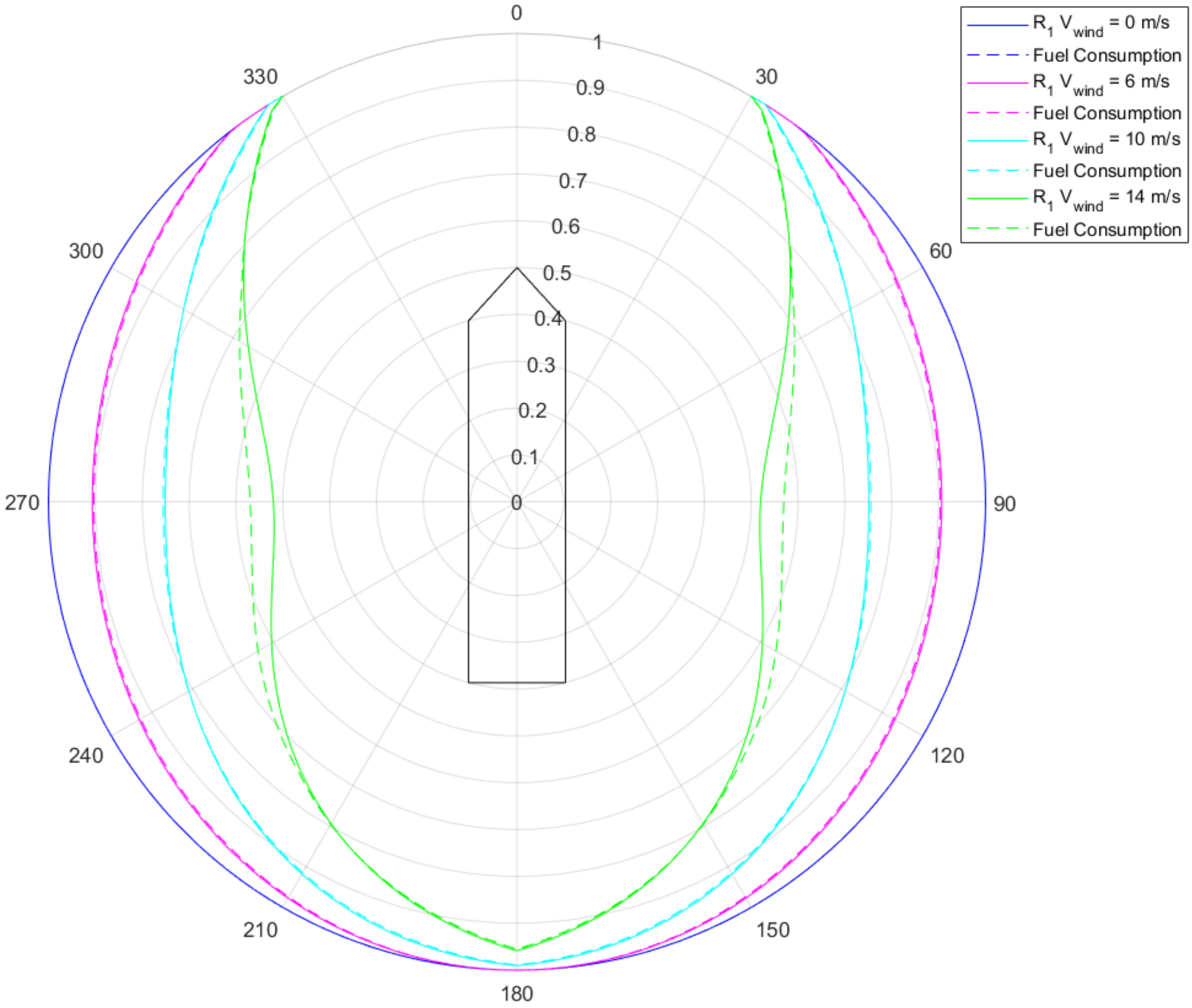

Figure B.3: FPP at a ship speed of $v_s = 12.5$ kts and engine speed of $n_e = 750$ RPM

Table B.3: $v_s = 12.5kts$, $n_e = 750$ RPM, TWA $= 90$ °, $R_0 = 144kN$

V_{wind}	R_1/R_0	η_D	SFOC [g/kWh]	$\dot{FC_1}/FC_0$	FC[ton/h]
0	1	0.5548	184.1	1	0.271
6	0.907	0.562	185.9	0.903	0.245
10	0.751	0.572	191.0	0.756	0.205
14	0.519	0.5573	202.7	0.569	0.154

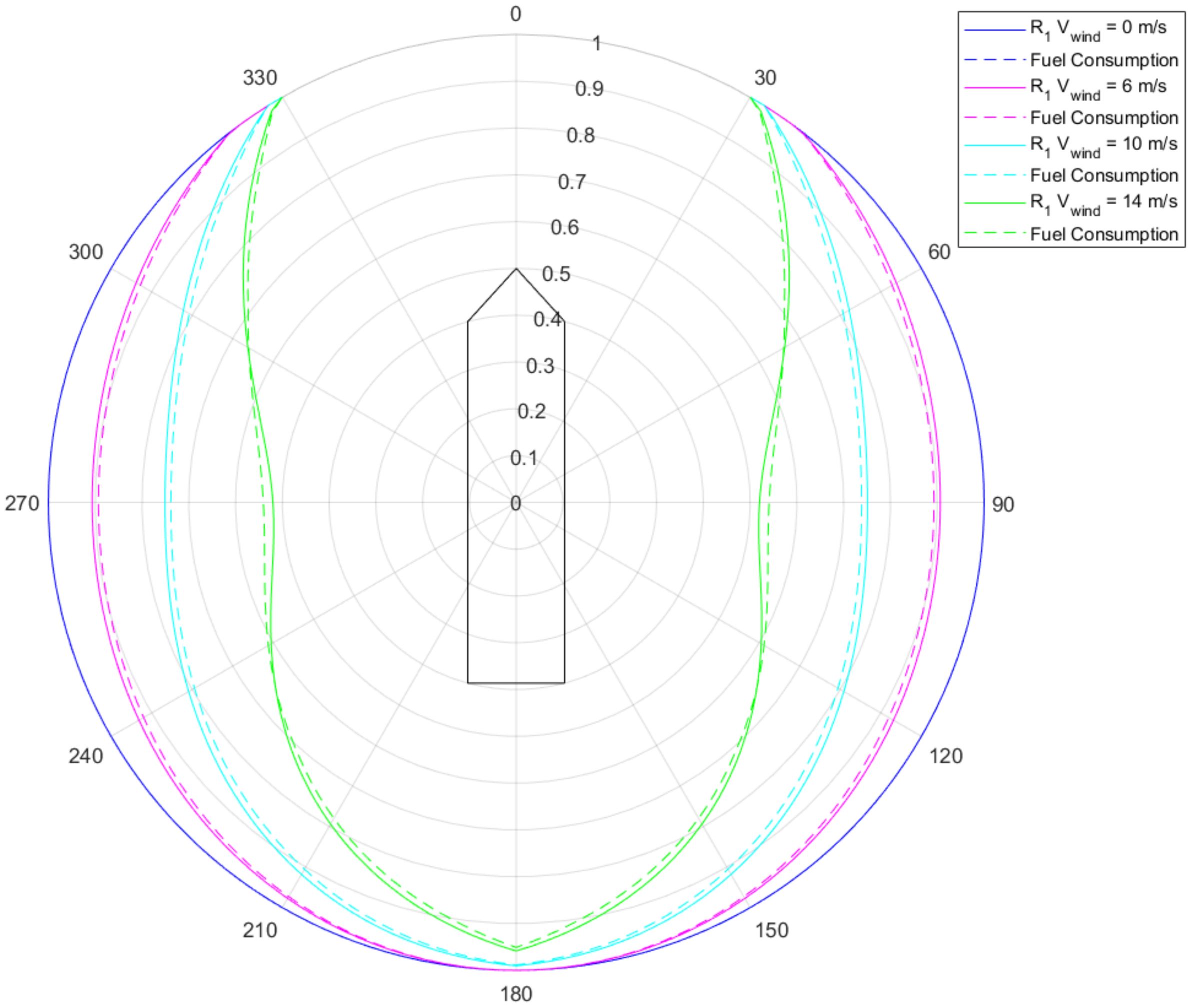

Figure B.4: FPP at a ship speed of $v_s = 12.5$ kts and engine speed of $n_e = 680$ RPM

Table B.4: $v_s = 12.5kts$, $n_e = 680$ RPM, TWA = 90 °, $R_0 = 144kN$

V_{wind}	R_1/R_0	η_D	SFOC [g/kWh]	FC_1/FC_0	FC [ton/h]
0	1	0.5554	184.2	1	0.271
6	0.907	0.5698	186.2	0.892	0.242
10	0.751	0.5883	191.8	0.738	0.200
14	0.519	0.5957	205.4	0.539	0.146

Appendix C

Testcases CFD Computations

Table C.1: C_L and C_D coefficients for different domain sizes with radii, R for an angle of attack $\alpha = 30$, with a suction speed of Cq = 0.047 .

Testcase ID	**Radius**	**xy plane cells**	C_L	C_D	C_{it}
1.1.1	20	764 x 628	7.756	0.4991	$5.2 \cdot 10^{-}8$
1.1.2	50	764 x 681	7.8937	0.3455	$5.6 \cdot 10^{-}8$
1.2.2	100	764 x 721	7.947	0.294	$1 \cdot 10^{-}8$
1.1.4	200	764 x 761	7.967	0.2671	$5.8 \cdot 10^{-}8$
1.1.5	500	764 x 814	7.9819	0.2508	$5.6 \cdot 10^{-}8$

Table C.2: C_L and C_D coefficients calculated with different grid size for estimating the discretization error and numerical uncertainty, for $\alpha = 30°$ and $C_q = 0.047$

Testcase ID	**Grid nr i**	h_i/h_1	C_L	C_D	C_{it}
1.2.1	1	1.00	7.963	0.288	$2.8 \cdot 10^{-}7$
1.2.2	2	1.41	7.947	0.294	$1 \cdot 10^{-}8$
1.2.3	3	2.00	7.951	0.293	$1 \cdot 10^{-}8$
1.2.4	4	2.83	7.971	0.289	$1 \cdot 10^{-}8$
1.2.5	5	4.00	7.963	0.297	$1 \cdot 10^{-}8$
1.2.6	6	5.66	7.785	0.363	$4 \cdot 10^{-}7$

Table C.3: Testcase 1.3: Calculated lift and drag coefficients with transition modeling, according to the RANS SST + LCTM turbulence model.

Testcase ID	**Grid nr i**	C_L	C_D	$C_{it,\gamma}$
1.3.1	4	7.958	0.290	$1.6 \cdot 10^{-}4$
1.3.2	3	7.938	0.295	$2.4 \cdot 10^{-}4$

Table C.4: Computed lift and drag coefficients for 2D steady RANS SST turbulence model for a range of angle of attack α at a suction rate of $C_q = 0.047$

Testcase ID	α	C_L	C_D	p_{suc} [Pa]	C_q [-]
1.4.1	0	4.04	0.146	-310	0.0469
1.4.2	5	4.79	0.175	-317	0.0473
1.4.3	10	5.52	0.203	-320	0.0476
1.4.4	15	6.22	0.227	-318	0.0472
1.4.5	20	6.88	0.246	-312	0.0461
1.4.6	25	7.49	0.270	-305	0.0475
1.4.7 =1.2.4	30	7.97	0.289	-287	0.0480

Table C.5: Computed lift and drag coefficients for 2D steady RANS SST turbulence model for a range of angle of attack α at a suction rate of $C_q = 0.032$

Testcase ID	α	C_L	C_D	p_{suc} [Pa]	C_q [-]
1.4.8	0	3.81	0.13	-275	0.0318
1.4.9	5	4.58	0.1436	-282	0.0312
1.4.10	10	5.32	0.1617	-285	0.0311
1.4.11	15	5.99	0.1795	-282	0.0313
1.4.12	20	6.53	0.2001	-270	0.0325
1.4.13	25	6.80	0.2207	-235	0.0326

Table C.6: Test case 1.5: time step variation study

Testcase ID	**Time step Δt in [s]**	**Average CFL number**	$C_{L,mean}$	$C_{D,mean}$
1.5.1	0.01s	40	X	X
1.5.2	0.005s	20	X	X
1.5.3	0.0025s	10	X	X
1.5.4	0.00125s	5	X	X

Table C.7: Computed lift and drag coefficients for 2D unsteady RANS SST turbulence model for a range of angle of attack α at a suction rate of $C_q = 0.047$

Testcase ID	α	C_L	C_D	p_{suc} [Pa]	$C_{q,min}$	$C_{q,mean}$	$C_{q,max}$
1.6.1	0	4.338	0.2263	-335	0.043	0.048	0.053
1.6.2	10	5.8576	0.2955	-350	0.043	0.048	0.053
1.6.3	25	7.6549	0.3543	-322	0.038	0.0479	0.058
1.6.4 = 1.5.3	30	7.9857	0.3854	-293	0.034	0.0472	0.06
1.6.5	32	8.0765	0.3854	-278	0.033	0.0463	0.059
1.6.6	35	8.2694	0.4142	-258	0.034	0.0486	0.06
1.6.7	40	8.1473	0.4686	-225	0.031	0.061	0.087

Table C.8: Computed lift and drag coefficients for 2D steady RANS SST turbulence model for a range of angle of attack α at a suction rate of $C_q = 0.032$

Testcase ID	α	C_L	C_D	p_{suc} [Pa]	$C_{q,min}$	$C_{q,mean}$	$C_{q,max}$
1.6.8	25	6.718	0.430	-238	0.014	0.0306	0.042
1.6.9	27	6.871	0.397	-232	0.014	0.033	0.046
1.6.10	30	6.125	0.718	-180	0	0.061	0.093

Table C.9: Computed lift and drag coefficients for 2D steady RANS SST turbulence model for a range of angle of attack α without suction so that $C_q = 0$

Testcase ID	α	C_L	C_D
1.6.11	0	1.1095	0.6727
1.6.12	5	1.5159	0.7503
1.6.13	10	2.2242	0.7116
1.6.14	15	2.5136	0.8352

Table C.10: Lift and drag coefficients for infinite span at $\alpha = 30°$ and $C_q = 0.047$, using a 3D grid examining the refinement in z-direction.

Testcase ID	**Nr of cells z- direction**	C_L	C_D	C_{it}
2.1.1	70	7.9661	0.2885	$1 \cdot 10^{-}8$
2.1.2	140	7.9663	0.2885	$1 \cdot 10^{-}8$
2.1.3	280	7.9661	0.2885	$1 \cdot 10^{-}8$

Table C.11: Computed lift and drag coefficients for 3D steady RANS SST turbulence model for a range of angle of attack α at a suction rate of $C_q = 0.047$

Testcase ID	α	C_L	C_D	p_{suc} [Pa]	$C_i t$	C_q
2.2.1	0	4.0328	0.1464	-310	$2.8 \cdot 10^{-7}$	0.0469
2.2.2	5	4.7925	0.1747	-317	$3 \cdot 10^{-7}$	0.0473
2.2.3	10	5.5197	0.2033	-320	$6.6 \cdot 10^{-7}$	0.0476
2.2.4	15	6.2119	0.2268	-318	$2.5 \cdot 10^{-8}$	0.0472
2.2.5	20	6.8715	0.2456	-312	$4 \cdot 10^{-7}$	0.0461
2.2.6	25	7.49	0.27	-305	$5.5 \cdot 10^{-8}$	0.0475
2.2.7	30	7.9662	0.2885	-287	$8.4 \cdot 10^{-8}$	0.048

Appendix D

Numerical Uncertainty Estimate

The method of Eça and Hoekstra, follows a procedure by finding the least square fit through the solution points of each calculation, using four different calculation methods, based on the quality of the least square fit.

The following conditions should be met, in order to do a qualitative error estimation,

1. The solution quantity ϕ_i, for a number of grids n_g should be in the 'asymptotic range', to estimate a the exact solution ϕ_{exact} and uncertainty estimate U_ϕ, with higher accuracy.

2. The grids must be geometrically similar, which means that the orthogonality, skewness, etc, is more or less preserved.

The following steps for calculating the numerical uncertainty U_ϕ is summarized in the following, and for the complete implementation of the numerical uncertainty analysis the publication of Eça and Hoekstra [23] may be reviewed. To determine the discretization error estimate ϵ, follow step 1.1-1.3

- Step 1.1. First solve the power series expansion function in equation D.1 in the least square sense with and without weight factor w_i, where p should be between $0.5 \leq p \leq 2$ to find an solution for the discretization error ϵ_ϕ. When both formula comply with this condition (with and without weight fucntion), the method giving the least variance should be adopted. When p is out of the suggested range, go to step 1.2.

  $$\epsilon_\phi \simeq \delta_{RE} = \phi_i - \phi_0 = \alpha h_i^p \tag{D.1}$$

  where ϕ_i represents a quantity of interest, such as the lift and drag coefficients, for a specific grid number i. ϕ_0 is an estimate of the exact solution, α a polynomial constant, h_i is a typical cell size, where grid 1, with h_1 is the finest available grid.

- Step 1.2. If the condition is for p is not satisfied and $p > 2$, equation D.2 and D.2 needs to be solved with and without weight factor. The equation with the smallest deviation σ should then be adopted for the uncertainty estimate. If $p < 0.5$, go to step 1.3.

  $$\epsilon_\phi \simeq \delta_1 = \phi_0 - \phi_i = \alpha h_i \tag{D.2}$$

  and

  $$\epsilon_\phi \simeq \delta_2 = \phi_0 - \phi_i = \alpha h_i^2 \tag{D.3}$$

- Step 1.3. If the order of p from equation D.1 is smaller than $p < 0.5$, equation D.4 should be solved with and without weight factors, solution with the smallest deviation should be adopted.

$$\epsilon_\phi = \delta_{12} = \phi_0 - \phi_i = \alpha h_i + \alpha h_i^2 \tag{D.4}$$

Finally, with the estimate of the exact solution ϕ_0, standard deviation σ and the order of convergence, p, to be known, the uncertainty estimate U_ϕ for the exact solution ϕ_{exact} with 95% confidence level can be made, with the expression given in equation D.5.

$$\phi_i - U_\phi \leq \phi_{exact} \leq \phi_i + U_\phi \tag{D.5}$$

The quality of the least square fit to the data points is expressed by a parameter $\Delta_p hi$, which divides the difference between the maximum and minimum value of quantity ϕ_i by the total number of grids n_g subtracted with 1, see equation D.6

$$\Delta_\phi = \frac{(\phi_i)_{max} - (\phi_i)_{min}}{n_g - 1} \tag{D.6}$$

Based on the order of convergence, expressed with p, a safety factor F_s, is defined. When p complies with $0.5 \leq p \leq 2$ using eq D.1, the safety factor becomes $F_s = 1.25$. For other p, the safety factor becomes $F_s = 3$.

The final expression for the uncertainty estimate is presented in equation .. and ... .

When $\sigma < \Delta_\sigma$, use:

$$U_\phi(\phi_i) = F_s \epsilon_\phi(\phi_i) + \sigma + |\phi_i - \phi_{fit}| \tag{D.7}$$

When $\sigma \geq \Delta_\phi$, the quality of the fit is worse and a safety factor of $F_s = 3$ must be applied:

$$U_\phi(\phi_i) = 3\frac{\sigma}{\Delta_\phi}(\epsilon_\phi(\phi_i) + \sigma + |\phi_i - \phi_{fit}|) \tag{D.8}$$

Equation D.1-D.8 give a complete overview of the solved equations to determine the uncertainty error estimate U_ϕ and the exact solution ϕ_{exact} within confidence bounds of 95%.

Appendix E

Axial Fan Specifications

Link to website: https://www.systemair.com/nl/Rucon-Systemair/VentilatieProducten/ventilatoren–toebehoren/axiaal-ventilatoren/middendruk-axiaal-ventilatoren/axc/AXC-1000/

AXC 1000

Artikel nr: C1000AXC

Axiaal ventilator serie AXC, geschikt voor werktemperatuur tot 55°C

- Luchtrichting over de motor naar schoepenwiel, direct gedreven
- Schoepenwiel is verstelbaar om optimale werkpunt te verkrijgen
- Aluminium huis en bladen. Schoepenwiel is statisch en dynamisch gebalanceerd volgens DIN/ISO1940-1 6.3
- Lange behuizing, gegalvaniseerd staal volgens DIN/ISO1461
- Flenzen volgens Eurovent 1/2
- VDE gecertificeerde aanluitbox IP65 die is gemonteerd aan de buitenzijde om eenvoudig aan te sluiten
- 3-phase motoren IE2 of IE3 / IP55 / ISO F volgens EN60034-5 / IEC85

Figure E.1: Technical specifications of the axial fan AXC-1000.

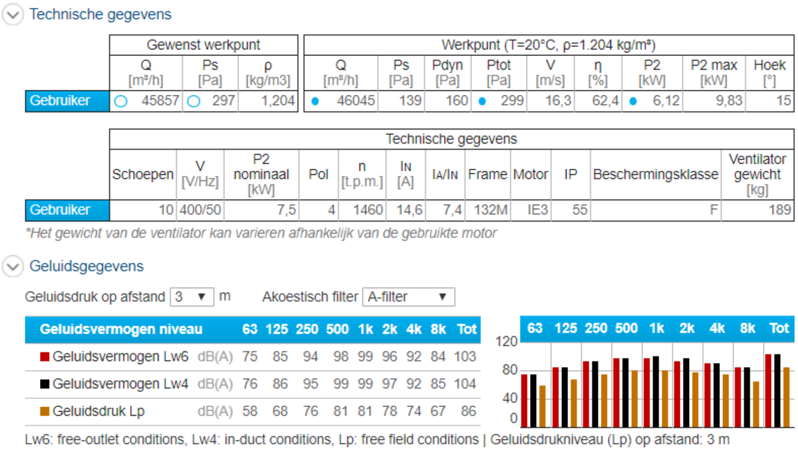

Technische gegevens

	Gewenst werkpunt			Werkpunt (T=20°C, ρ=1.204 kg/m^3)								
	Q [m^3/h]	Ps [Pa]	ρ [kg/m3]	Q [m^3/h]	Ps [Pa]	Pdyn [Pa]	Ptot [Pa]	V [m/s]	η [%]	P2 [kW]	P2 max [kW]	Hoek [°]
Gebruiker	○ 45857	○ 297	1,204	● 46045	139	160	● 299	16,3	62,4	● 6,12	9,83	15

	Technische gegevens											
	Schoepen	V [V/Hz]	P2 nominaal [kW]	Pol	n [t.p.m.]	IN [A]	IA/IN	Frame	Motor	IP	Beschermingsklasse	Ventilator gewicht [kg]
Gebruiker	10	400/50	7,5	4	1460	14,6	7,4	132M	IE3	55	F	189

*Het gewicht van de ventilator kan varieren afhankelijk van de gebruikte motor

Geluidsgegevens

Geluidsdruk op afstand 3 ▼ m   Akoestisch filter A-filter ▼

Geluidsvermogen niveau		63	125	250	500	1k	2k	4k	8k	Tot
🟥 Geluidsvermogen Lw6	dB(A)	75	85	94	98	99	96	92	84	103
■ Geluidsvermogen Lw4	dB(A)	76	86	95	99	99	97	92	85	104
🟧 Geluidsdruk Lp	dB(A)	58	68	76	81	81	78	74	67	86

Lw6: free-outlet conditions, Lw4: in-duct conditions, Lp: free field conditions | Geluidsdrukniveau (Lp) op afstand: 3 m

Figure E.2: Technical specifications of the axial fan AXC-1000.

Air direction: SO/SU (vertical). (SO = air direction upwards; SU = air direction downwards)

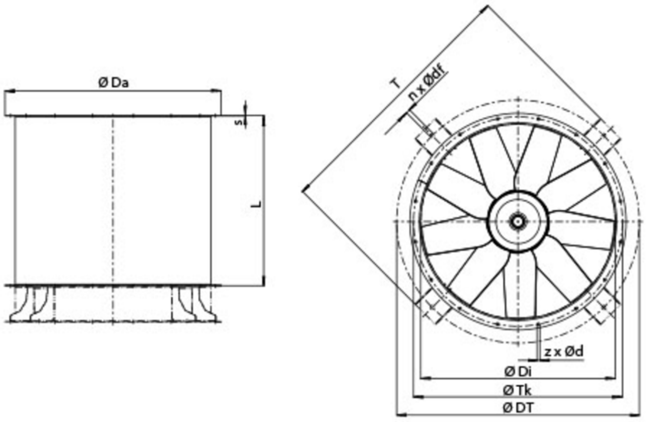

ØDa	ØDi	ØTk	zxØd	ØDT	T	nxØdF	s	Motor	L
1105	1000	1070	16x 15	1208	1288	4x 11	4,0	100-132	640
								160-200	850

Figure E.3: Dimensions of axial fan AXC-1000.